

Group IV (Si)GeSn Light Emission and Lasing Studies

Daniela Stange

Schlüsseltechnologien / Key Technologies Band / Volume 193 ISBN 978-3-95806-389-1



Schriften des Forschungszentrums Jülich Reihe Schlüsseltechnologien / Key Technologies

Band / Volume 193

Forschungszentrum Jülich GmbH Peter Grünberg Institut Halbleiter-Nanoelektronik (PGI-9)

Group IV (Si)GeSn Light Emission and Lasing Studies

Daniela Stange

Bibliografische Information der Deutschen Nationalbibliothek. Die Deutsche Nationalbibliothek verzeichnet diese Publikation in der Deutschen Nationalbibliografie; detaillierte Bibliografische Daten sind im Internet über http://dnb.d-nb.de abrufbar.

Herausgeber Forschungszentrum Jülich GmbH

und Vertrieb: Zentralbibliothek, Verlag

52425 Jülich

Tel.: +49 2461 61-5368 Fax: +49 2461 61-6103 zb-publikation@fz-juelich.de www.fz-juelich.de/zb

Umschlaggestaltung: Grafische Medien, Forschungszentrum Jülich GmbH

Druck: Grafische Medien, Forschungszentrum Jülich GmbH

Copyright: Forschungszentrum Jülich 2019

Schriften des Forschungszentrums Jülich Reihe Schlüsseltechnologien / Key Technologies, Band / Volume 193

D 82 (Diss., RWTH Aachen University, 2019)

ISSN 1866-1807 ISBN 978-3-95806-389-1

Vollständig frei verfügbar über das Publikationsportal des Forschungszentrums Jülich (JuSER) unter www.fz-juelich.de/zb/openaccess.



This is an Open Access publication distributed under the terms of the Creative Commons Attribution License 4.0, which permits unrestricted use, distribution, and reproduction in any medium, provided the original work is properly cited.

"When God said 'Let there be light' he surely must have meant perfectly coherent light."

- Charles Townes

Abstract

To enable the continuous evolution of information technology, increasing data transfer rates are demanded. This is accompanied by rising power consumption and requisition of larger bandwidths. The integration of photonics with electronic circuits provides a solution, which facilitates the decrease of heat dissipation and allows transmitting data in parallel with the speed of light, boosting the performance of integrated circuits. Such a concept is preferably realized within the highly elaborated silicon processing technology, on which the whole information technology is based on. The most pressing issue, missing for the fully integration of photonics to electronics, is an integrated light source. Silicon-germanium-tin (SiGeSn) alloys offer a promising extension of this platform, since they can be monolithically grown on Si and their direct bandgap in specific configurations was proven in 2015.

This thesis summarizes studies on spontaneous and stimulated emission of GeSn alloys mainly based on photoluminescence (PL) and electroluminescence (EL) spectroscopy. The effect of strain relaxation in GeSn alloys, grown on top of Ge virtual substrates, on optical properties is investigated. The temperature trend of spontaneous emission provides insight on the contribution of non-radiative defect recombination. It also illustrates the indirect-to-direct bandgap transition in $Ge_{0.875}Sn_{0.125}$ alloys under strain relaxation. Heterostructure PL analysis emphasizes the importance of defect engineering, since presence of defects close to the active layer heavily deteriorates light emission.

To prove the concept of electrical carrier injection, GeSn-based LEDs are fabricated. Electroluminescence spectra unveil similar temperature dependent behavior as PL from unprocessed layers, with comparable defect-induced limitations. The examination of Ge and SiGeSn as barrier materials in multi-quantum-wells (MQWs) proves

SiGeSn as the material of choice due to a better carrier confinement.

Subsequently, stimulated emission from undercut microdisk cavities is investigated. For the first time, single layer GeSn microdisk lasers are presented, offering increased mode confinement due to high refractive index contrasts compared to common Fabry-Pérot lasers. The undercut leads to an almost complete strain relaxation modifying the band structure of the gain material. Even "just direct" GeSn alloys are proven to be suitable as gain material.

To further enhance the electron population at the direct Γ -valley, which is still limited by the moderate difference between L- and Γ -valley, in-situ n-doping of direct bandgap GeSn is studied. Lasing is detected in these materials, however, showing no advantage compared to the undoped lasers. This is attributed to simultaneously increased defect recombination.

The first GeSn/SiGeSn heterostructure lasers yield record low thresholds in an MQW design, enabled by carrier confinement, screening from misfit dislocations and a 2D density of states. Limitations were found, on one hand, in layer stacks with large volume-strain, hindering efficient barriers from shielding defective regions. On the other hand, directness and barrier offsets are reduced by strong quantization effects.

Finally, a process flow for electrically-driven laser designs with micro ring and waveguide geometry is introduced, underlining the applicability of group IV photonics integration into Si technology.

Zusammenfassung

Die kontinuierliche Entwicklung der Informationstechnologie erfordert immer höhere Datenübertragungsraten. Das geht sowohl mit wachsendem Energieverbrauch, als auch der Forderung nach größeren Bandbreiten einher. Eine Lösung bietet die Integration von photonischen Bauelementen in elektronische Schaltkreise. Diese ermöglicht Wärmeverluste zu senken und Daten parallel mit Lichtgeschwindigkeit zu übermitteln, was insgesamt zu einem Anstieg der Leistungsfähigkeit in solchen integrierten Schaltkreisen führt. Da die gesamte Informationstechnologie auf der bereits hoch entwickelten Silizium (Si) Technologie basiert, ist es vorteilhaft die Realisierung solcher Konzepte innerhalb dieser Technologie umzusetzen. Zur vollständigen Integration photonischer in elektronische Schaltkreise, ist die Herstellung einer kompatiblen Lichtquelle am dringlichsten. Legierungen aus Si, Germanium (Ge) und Zinn (Sn) stellen eine vielversprechende Erweiterung dieser Plattform dar, da sie monolithisch auf Si-Wafer gewachsen werden können. Außerdem wurde 2015 gezeigt, dass bei bestimmten Zusammensetzungen ein direkter Halbleiter entsteht.

In dieser Arbeit werden Studien zur spontanen und stimulierten Emission von GeSn-Legierungen, basierend auf Photolumineszenz (PL) und Elektrolumineszenz (EL) Spektroskopie, zusammengefasst. Dabei wird der Effekt der plastischen Spannungsrelaxation auf die optischen Eigenschaften der GeSn Schichten – gewachsen auf Ge Pufferschichten – untersucht. Der temperaturabhängige Verlauf der spontanen Emission liefert Einblicke in die nicht-radiative Defektrekombination. Zusätzlich kann dadurch in Ge_{0.875}Sn_{0.125} der Übergang von einem indirekten zu einem direkten Halbleiter ausschließlich durch Spannungsrelaxation aufgezeigt werden. PL Analysen an Heterostrukturen stellen die Relevanz des Defekt-Engineerings heraus, da durch die Anwesenheit von Defekten nahe des aktiven Materials die Lichtemission

stark vermindert wird.

Durch die Fabrikation von GeSn-basierten Leuchtdioden (LEDs), wird das Konzept der elektrischen Ladungsträgerinjektion überprüft. Elektrolumineszenzspektren zeigen die gleichen Defekt-induzierten Limitierungen, die auch in PL Messungen an unprozessiertem GeSn gefunden wurden. Die Auswertung unterschiedlicher Materialien für Potentialbarrieren in Mehrfach-Quantentopf-Heterostrukturen (MQW) lässt erkennen, dass SiGeSn hierfür auf Grund einer besseren Ladungsträgerbeschränkung das Material der Wahl ist.

Des Weiteren wird stimulierte Emission an Kavitäten aus unterätzten Mikroscheiben untersucht. Zum ersten Mal wurden Mikroscheiben-Laser aus einfachen GeSn Schichten gezeigt. Im Vergleich zu nicht unterätzten Fabry-Pérot Lasern verfügen sie über eine bessere lokale Beschränkung der Mode, die durch den guten Kontrast der Brechungsindizes begünstigt wird. Darüber hinaus erlaubt die Unterätzung eine fast vollständige Spannungsrelaxation der GeSn Schicht. Dadurch wird ihre Bandstruktur modifiziert, sodass auch für einen gerade direkten Halbleiter die Tauglichkeit als Lasermaterial nachgewiesen werden konnte. Die Elektronenpopulation am Γ -Punkt, die trotz direktem Halbleiter durch den moderaten Energieunterschied zwischen den Bandkanten an L und Γ (auch Direktheit genannt) begrenzt ist, kann durch n-Dotierung erhöht werden. Solches Material zeigt zwar Laserverhalten, jedoch kann kein Vorteil gegenüber undotierten Schichten festgestellt werden. Das ist zurückzuführen auf die damit einhergehende erhöhte Defektrekombination.

Erste GeSn/SiGeSn MQWs weisen sehr niedrige Laserschwellen auf. Dies wird durch die Beschränkung der Ladungsträger in der aktiven Schicht, deren Abschirmen von Versetzungsfehlern, wie auch durch die 2 dimensionale Zustandsdichte in diesem Schichtsystem ermöglicht. Allerdings wurden Verschiedene Limitierungen für Heterostruktur Laser gefunden. Einerseits führt eine große Volumenspannung durch zu dicke Schichten zur weiteren Relaxation des Schichtsystems, was die Abschirmung von Ladungsträgern zu defekten Regionen verhindert. Andererseits werden sowohl die Direktheit, als auch die Potentialdifferenz von Barriere und Quantentopf durch zu starke Quantisierungseffekte reduziert.

Zuletzt wird ein Prozess für elektrisch gepumpte Laser mit Mikroring und Fabry- $P\'{e}rot$ Kavitäten vorgestellt, was eine Integration von Gruppe IV-basierter Photonik in die Si-Technologie ermöglichen kann.

Contents

1.	Intro	oduction	1
2.	(Si)	GeSn Material Properties	5
	2.1.	From Indirect to Direct Bandgap GeSn	6
		2.1.1. Sn Incorporation	6
		2.1.2. Strain Dependence	8
		2.1.3. Si Incorporation	Ĝ
	2.2.	From Homojunction to Heterostructures	11
	2.3.	Radiative and Non-Radiative Recombination	13
3.	Pho	toluminescence of GeSn Alloys	19
	3.1.	GeSn Single Layer	20
	3.2.	GeSn/SiGeSn Heterostructures	27
		3.2.1. Material Overview	28
		3.2.2. Light Emission	30
	3.3.	Summary	35
4.	Ligh	t Emitting Diodes	37
	4.1.	Fabrication and Electrical Characterization	38
	4.2.	Homojunction LEDs	42
	4.3.	-	
		4.3.1. Ge Barriers	48
		4.3.2. SiGeSn Barriers	
	4.4.	Summary	

Contents

5.	Opt	ically Pumped Lasers	61
	5.1.	Laser Theory	63
	5.2.	Fabrication and Measurement Routine	68
	5.3.	GeSn Single Layer Lasers	69
		5.3.1. Strain Distribution in Suspended Disk Structures	
		5.3.2. Lasing Characteristics	73
	5.4.	GeSn:P for Lasers	79
		5.4.1. Material Overview	80
		5.4.2. Lasing Characteristics	83
	5.5.	GeSn/SiGeSn Heterostructure Lasers	85
		5.5.1. Strain and Band Structure in Undercut MQW Microdisks $$	86
		5.5.2. Lasing Characteristics	89
	5.6.	Summary	96
6.	Tow	ards Electrically Pumped Lasing	99
7.	Con	clusion and Outlook	105
Α.	Арр	endix	111
Bi	bliog	raphy	113
Ac	know	vledgments	143
Lis	st of	Publications	147
Cι	ırricu	lum Vitae	153

1. Introduction

The first laser was discovered in 1960 by optical excitation of a 1 cm long ruby crystal. 12-14 Laser technology developed fast, comprising a broad energy range and to date, after 55 years, reaches device dimensions of nanometer scale. 15,16 Shortly after demonstration of the ruby laser, experimental work on semiconductor lasers started on III-V materials. 17,18 In 1962, first GaAs lasers with relatively high thresholds between 8 kA cm⁻² to 100 kA cm⁻² were presented at 77 K.¹⁹⁻²¹ The continuous threshold decrease was achieved by application of heterostructures, quantum wells and quantum dots, ²² as well as advanced designs for current and mode confinement. Today, semiconductor lasers and diodes cover a wide field of applications from spectroscopy for e.g. medical diagnostics, laser beam machining to telecommunication. But the rapidly developing technological world poses new challenges. Novel application opportunities like the internet of things (IoT), or training of neural networks will dramatically rise the amount of processed and transferred data.^{23,24} Forecasts referring only to internet traffic, predict a three-fold increase from 2016 to 2021.²⁵ Hence, research in different areas is concerned with solving problems of increasing power consumptions and the demand of larger bandwidths. A part of scientists focused on new concepts like opto-electronic integrated circuits (OEICs), deeming the integration of optical components into electronic circuits. By using optical instead of copper interconnects, the heat dissipation and therefore the energy consumption of inter- and intra-chip communication is reduced. ^{26–28} Furthermore, they increase bandwidth compared to copper interconnects by allowing parallel data transfer, e.g. using wavelength multiplexing.^{29,30}

nents is preferred to match this technology, establishing the field of Si photonics. 31,32 The simplest option of materials from the growth and processing point of view are configurations of group IV elements. Their main drawback is the unsuitability to efficiently emit light due to their indirect bandgap character, for example in silicon and germanium (Ge). In contrast, III-V compound semiconductor lasers were already in a highly developed status and have therefore been the first choice for photonic circuits. Different procedures were developed like bonding III-V lasers on Si or Si on insulator (SOI) wafers, 33–36 as well as the direct growth of III-V layer stacks on Si. 37,38 Both are complex methods and not used in large scale integration yet. For this reason, optical interconnect designs based on Si often use external laser sources. 39,40

A light source consisting of group IV materials would facilitate monolithic integration into the chip technology. Therefore, different approaches, how to turn a group IV material into a direct bandgap semiconductor, were fathomed.⁴¹ In addition to the application of tensile strain to Ge,^{42–44} the alloying of Ge with tin (Sn) turned out to be a possible solution.⁴⁵ The demonstration of a direct bandgap and optically pumped lasing in GeSn⁴⁶ depicted the start for raising research activities in this field.

Apart from photonic applications the material offers promising prerequisites for electronic devices like metal-oxide-semiconductor field effect transistors (MOSFETs), 47 due to its small electron effective mass at Γ and the resulting increased mobility. The direct bandgap nature also leads to an enhanced band-to-band tunneling rate, which is why GeSn might be also suitable for group IV tunnel FETs. 48

GeSn lasers in a wavelength range from $2.0\,\mu\mathrm{m}$ to $3.1\,\mu\mathrm{m}$ have been presented up to now offering not only a new wavelength band for optical communication, but also the potential for sensing in the mid-IR range.^{3,49,50} Beside spectroscopy on a chip for medical diagnostics,⁵¹ absorption lines of carbon monoxide (CO) or greenhouse gases like water vapor (H₂O), carbon dioxide (CO₂) and methane (CH₄) are in this wavelength regime.^{52,53}

Since a large number of possible application areas of GeSn lasers exists, the further investigation of those group IV alloys is significant. To date these light sources are in a premature state and many mechanisms are not fully understood yet. Quite comparable to III-V history, the first lasing was reached with a pumping carrier density of

approximately 2×10^{18} cm⁻³ in GeSn waveguides,⁵⁴ which was the same calculated carrier density, required to obtain lasing in the GaAs system.⁵⁵ Since then, years of studies and deepening the physical understanding followed. This thesis contributes a part of the investigation and evolution of GeSn-based light emitters and lasers. The aim is to analyze spontaneous, as well as stimulated emission characteristics in the (Si)GeSn material system.

The thesis contains seven chapters. After this introduction, the basics of Si-Ge-Sn band structure properties are described in **chapter 2** to provide a physical introduction into the topic. **Chapter 3** deals with photoluminescence studies of various GeSn alloys, comprising the strain induced indirect-to-direct bandgap transition and temperature dependent effects in homo- and heterostructures. Founding on previous results, in **chapter 4** LEDs are fabricated and analyzed. Different barrier materials in GeSn MQW light emitters are examined. Lasing from GeSn microdisk (MD) cavities is presented in **chapter 5**. Strain distribution in undercut MD geometries and the resulting band structures are discussed. Heterostructure designs in MDs are analyzed and compared to single layer GeSn lasers with regard to maximum lasing temperature and threshold. Finally, a fabrication process for electrically pumped lasers is developed in **chapter 6**, demonstrating their compatibility with Si CMOS processing technology. A brief summary and future outlook can be found in **chapter 7**.

2. (Si)GeSn Material Properties

Contents

2.1. From Indirect to Direct Bandgap GeSn	6
2.1.1. Sn Incorporation	6
2.1.2. Strain Dependence	8
2.1.3. Si Incorporation	9
2.2. From Homojunction to Heterostructures	11
2.3. Radiative and Non-Radiative Recombination	13

As early as 1982 Germanium-Tin (GeSn) has been theoretically proposed as a possible direct bandgap group IV material.⁵⁶ From that point onwards, it took over thirty years to overcome the challenges of crystal growth and to form a metastable direct bandgap GeSn alloy.

Simultaneously to the proof of direct bandgap formation in GeSn, the first optically pumped lasing was demonstrated.⁴⁶ This opened up a large research field for GeSn in optical devices, like light emitter, detector and modulator in group IV photonics.^{27,57,58}

Before presenting the results on development of layer stacks, diodes and lasers, this chapter gives a general overview about the Si-Ge-Sn material system. Electronic and optical material properties and characteristics are considered in respect to light emitter applications on the group IV platform. In the first section, band structure of different Si-Ge-Sn alloy configurations is discussed with the main focus on the transition from indirect to direct bandgap semiconductors. The second section deals

with the advantages and applications of heterostructures, followed up by the third section, which discusses the basics of radiative and non-radiative recombination of charge carriers in semiconductors.

2.1. From Indirect to Direct Bandgap GeSn

In this section, different ways to achieve a direct bandgap semiconductor in the Ge-Sn system are introduced. On one hand, the incorporation of a sufficient amount of Sn is mandatory to induce the transition from indirect bandgap Ge to a direct bandgap GeSn. On the other hand, strain also plays an essential role in modifying the band structure.

2.1.1. Sn Incorporation

The direction towards creating a direct bandgap semiconductor can be deduced from the electronic band structure of the particular elements. Ge is a semiconductor with an indirect bandgap at the L-valley of $0.76\,\mathrm{eV}$ and a direct bandgap at Γ of $0.90\,\mathrm{eV}$ at $0\,\mathrm{K}$. That makes it an indirect bandgap semiconductor with a rather small energy difference between Γ and L of $140\,\mathrm{meV}$. ⁵⁹

In contrast, α -Sn is a semi-metal, which is stable at temperatures below 13 °C, having an inverted band structure at Γ and therefore a negative bandgap of $-0.41\,\mathrm{eV}$. Electronic band structure diagrams in the first Brillouin zone of Ge and Sn are presented in figures 2.1a and b. Alloying Ge with Sn changes the band structure so that the conduction band of Ge is shifted downwards in energy towards the valence bands. Bandgaps at critical points of the Brillouin zone can be calculated using an interpolation between both materials, 62 including the respective bowing parameter b_i , which describes the deviation from the linear interpolation:

$$E_i(x) = E_i^{\text{Ge}}(1-x) + E_i^{\text{Sn}}x + b_i^{\text{GeSn}}x(1-x), \tag{2.1}$$

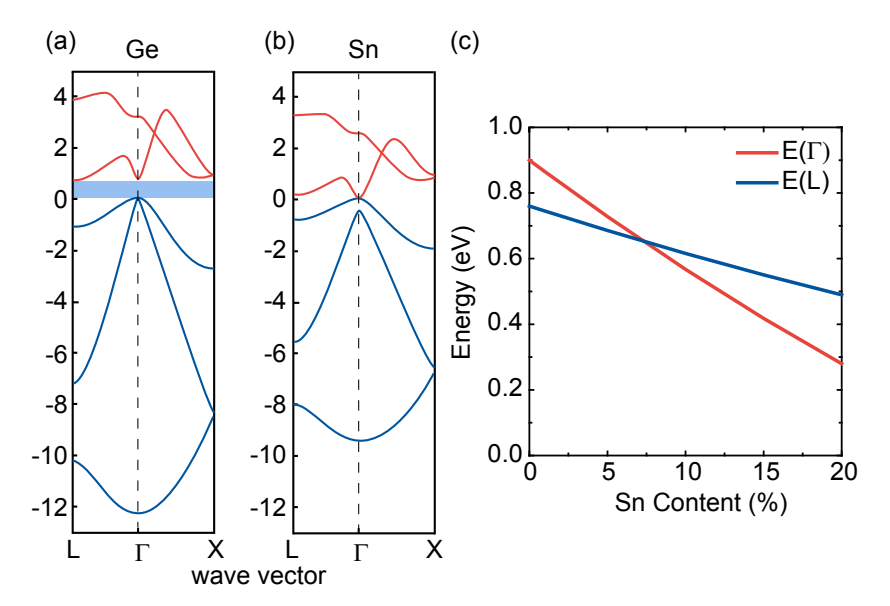


Figure 2.1. Electronic band structure of semiconductor Ge (a) and semi metal Sn (b), adapted from reference [61]. ©IOP Publishing. Reproduced with permission. All rights reserved. In (c) transition from indirect to fundamental direct bandgap GeSn is shown dependent on Sn concentration.

where x is the Sn concentration in the alloy and i denotes the particular point in the Brillouin zone, i.e. Γ , L or X, for which the energy is calculated. All important band energies are summarized in table 2.1 on page 11.

Since the band energy difference between Ge and α -Sn at Γ is larger compared to L $(E_{\Gamma,\text{Ge}}-E_{\Gamma,\text{Sn}}) > E_{L,\text{Ge}}-E_{L,\text{Sn}})$, the bands decrease faster at the Γ -point and, together with the fact that $E_{\Gamma,Sn} < 0$, this leads to a transition from indirect to direct bandgap GeSn alloy at some concentration of Sn. The transition point is calculated to occur above 7 at.% Sn for a cubic lattice at 0 K using $b_{\Gamma,\text{GeSn}} = 2.24\,\text{eV} - 4 \times 10^{-4}\,T$ and $b_{L,\text{GeSn}} = 0.89\,\text{eV} + 7 \times 10^{-4}\,T$. ^{63,64} The dependence of the conduction band energies at L and Γ on the Sn content x is plotted in figure 2.1c. All band structure calculations, shown in this thesis, are performed in cooperation with Dr. Zoran Ikonić from the UNIVERSITY OF LEEDS and my colleague Denis Rainko. Experimentally, the transition between indirect and direct GeSn was shown in 2015 to take place at

 ~ 9 at.% for a cubic lattice.⁴⁶

2.1.2. Strain Dependence

A critical parameter influencing the band structure of GeSn alloys is strain. All GeSn alloys, investigated in this thesis, are grown by reduced-pressure chemical vapor deposition (RP-CVD) in an industry-compatible Aixtron reactor^a. Silicon (Si) (001) wafers (200 mm) with a $\sim 2.5 \, \mu m$ thick Germanium virtual substrate (Ge-VS)^b on top are used as substrates.^{8,65} Pseudomorphic growth of GeSn layers on top of the Ge-VS imposes biaxial compressive strain in the GeSn lattice. When exceeding a specific volume strain, the GeSn layer starts to relax. With rising Sn concentration, the lattice mismatch between GeSn and Ge becomes larger. After passing the thickness when strain relaxation started, the increase of the layer thickness leads to a higher degree of relaxation. Thus, depending on Sn concentration and layer thickness, the strain in the particular layers varies.

Compressive biaxial strain influences the band structure of GeSn alloys in the opposite way compared to incorporation of Sn. Band energies are shifted up with increasing compressive strain, moving the indirect-to-direct bandgap transition to larger Sn concentrations. Therefore, it is possible to grow multiple GeSn alloys with a constant Sn concentration but different bandgaps, indirect as well as direct. The lattice constant for cubic, and thus relaxed, GeSn alloy a_0 , can be related to experimentally determined in- and out-of plane lattice constants $(a_{\parallel}^{\text{GeSn}}$ and a_{\perp}^{GeSn} , respectively), as well as the interpolated elastic constants C_{11} and C_{12} :⁶⁶

$$a_0^{\text{GeSn}} = \frac{a_{\perp}^{\text{GeSn}} + 2a_{\parallel}^{\text{GeSn}} C_{12}/C_{11}}{1 + 2C_{12}/C_{11}}.$$
 (2.2)

^aMany thanks to my colleagues *Dr. Nils von den Driesch* and *Denis Rainko*, who grew all layers I worked with

^bGe-VS was provided by Dr. Jean-Michel Hartmann from CEA/LETI, Grenoble.

These lattice constants can be subsequently used to determine the biaxial strain ϵ_{\parallel} of the layer:

 $\epsilon_{\parallel} = \frac{a_{\parallel}^{\text{GeSn}} - a_0^{\text{GeSn}}}{a_0^{\text{GeSn}}}.$ (2.3)

Strain has then to be considered in band structure calculations as a correction term to the calculated bulk energy values. These corrections come from deformation potentials corresponding to hydrostatic and biaxial strain, which need to be included for each symmetry point of the Brillouin zone.^{67,68} The most important band energies, lattice and elastic constants of Si, Ge and Sn used for all band structure calculations in this thesis are summarized in table 2.1.

Besides the bandgap, the difference of conduction band energy between L and Γ , $\Delta E_{L\Gamma} = E_L - E_{\Gamma}$, is an essential parameter and will be referred to as directness in the remainder of the thesis. If $\Delta E_{L\Gamma} < 0$, the semiconductor is an indirect bandgap semiconductor, if $\Delta E_{L\Gamma} > 0$ the semiconductor is defined as direct. The directness strongly influences the properties of light emission, since the electron occupation of the Γ -valley increases for a higher directness, rising the probability of radiative recombination of carriers. However, even for the direct bandgap GeSn alloys used in this work (Sn < 14 at.%), at room temperature the largest fraction of electrons will reside in the L-valley because of a large DOS, while at 4 K the majority will be condensed in Γ .

An overview of the directness for alloys with different Sn content and variable strain is shown in figure 2.2. The directness, which can be kept constant for alloys with variable Sn concentration and strain, is indicated by solid black lines and its values are written in white font. The transition from indirect to direct bandgap semiconductor occurs at the line with $\Delta E_{L\Gamma} = 0$.

2.1.3. Si Incorporation

Incorporating a third group IV element, Silicon (Si), into GeSn allows strain independent bandgap tuning. Si has a lattice constant smaller than Ge and Sn and therefore reduces the compressive strain which is built up in an alloy by the Sn concentration. Secondly, Si shifts the bandgap energies to larger values. With these

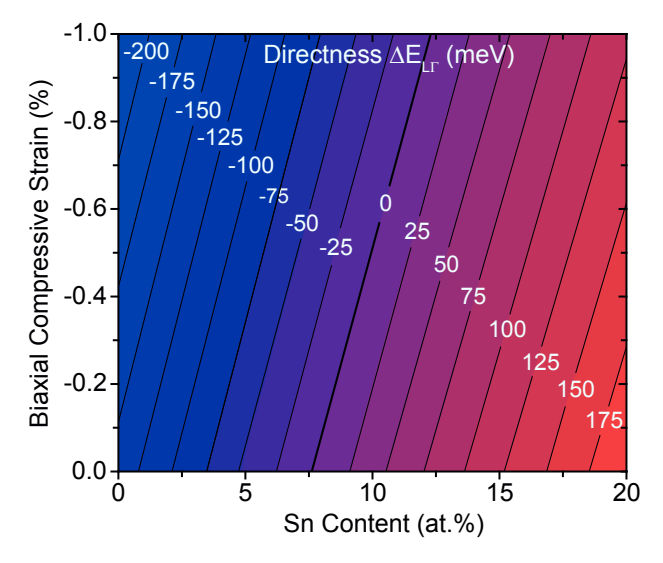


Figure 2.2. Alloy directness as it depends on Sn concentration and biaxial strain. The Sn concentration, required to reach the transition from an indirect to a direct bandgap semiconductor, is shifted to larger values for higher compressive strain.

characteristics, if SiGeSn ternaries are direct, they can be used as shorter wavelength emitters and detectors compared to GeSn and serve as appropriate material for cladding and barriers in heterostructure designs, if they are indirect.⁶⁸ To calculate the band energies, the same interpolation as for GeSn can be used by adding the terms for Si content y in $Si_yGe_{1-x-y}Sn_x$:⁶²

$$E_i(x) = E_i^{\text{Ge}}(1 - x - y) + E_i^{\text{Si}}y + E_i^{\text{Sn}}x + b_i^{\text{SiGe}}(1 - x - y)y + b_i^{\text{SnGe}}(1 - x - y)x + b_i^{\text{SiSn}}xy.$$
(2.4)

At L, a theoretically extrapolated bowing parameter of $b_{\rm L}^{\rm SiSn}=2.124\,{\rm eV^{62}}$ is used in our calculations. The attempt to verify the calculated $b_{\rm T}^{\rm SiSn}=3.915\,{\rm eV^{62}}$ resulted in a broad range of possible values varying between 2 eV to $24\,{\rm eV^{.62,69-72}}$ A closer look at these values indicates a linear dependence on the Sn concentration, yielding lower $b_{\rm T}^{\rm SiSn}$ for higher Sn concentrations, as concluded in references [8, 63]. Until now, a conclusive and experimentally verified bowing parameter was not found, leaving a rather large uncertainty in SiGeSn band structure calculations.

	$\mid \Gamma({ m eV}) \mid$	L (eV)	X (eV)	a (Å)	C ₁₁ (GPa)	$\mathrm{C}_{12}~(\mathrm{GPa})$
Ge	0.90	0.76	1.16	5.65	129	48
\mathbf{Sn}	-0.41	0.12	0.91	6.49	69	29
\mathbf{Si}	4.10	2.23	1.17	5.43	166	64

Table 2.1. Band structure properties at high symmetry points of Ge, α -Sn and Si at $0 \, \text{K}$, 59,62 cubic lattice constants and elastic constants from ref. [68].

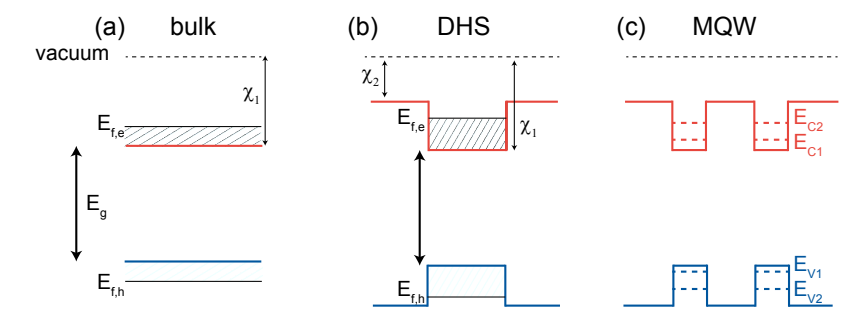


Figure 2.3. Schematic of conduction (red) and valence band (blue) of a homojunction (a), a double heterostructure (b) and a multi quantum well (c).

2.2. From Homojunction to Heterostructures

The simplest material stack design that can be grown is a homojunction, whose band diagram is schematically displayed in figure 2.3a. Energies of quasi *Fermi* levels of electrons $E_{f,e}$ and holes $E_{f,h}$ are denoted in the conduction (red) and valence band (blue). The energy needed to move an electron to vacuum is called electron affinity and labeled with χ_1 .

With the target of fabricating group IV infrared light sources based on (Si)GeSn, the development of III-V light sources serves as guidance. There, the efficiency of light emitters could be increased by using heterostructucture designs.^{73,74} In heterostructures, at least two different materials are combined, whose band alignment,

to a good approximation, depends on their electron affinities χ_1 and χ_2 . For the conduction band, the offset yields $\Delta E_C = \chi_1 - \chi_2$, while for the valence band $\Delta E_V = (\chi_1 + E_{g1}) - (\chi_2 + E_{g2})$, see figure 2.3b.⁷⁵ The band alignment sketched in figure 2.3 is called type-I band alignment, where the lower bandgap material forms the active region. If a potential is applied to this double heterostructure (DHS), electrons and holes drift from larger bandgap material to lower bandgap material which leads to accumulation of carriers in the active region. The potential well is exploited in light emitting diodes (LEDs) and laser structures to confine electrons and holes and therefore increase their overlap. This is a big advantage compared to homojunctions since the increased carrier concentration in heterostructure active regions leads to higher radiative recombination rate, as discussed later in section 2.3. This advantage is present as long as the active region does not exceed the diffusion lengths of carriers.

When the different layers are brought into contact to design a heterostructure, a space charge region builds up at the interface of the two materials with the purpose of potential compensation. This can induce an additional resistance for carrier transport. As a solution, profile grading of the barriers as well as doping can be applied.⁷⁶

The carrier concentration in homojunctions and DHSs is given by the integral of the product of *Fermi-Dirac* distribution and the density of states. The density of states $\rho^{3D}(E)$ is expressed by:

$$\rho^{3D}(E) = \frac{D^{3D}}{V} = \frac{1}{2\pi^2} \left(\frac{2m^*}{\hbar^2}\right)^{3/2} \sqrt{E},\tag{2.5}$$

with the volume of the layer V and effective mass m^* .

If the thickness of the active region is strongly reduced so that quantum mechanical effects become important, quantized states are formed confining the charge carriers additionally in z-direction. This kind of structure is called quantum well (QW). The density of states is then independent on energy for each quantized state:

$$\rho^{2D}(E) = \frac{D^{2D}}{A} = \frac{m^*}{\pi \hbar^2},\tag{2.6}$$

with A being the area of the layer. Depending on the materials and their barrier heights, quantized states appear in the conduction and valence bands, as schematically shown for type I band alignment in figure 2.3c. The energy levels of electrons in a quantum well with thickness L_z and with infinite barrier heights, can be calculated from the simple particle-in-a-box model:

$$E_n = \frac{\hbar^2}{2m^*} \left(\frac{n\pi}{L_z}\right)^2, n = 1, 2, 3, \dots$$
 (2.7)

In reality, the barriers have finite heights and the energy levels have to be found by numerical solutions. The quantized states wave functions then leak into the barrier, leading to an overlap with wave functions from neighbouring wells for multi quantum well (MQW) structures. The interaction of different wave functions influences the quantized state energy, so that splitting for each E_n occurs.

In the calculations presented in these work, the quantized states are evaluated by solving the effective-mass $Schr\ddot{o}dinger$ equation with band- and effective mass discontinuities at the interfaces accounted for. The effective masses used for the calculation of quantized states come from 8 band $k \cdot p$ calculations for each individual alloy.^{77–79}

Since the carriers' thermal energy increases exponentially with temperature, 76 the barrier heights should be $> k_B \cdot T$ to avoid carrier escape over the barrier (25 meV at room temperature), ideally hundreds of meV.

2.3. Radiative and Non-Radiative Recombination

The processes occuring in all semiconductor light emitters are the radiative and non-radiative recombinations. In this section the fundamentals of different recombination mechanisms in direct bandgap semiconductors are briefly summarized.

As the name already indicates, radiative band-to-band recombination stems from electrons in the conduction band recombining radiatively with holes (empty states) from the valence band, as schematically shown in figure 2.4a. Light matter inter-

actions include the processes of absorption, spontaneous emission and stimulated emission. In this section the focus is on spontaneous emission, the essential process for photoluminescence (PL) and electroluminescence (EL). For the generation of electron hole pairs either optical or electrical injection of charge carriers can be used.

The spontaneous recombination rate r_{sp} can be expressed as:

$$r_{sp} = B \cdot f_c \cdot f_v \cdot \rho_{\text{joint}}(E), \tag{2.8}$$

depending on the occupation probability of electrons f_c and holes f_h , determined by the *Fermi-Dirac* distribution which includes the quasi *Fermi* levels. Furthermore r_{sp} includes the joint density of states $\rho_{\rm joint}(E)$ and the transition probability B. The mean spontaneous lifetime τ is therefore defined as $\tau=1/B$. This probability B has orders of magnitudes lower values for indirect bandgap semiconductors, which implies the need for a direct bandgap semiconductor to fabricate efficient light emitters.

The emission spectrum of spontaneous emission from a direct bandgap semiconductor is shown in figure 2.4b. The high energy tail of Fermi distributions can be approximated by the Boltzmann distribution $[\propto \exp(-E/(k_BT))]$, with Boltzmann constant k_B and is also reflected in the spectrum shape. The joint density of states $\propto \sqrt{E-E_g}$ forms the lower energy shape of the spectrum. Therefore, the peak emission energy of a spontaneous emission spectrum of a semiconductor is given by its energy gap E_g , plus the temperature-dependent shift

$$E_{\text{emission}} = E_{\text{g}} + 0.5 k_{\text{B}} T. \tag{2.9}$$

Combining these terms, the total emission rate R, proportional to the intensity of the spectrum, can be written as:

$$R \propto \sqrt{E - E_g} \exp\left(\frac{-E}{k_B T}\right).$$
 (2.10)

The competing process with radiative recombination is non-radiative recombination.

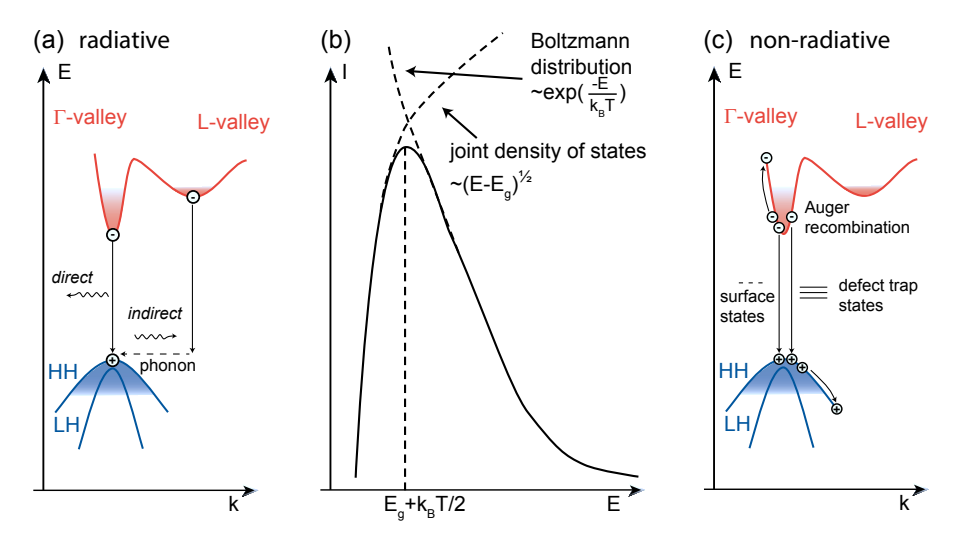


Figure 2.4. (a) Radiative recombination paths for indirect and direct bandgap recombination. (b) Theoretical luminescence spectrum from direct bandgap recombination adapted from ref. [76]. (c) Non-radiative recombination paths via surface states, defect trap states and Auger recombination.

Non-radiative recombination in semiconductors comprises all processes which do not lead to the emission of photons and therefore can be considered as carrier losses in respect to light emission efficiency. The main sources of non-radiative recombination are recombination via trap states, surface states and Auger recombination, which are pictured in figure 2.4c and will be shortly explained in the following.

In non-radiative recombination the energy of an excited electron can be converted to vibrational energy of lattice atoms, so called phonons. All crystalline point defects and lattice dislocations can serve as non-radiative recombination centers. They form localized energy states inside the bandgap of the semiconductor. Recombination via these energy states is named after its first investigators Shockley-Read-Hall recombination. The non-radiative lifetime of a charge carrier in an intrinsic semiconductor $\tau_{\rm srh,i}$ can be approximated under several assumptions as 81

$$\tau_{\rm srh,i} = \tau_{n0} \left(1 + \cosh \left(\frac{E_T - E_{fi}}{k_{\rm B} T} \right) \right), \tag{2.11}$$

where τ_{n0} is the minority carrier lifetime, and trap level and intrinsic *Fermi* energy are denoted as E_T and E_{fi} , respectively. This approximation shows the dependence of recombination time (and therefore recombination efficiency) on the trap level position, as well as on temperature. For trap levels in the middle of the bandgap, called deep levels, and for high temperatures the non-radiative recombination lifetime is smallest, resulting in less efficient emission, refer to equation 2.12.

Surface states, which originate from perturbation of the perfectly periodic lattice, are formed inside the bandgap. Ways to prevent non-radiative recombination at surfaces, are to use heterostructures, in which carriers recombine inside the active layer away from any surfaces, or by the passivation of surfaces with high quality oxides. But for both solutions the quality of the interface is essential because interface trap states can also be generated.

The last non-radiative recombination process, to be considered here, is Auger recombination, which is a three particle process, see figure 2.4c. The energy generated by a recombining electron-hole pair is used to excite an electron/hole deeper into the conduction/valence band. Therefore, the recombination rate R_{Auger} is either $R_{\text{Auger}} = C_p n p^2$ for electrons or $R_{\text{Auger}} = C_n n^2 p$ for holes. C_n and C_p are the Auger coefficients for the particular process and carrier concentrations of electrons and holes are expressed by n and p, respectively. Due to this cubic dependence, the effect of Auger recombination becomes stronger for higher carrier concentration. For low bandgap semiconductors like (Si)GeSn, Auger recombination becomes particularly important at higher temperatures. Calculations of G. Sun et al. show that Auger recombination can be a limiting factor for lasing in relaxed $Ge_{0.94}Sn_{0.06}$ above 200 K. ⁶⁹ In their calculations, the 2D density of states using MQWs helps to increase the non-radiative lifetime so that room temperature lasing could become possible. ⁸² Radiative as well as non-radiative recombination times influence the quantum efficiency η_{int} of a light emitter, which is given by:

$$\eta_{\rm int} = \frac{\tau_{\rm nr}}{\tau_{\rm r} + \tau_{\rm nr}}. (2.12)$$

Literature data about experimentally measured lifetimes in the (Si)GeSn material system is only found in the thesis of *R. Geiger* at present.⁵⁴ In this study, infrared pump-probe spectroscopy was used to determine lifetimes of GeSn with 8.5 at.% and

12.5 at.%. Values in the range between 200 ps and 400 ps were found.

In this work radiative emission spectra of different (Si)GeSn samples are analyzed in detail, and were measured in the set-up described in the following paragraph. PL spectra from unprocessed bulk and heterostructures, as well as EL spectra from various diodes are measured in a Fourier-transform infrared (FTIR) spectrometer (Bruker, Vertex v80). The sample of interest is mounted in a cold-finger cryostate, which can be cooled with liquid helium (He) to 4 K. To excite carriers in the sample, either a chopped 532 nm diode laser or a frequency modulated voltage with rectangular shape is applied with frequencies around 2 kHz. The emission is detected by a liquid nitrogen cooled indium antimonide (InSb) detector, including an optical filter with cut-off wavelength of 3 µm in front of the detector, via lock-in technique. Thus, the infrared luminescence can be separated from the thermal radiation. All spectra are measured in a step scan mode, which means that the mirrors of the interferometer are moved stepwise instead of continuously. At each mirror position, data are acquired several times in a fixed time interval. This technique allows very stable detection of emission spectra and would also allow to record time-resolved

In this chapter, the essentials of the Si-Ge-Sn material system were described, necessary to understand the results in the course of the thesis. The opposing effects of Si and Sn on the alloys, as well as the impact of lattice strain are depicted. A brief overview of the advantages of 2D heterostructures shows the reason for the research focus moving from (Si)GeSn bulk to heterostructure light emitters, prevailing the content of this thesis. The basic principles of recombination processes were also summarized as an introduction for the next chapter, on PL analysis of several (Si)GeSn designs.

processes. The generated interferogram (intensity vs. optical path difference) can be *Fourier*-transformed to obtain the final, energy-resolved, optical spectrum.

3. Photoluminescence of GeSn Alloys

Contents

3.1. GeSn Single Layer	20
3.2. GeSn/SiGeSn Heterostructures	27
3.2.1. Material Overview	28
3.2.2. Light Emission	30
3.3. Summary	35

For the investigation of optical properties of GeSn alloys, photoluminescence has often been the method of choice. Red shifted emission for increasing Sn concentrations were analyzed via PL to verify band structure calculations and relative intensity was taken as an indication for the optical quality of the layers. ^{65,83–86} Radiative recombination at Γ from a direct bandgap semiconductor increases for lower temperatures, while it decreases for an indirect bandgap semiconductor. Close to the transition from indirect to direct bandgap semiconductors, after a small intensity decrease, it increases for even lower temperatures. This temperature dependent trend has been taken as a measure for the directness of an alloy by applying a joint density of state (JDOS) model. ^{1,46}

In contrast to bulk layers, experimental results of PL from heterostructures have been hardly discussed in literature.^{87,88}

In this chapter, PL measurements of bulk GeSn layers are analyzed in terms of directness and material quality. In a second section, PL data of direct bandgap GeSn/SiGeSn heterostructures are discussed concerning carrier confinement, tem-

Thickness (nm)	strain (%)	calculated directness $\Delta E_{L\Gamma}$ (at 4 K) (meV)
46	-1.65	-45
170	-1.07	8
280	-0.48	47
414	-0.43	51
560	-0.40	53
705	-0.31	59
970	-0.34	57

Table 3.1. Sample overview of $Ge_{0.875}Sn_{0.125}$ alloys with different biaxial lattice strain.

perature-dependent light emission and quantization in 2D structures.

The results presented in this chapter have been partly published in references [1, 6, 9, 11, 63, 65].

3.1. GeSn Single Layer

A series of GeSn samples with an average Sn content of 12.5 at.% and different lattice strain is examined, see details in table 3.1. Thickness (uncertainty of ± 5 nm) and Sn concentrations (uncertainty of ± 0.5 at.%) were determined via *Rutherford* Backscattering Spectrometry (RBS), while lattice strain (uncertainty of $\pm 0.15\%$) was evaluated from X-ray diffraction reciprocal space mapping (XRD-RSM) measurements. The 46 nm layer is pseudomorphically on top of the Ge buffer. With increasing thickness, the GeSn layers start to plastically relax via formation of misfit dislocations, leading to a decrease of the compressive strain. Strain relaxation changes the band structure in a way that increases the directness $\Delta E_{L\Gamma}$, as explained in section 2.1.2. The concrete values for the set of samples discussed here, are shown in table 3.1. Over a certain thickness relaxation saturates, so that in layers approaching 1 µm, the strain does not change anymore. Details of the strain relaxation process can be found in references [63, 65, 89].

The PL spectra of all unprocessed samples were measured at various temperatures

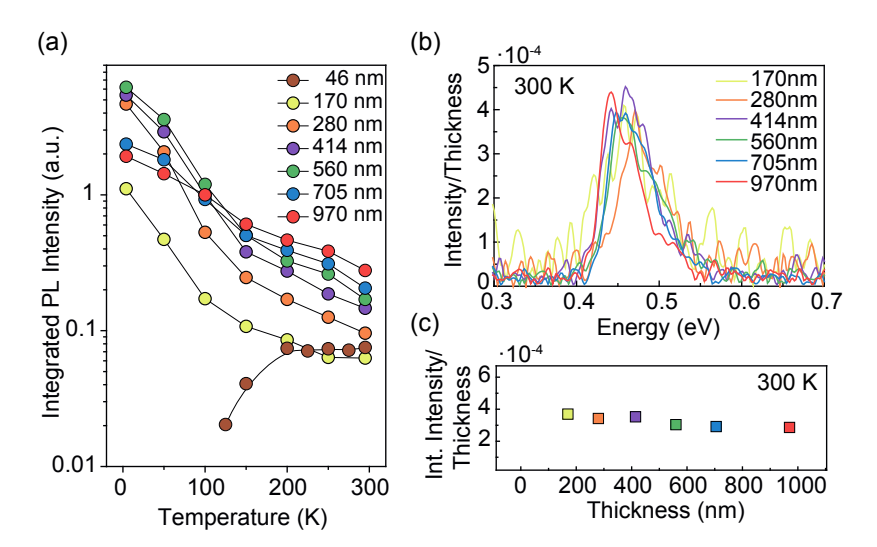


Figure 3.1. (a) Integrated PL intensities versus temperature for a series of samples with constant Sn concentration of 12.5 at.% and various thicknesses (strain). Adapted with permission from [1]. Copyright 2018 American Chemical Society. (b) Spectra of different samples normalized to their thickness show the same intensity, as well as normalized integrated intensities in (c).

between 4 K and 300 K, and the integrated intensities derived from the spectra are drawn in figure 3.1a.

At 300 K, the integrated intensity of direct bandgap samples rises with increasing layer thickness. A strong influence is caused by the amount of material itself. Carriers, excited by a 532 nm laser inside the first $\sim \!\! 50\,\mathrm{nm}$ of GeSn, diffuse through the whole GeSn layer, where they recombine. Hence, the PL intensity scales linearly with the layer thickness, which is illustrated by the spectra at 300 K normed to their specific thickness in figure 3.1b. The same is shown for the normalized integrated thickness in figure 3.1c. The normalized values stay almost constant. This indicated, the continuous increase of intensity at 300 K can be primarily associated to the amount of material, available for radiative recombination, while directness and distance to dislocations play a minor role here.

The intensity trends in figure 3.1a change when going from room temperature to lower temperature, when other contributions than the increasing thickness of the

material predominate: i) The signal of the indirect bandgap semiconductor (brownish) shows a decreasing trend with decreasing temperature. This is caused by the drop of the number of carriers at Γ , which decreases when carriers start to condense into the lowest energy states at the L-valley. ii) The direct bandgap semiconductors show the opposite behavior: with decreasing temperature, the intensity increases steadily. For thicker and more relaxed layers, $\Delta E_{L\Gamma}$ increases and the portion of electrons populating Γ rises, as it is visualized for 50 K in figure 3.2a. For a directness changing from 0 to 80 meV, the fraction of electrons in Γ increases from 25% to 100%. At the same time, the population of electrons in L drops by that amount. Simultaneously to the changing population, the non-radiative lifetime increases for the available carriers at low temperature, because SRH recombination reduces, as described in section 2.3. Regarding the JDOS model, discussed in reference [90], the non-radiative lifetime increases with a factor of 6 from 300 K to 4 K and therefore strongly influences the PL efficiency.

The trend of increasing PL intensity for thicker samples is visible down to 150 K. Then the integrated intensities of the thinner, direct bandgap layers surpass the integrated intensity of thickest layers with 705 nm (blue) and 970 nm (red). With increasing thickness the number of misfit dislocations at the interface to the Ge-VS grows as it is visible in the cross-sectional transmission electron microscopy (X-TEM) graphs in figures 3.2b-d. The 172 nm thick sample in figure 3.2b only marginally shows dislocation loops at the interface. This behavior is different to 414 nm thickness in 3.2c, where the loops already penetrate the GeSn layer. Nevertheless, crystalline quality remains high as indicated by the inset of figure 3.2c. When the thickness approaches 705 nm, the number of dislocation half loops is further increased and threading dislocations through the whole GeSn layer are observed, as visible in figure 3.2d. These degrade the direct bandgap radiative recombination efficiency, introduced previously in section 2.3, since defects can cause localized states inside the bandgap.

The temperature-dependent trend for each sample, resulting from the interplay of electron condensation in Γ and reduced non-radiative recombination, can be investigated in detail by analysis of the activation energy of these mechanisms. To extract the activation energy, the measured integrated intensity is plotted against 1000/T

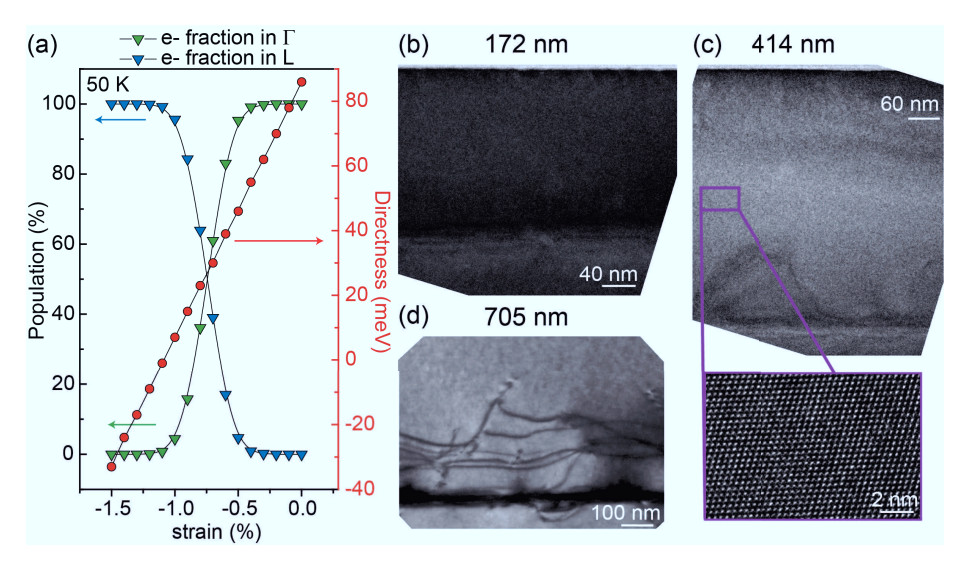


Figure 3.2. (a) Fraction of electron population inside the conduction band at Γ and at L are plotted at the left side of the graph and directness at the right side in dependence on the strain of a Ge_{0.875}Sn_{0.125} alloy. The calculation was done for 300 K. X-TEM image of the 172 nm (b), 414 nm (c) (with a zoom to show the crystallinity), and 705 nm sample (d). In thicker layers, the number of threading dislocations rises.

to be fit to an Arrhenius curve at temperatures above 100 K:91

$$I(T) = \frac{I_0}{1 + A \cdot \exp(\frac{-E_A}{k_B T}) + B \cdot \exp(\frac{-E_B}{k_B T})},$$
(3.1)

with temperature dependent intensity I(T), intensity I_0 at 0 K and Boltzmann constant k_B . A and B give a weight for different processes which are involved and which dominate at different temperatures regimes: A refers to the higher temperature and B to the lower temperature region. The corresponding activation energies E_A and E_B can be evaluated by fitting. An example of the fit is shown in figure 3.3a for the sample with 414 nm thickness. This procedure is undertaken for all relaxed layers and the extracted energy values E_A (for activation at higher temperature down to 100 K) are summarized in figure 3.3b. For the thinner layers up to a thickness of 414 nm the activation energy E_A increases, which is linked to an increasing directness. But for thicker samples, when the directness does not change much any more,

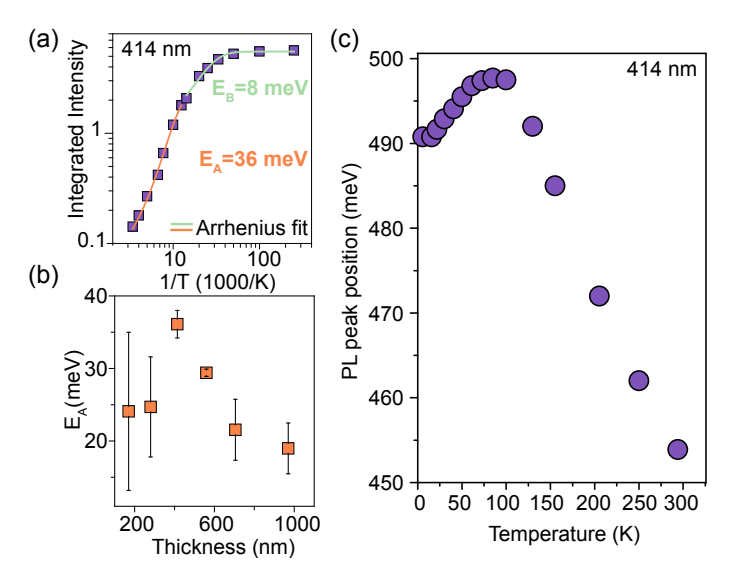


Figure 3.3. (a) Integrated intensity of $Ge_{0.875}Sn_{0.125}$ with 414 nm thickness is plotted versus 1000/T with Arrhenius fit included (orange). (b) Results from Arrhenius fit of samples with different thickness. (c) Temperature dependent peak position of PL spectra from $Ge_{0.875}Sn_{0.125}$ with 414 nm thickness. Adapted with permission from [1]. Copyright 2018 American Chemical Society.

the material quality degrades, as discussed before, and therefore a higher amount of non-radiative recombination centers is available, which leads to a decrease of the activation energies.

This analysis indicates that relaxation in thick GeSn layers can be used for increasing the directness and therefore the emission efficiency. However, the material quality degrades through mediation of defects and therefore reduces the benefit of increased directness at a certain point.

The investigation of low temperature peak positions, pictured in figure 3.3c as for the 414 nm sample, shows a noticeable feature. The temperature-dependent emission energy of semiconductors E(T) was once investigated by Y. P. Varshni, who described it with the equation: $E(T) = E_0 - \alpha T^2/(T + \beta)$, with constants α , β , while β can be related to the Debye temperature, and E_0 is the emission energy at 0 K.⁹² This formula describes well the emission from group IV Ge as well as from

III-V materials like InP, GaAs and InAs. Here, however, instead of the typical Varshni-like course of the emission energy, a decrease of peak position is detected between 95 K and 4 K of 8 meV. This energy drop fits well to the evaluated, low temperature activation energy E_B of 8 meV in figure 3.3a and can originate from localized carriers, which are trapped at energy states below the bandgap from where they recombine radiatively. These traps are likely caused by Sn vacancies, alloy fluctuations or other crystal defects. In the study of S. Gupta et al., 93 it was found that defects close the bandgap, can be more probably related to point defects than to threading dislocations since the latter ones offer rather energy valleys in the middle of the bandgap. To overcome the barrier, they need an energy of 8 meV= k_B ·90 K, which matches the temperature of 95 K from which the decrease of emission energy starts. This behavior was also observed in III-V ternaries like InGaN and InGaP and was attributed to carriers, localized "in fluctuating potentials".

Next to temperature dependent analysis, GeSn PL was investigated dependent on pump power. Power-dependent intensity I can be described by $I \propto P^m$ law, with power P and slope m. The latter gives additional information about the recombination process. In EL studies the conclusion was drawn, that it depends on the competition between radiative and non-radiative recombination: if $m \sim 1$ the emission is dominated by radiative direct bandgap recombination. Anyhow, at low carrier injection the SRH regime exhibits also an exponent of 1. For high injection the power exponent yields m=2 and the portion of non-radiative recombination is higher. It is stated, that m could be a measure for non-radiative recombination via defect states in strong direct bandgap semiconductors. 95-97 Another model, dealing with exciton recombination, attributed 1 < m < 2 to free- and bound exciton emission, while m < 1 is related to free-to-bound and donor-acceptor pair recombination.⁹⁸ The results of the power dependent analysis are summarized in figure 3.4. When increasing the laser power from 5 mW to 100 mW, the emission increases continuously, as shown for the sample with 280 nm thickness in figure 3.4a at 4 K. The slope is evaluated for all relaxed samples of the previously introduced sample series and presented in figure 3.4b in orange by a double logarithmic plot. For samples with a higher degree of relaxation, the slope decreases to values of m closer to 1, indicating that the radiative recombination rate becomes larger. This is supported by the higher directness of thicker samples, resulting in increased electron population in Γ ,

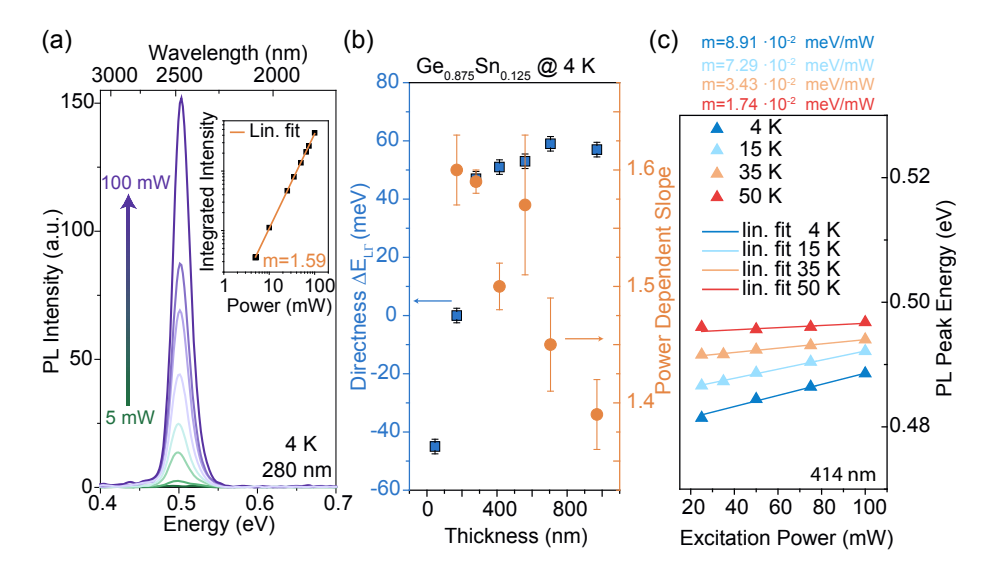


Figure 3.4. Power dependent characteristics. (a) Power dependent spectra of the 280 nm sample. The inset shows a double logarithmic plot of integrated intensities versus power and the corresponding fit. (b) Extracted slope of the power dependent excitation of various samples at low temperature is plotted in orange dependent on the thickness of the sample. The degree of relaxation changes the directness, which is shown in blue. (c) Band filling with increasing excitation power is shown by the increase of peak energy for different temperatures of the 414 nm thick sample.

leading to a rise of radiative recombination rate. Therefore radiative recombination efficiency increases leading to m closer to 1.

However, the slope for all investigated layers lies between 1 and 2 indicating a recombination dominated by SRH processes.

A further effect is observed for increasing the excitation power. The peak position of the emission shifts to larger energy with stronger pumping, as exemplarily shown for the 414 nm thick sample in figure 3.4c. This is attributed to band filling effect. At 4 K a blueshift of 7 meV is detected between 5 mW and 100 mW. With larger excitation power, the Γ valley is filled to a higher level, leading to a recombination at elevated energies. This shift of $8.9 \times 10^{-2} \,\mathrm{meV} \,\mathrm{mW}^{-1}$ decreases, when the temperature rises to 50 K. Due to the density of states ($\propto \sqrt{E}$), the number of available energy states of electrons becomes larger, the higher the quasi *Fermi* level lies

within the bands. Since the quasi *Fermi* level of electrons increases with increasing temperature, additional band filling by optical pumping becomes insignificant.

3.2. GeSn/SiGeSn Heterostructures

On the way to construct an efficient light emitter, the detailed characterization of heterostructures is inevitable. If the active region is formed by GeSn, there are several possibilities to achieve type-I band alignment with higher bandgap barrier material, like pure Ge, GeSn with lower Sn concentration or different SiGeSn ternaries. Ge as a barrier is well investigated in literature, but it is only suitable if GeSn is pseudomorphically grown on Ge, which leaves the Ge barriers unstrained. In this case, GeSn possesses the smallest bandgap at L, meaning it is indirect, and is not efficient for light emission. For direct bandgap GeSn, the Ge barriers become highly tensily strained, strongly pulling the conduction band energy downwards and reducing its bandgap, so that it does not offer a sufficient band offsets anymore. This point will be discussed more in detail, in chapter 4.

Experimental analysis of GeSn/SiGeSn heterostructures with SiGeSn barriers are so far very rare in literature. There are many theoretical studies on GeSn/SiGeSn light emitters, forecasting a promising performance due to efficient carrier confinement. Experiments with a single quantum well embedded in SiGeSn claddings, pseudomorphically grown on Ge, showed improved emission behavior compared to the single pseudomorphic layer. Nevertheless, all used active GeSn layers in this investigation exhibit the smallest bandgap at L, R7,88,99 making them to indirect bandgap semiconductors.

In the following, a direct bandgap GeSn/SiGeSn DHS as well as three different MQWs are introduced in a short material overview. They are analyzed and compared regarding emission intensity and energy via temperature dependent PL measurements.

structure name	thickness of active layer (nm)	Sn content of active layer (at.%)	cladding/ barrier thickness (nm)	Si/Sn content in cladding or barrier (at.%)
DHS	380	14.5	50	4.5/14.0 (top) 5.5/11.5 (bottom)
MQW1	$22.0 \ (\times 10)$	13.3	$22.0 \ (\times 10)$	4.8/13.0
MQW2	$12.0 \ (\times 10)$	13.5	$16.0 \ (\times 10)$	5.2/13.4
MQW3	$15.5 \ (\times 10)$	13.4	$19.0 \ (\times 10)$	5.0/13.2

Table 3.2. Overview on heterostructure samples, their thicknesses, Si and Sn contents. All these heterostructures are grown on top of a $200\,\mathrm{nm}$ thick $\mathrm{Ge_{0.90}Sn_{0.10}}$ to ensure a larger lattice template compared to the Ge-VS. Adapted with permission from [6]. Copyright 2018 American Chemical Society.

3.2.1. Material Overview

This section briefly sums up the properties of samples, which are further used in PL and lasing studies in this thesis. Four different direct bandgap GeSn/SiGeSn stacks were investigated, including one double heterostructure and three different multi quantum well heterostructures. An overview on sample thickness and Si/Sn contents in active layer and cladding(in DHS)/barrier (in MQWs) are given in table 3.2. The material characterization was done partially in collaboration with the group of *Prof. Giovanni Capellini* from *IHP* at Frankfurt (Oder).

All heterostructures follow the same concept: A 200 nm Ge_{0.90}Sn_{0.10} layer is grown on top of Ge-VS to guarantee a larger lattice as a basis for the following heterostructure. The latter is then intended to be pseudomorphic on top of the GeSn buffer to confine misfit dislocations at the interface with Ge-VS. X-TEM micrographs of all four structures are shown in figure 3.5a-d. The DHS consists of a 380 nm thick active layer with 50 nm cladding at each interface. Since the bottom cladding is grown at lower temperature than the active layer, the Si/Sn concentrations are higher/lower compared to those in the top cladding. The X-TEM of the DHS is overlayed with an energy-dispersive X-ray spectroscopy (EDX) line scan to show Si, Ge and Sn contents of each layer in figure 3.5a. A closer look to the X-TEM reveals a defective

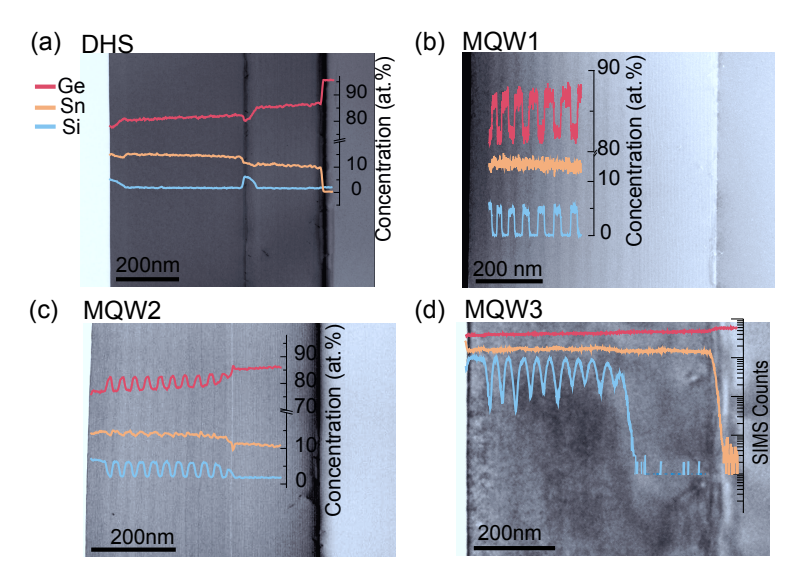


Figure 3.5. X-TEM of GeSn/SiGeSn heterostructures: (a) DHS combined with EDX line scan, (b) MQW1 combined with APT concentration profiles, (c) MQW2 combined with EDX line scan and (d) MQW3 combined with SIMS line scan.

interface between SiGeSn cladding and GeSn active layer, resulting from a further, unintended relaxation of the material stack.

Three MQWs, each with ten wells and barriers but different well/barrier thickness were grown. MQW1 with the thickest well/barrier of (22.0/22.0) nm is plotted in figure 3.5b together with the concentration profiles of an atom probe tomography (APT) measurement. MQW2 offers the thinnest well/barrier configuration with (12.0/16.0) nm in figure 3.5c together with an EDX line scan and the last sample, MQW3, lies in between with well/barrier thickness of (15.5/19.0) nm. The Sn and Si concentrations of those structures are quite similar and listed in detail in table 3.2. Defective interfaces like in the DHS are absent in all MQWs.

A more detailed material characterization of the samples can be read in references [9, 63].

structure name	$\begin{array}{c} {\rm bandgap} \\ {\rm (meV)} \end{array}$	$\begin{array}{c} \textbf{directness } \Delta E_{L\Gamma} \\ \textbf{(meV)} \end{array}$	barrier height (meV)
DHS	447	83	191/98
MQW1	509	32	79
MQW2	529	14	71
MQW3	517	26	75

Table 3.3. Band structure calculations of the different structures at 4 K determine the values for bandgap, directness of the active layers as well as the barrier height, namely band offsets between active layer and claddings/barriers. Values for MQW structures refer to the lowest quantized levels inside the active layers. Adapted with permission from [6]. Copyright 2018 American Chemical Society.

3.2.2. Light Emission

To analyze the PL data acquired from the above described samples, a further look at each band structure is relevant. The most important parameters like bandgap and directness of the active layers as well as the band offset (called barrier height) at Γ between active layer and the SiGeSn cladding/barrier are given in table 3.3. The bandgap as well as the directness of the MQWs refer to the difference between the first quantized energy levels.

The variation of bandgaps in table 3.3 stems from slightly different Sn concentrations and strain in the different structures. In the MQWs, also the energy shift due to quantization plays an important role: as described in equation 2.7 in chapter 2, the energy of the quantized states depends inversely on the squared well thickness. The energy of the first quantized states of a $Ge_{0.87}Sn_{0.13}/Si_{0.05}Ge_{0.82}Sn_{0.13}$ MQW at Γ (red) and L (blue) is exemplarily visualized in figure 3.6 by courtesy of D. Rainko. With decreasing well thickness the energy of the quantized state rises, as explained before, which results in a bandgap shift to larger bandgaps for MQWs with thinner wells. This characteristic is also observed in the bandgap values in table 3.3. Due to the smaller effective electron mass at Γ compared to L, the impact of the well thickness on the quantization shift is much stronger at Γ . This leads to a transition from a direct bandgap to an indirect bandgap semiconductor at a certain well thickness, e.g. at 5 nm in figure 3.6. The data points corresponding to the structures discussed

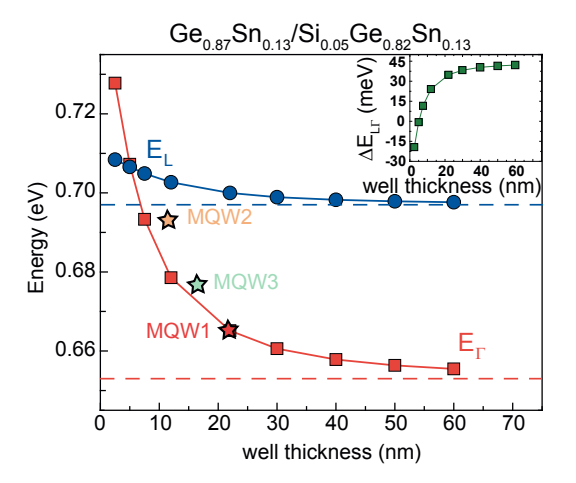


Figure 3.6. Energies of Γ and L are shown dependent on the well thickness calculated for 4 K. The difference, called directness, is shown in the inset. Courtesy of *D. Rainko*. The stars mark the calculated positions of MQW1-3.

here are shown as stars in the plot.

Since the directness is calculated from the energy difference between L and Γ , it is directly influenced by the well thickness, and also effects the directnesses of the MQW heterostructures in table 3.3, which is depicted in the inset of figure 3.6. The third parameter given in the table, the barrier height, is additionally affected by the energy shift due to quantization because it is given by the energy level difference at Γ of the active and barrier region.

The barrier heights, calculated with a SiSn bowing at Γ $b_{SiSn}=3.915\,\mathrm{eV}$, are unable to confine Γ -electrons at room temperature sufficiently, for which more than hundred meV are necessary.¹⁰⁰ The confinement of holes in the heterostructures is weaker and in the range of 56 meV to 24 meV. Nevertheless, the impact of the introduced hetero- and quantum structures is visible at low temperature.

PL spectra of all four samples are presented in figure 3.7a at 4 K (top graph) and 295 K (bottom graph). At room temperature the intensity scales with the available volume of active material, as well as with the directness of each sample. The performance of the DHS (blue), which has the highest directness and most active material available, sticks out. Since more than hundred meV are necessary to confine carriers

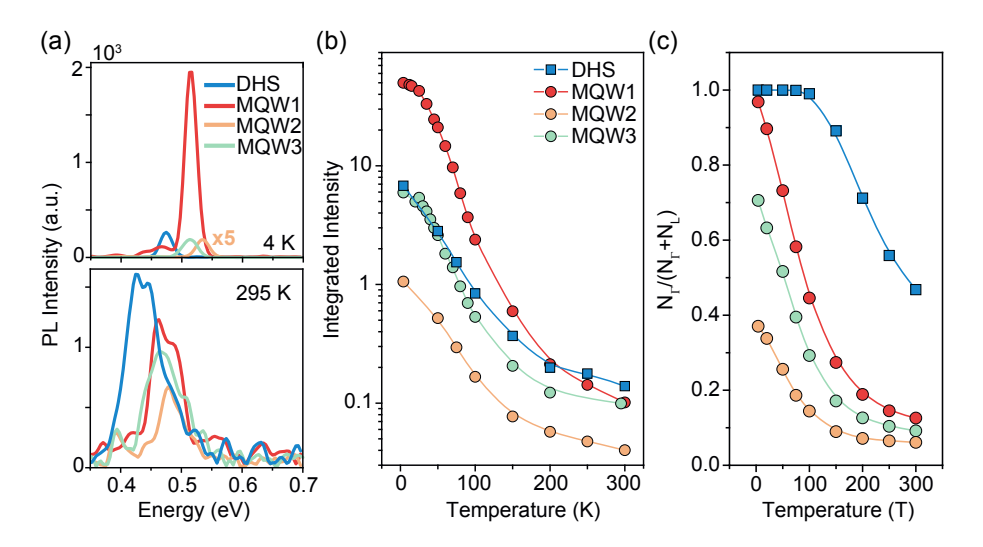


Figure 3.7. PL measurements of GeSn/SiGeSn heterostructures at room temperature and 4 K are shown in (a), the temperature dependent trend of integrated intensity in (b). (c) presents a calculation of the ration of carrier population in the Γ-valley and the total carrier population at Γ and L inside the active layers. Adapted with permission from [6]. Copyright 2018 American Chemical Society.

at room temperature to hinder the thermal carrier escape, the barrier heights of these samples have only weak influence on the emission intensity. Therefore, the emission characteristics are comparable to bulk, which can be seen in the appendix, figure A.1a. The picture changes completely when decreasing the temperature to 4 K as visible in the topmost graph in figure 3.7a. To confirm whether quantization plays a role in these structures, the peak positions can be compared to the calculated ones, specified in table 3.3. The emission of the DHS at 470 meV fits to the calculated value within the measurement errors. Comparing the calculated bandgap shift between MQW1 and MQW2 of 20 meV with their measured emission energy of 514 meV and 533 meV, respectively, the calculated quantization is in excellent agreement. The emission of MQW3 matches the emission energy of MQW1, which is not expected. However, the bandgap difference between MQW1 and MQW3 of 8 meV is hardly resolvable experimentally. Additionally, a comparison of the full width at half maximum (FWHM), which can be an indication for the homogeneity

of the material, features 23.6 meV FWHM for MQW1 and in contrast, MQW3 has the broadest spectrum with 29.5 meV FWHM. Therefore, material fluctuation together with the material parameter determination errors, may explain the behavior of MQW3.

With the evidence of emission shift because of quantization effects, the intensity characteristics at low temperature can be discussed. At 4 K MQW1 (red) exceeds the intensity of all other samples. Comparing MQW1 to the DHS the integrated intensities differ by a factor of 7.45 at 4 K, which is better visible in figure 3.7b. This behavior indicates a strongly increased non-radiative lifetime and therefore increased radiative recombination rate for MQW1. Here, the position of misfit dislocation may play a major role. The X-TEM micrographs in figure 3.5a and b show clearly the difference: MQW1 is pseudomorphically grown on top of the GeSn buffer, for DHS the active layer is adjacent to a second network of misfit dislocations because of a further relaxation of the material stack. In MQW1, the excited carriers, which are confined at low temperature to the active regions, are therefore spatially separated from misfit dislocations at the interface between the Ge-VS and GeSn buffer. Inside the DHS, excited carriers are in diffusion distance from misfit dislocations at the interface between the SiGeSn cladding and GeSn active region, which are non-radiative recombination centers.

An additional role plays the 2D density of states in the MQW structure. With the same optical excitation as for DHS, the number of carriers inside the wells per cubic centimeter is larger, enhancing the transition probability of radiative recombination. This influences the radiative recombination rate r_{sp} and time τ , meaning an increase of the former and a reduction of the latter one, compare section 2.3.

For MQW2 (orange, figure 3.7a and b) the intensity at 4 K is decreased by a factor of 47 compared to MQW1. Because of the low directness of 14 meV, the carrier population in Γ is strongly reduced compared to MQW1 resulting in lower PL emission. The effect of directness can be nicely seen for tensile strained GeSn micro disk PL, where only the directness influences the PL performance. ¹⁰¹ For the case of MQW3 the low temperature characteristic lies in between MQW1 and MQW2, as expected. In figure 3.7b the temperature dependence of integrated intensity is shown for each sample. The general trend of temperature dependent integrated intensities of a direct bandgap GeSn alloy has been already discussed in section 3.1: the intensity

decreases for increasing temperature with the change of population in Γ and the increased non-radiative SRH recombination rate. For MQW1 it is noticeable that the intensity change due to temperature is the strongest for all structures and at a temperature of 200 K, the intensity of MQW1 matches the data points of DHS.

To clarify the temperature dependent behavior, figure 3.7c shows the ratio of electron population at Γ and the total electron population in the Γ - and L-valleys for the active layer. With increasing temperature, the population decreases continuously and scales with the directness of each structure. The DHS with the strongest directness of 83 meV reveals the highest electron population in Γ at each temperature. Simultaneously, the energy barriers play an important role, because they influence the population of the whole active layer. With increasing temperature, carriers in the wells gain thermal energy, which enables them to overcome the energy barrier of SiGeSn. The lower the height of the energy barrier to the active layer, the earlier the carriers are able to escape from the well and additionally escape from the Γ - to the L-valley. Both effects, have an impact on the temperature dependent trend of integrated intensities and are responsible for the cross over point above 200 K, when the intensity of MQW1 becomes lower than the intensity of the DHS. A detailed analysis of the distribution of carrier concentration in active layer, barrier and buffer region of MQW1 and DHS was simulated by Prof. J. Witzens from IPH, RWTH Aachen University and is shown in the appendix in figure A.1b. Details of the simulation can be found in reference [6, 102].

In contrast to the bulk samples analyzed in section 3.1, none of the heterostructures show a sign of localized carriers regarding an emission energy decrease at low temperature. Due to the local confinement of charge carriers to the active region at low temperature, the carrier concentration in that region is higher compared to single layer samples. Therefore, the carrier might overflow of the localized traps which explains that no localization effect is observed in the heterostructures.

The PL characterization of GeSn/SiGeSn heterostructures reveals a promising behavior in terms of light emission for optimized MQW stacks. The investigated heterostructures showed that accurate defect engineering in terms of GeSn buffer technology, helps to strongly increase light emission at low temperature. At the same time, the example of DHS demonstrates how important it is to grow below the critical thickness of individual layers to avoid material degradation through an

additional misfit dislocation network at interfaces of heterostructures.

To benefit from a lower number of states in MQWs, the quantum wells (QWs) have to be chosen carefully: thin enough to guarantee a quantization effect, but thick enough to remain with a sufficient directness. Further evaluation of the material concerning the suitability for laser performance will be discussed in chapter 5.6.

3.3. Summary

The chapter dealt with the characterization of GeSn materials to qualify them for further optical devices. The texture of GeSn layers was analyzed by various techniques to confirm material concentration (RBS, EDX, SIMS, APT), strain (XRD-RSM) and material quality (X-TEM). These structural properties could be related to the optical features of the layers measured photoluminescence. The first section contains a detailed discussion about $Ge_{0.875}Sn_{0.125}$ bulk with different material strain. Subsequently, direct bandgap GeSn/SiGeSn heterostructures were introduced, a DHS and three different MQW designs.

The main findings are summarized in the following:

- Light emission at room temperature is limited by non-radiative defect recombination as well as the electron population in Γ which directly scales with the directness of the alloy and decreases with increasing temperature.
- By means of temperature dependent PL it is possible to examine layer quality as well as band structure (like the directness $\Delta E_{L\Gamma}$). Defects degrade the PL intensity by serving as recombination centers. So, they increase the non-radiative recombination rate by decreasing the non-radiative carrier lifetime, but their influence can be reduced at low temperature. There, the impact of the directness becomes visible via increased light emission. This was investigated at the example of a bulk $Ge_{0.875}Sn_{0.125}$ series with different thickness and strain relaxation. The higher the relaxation, the larger is the directness of the sample and therefore PL at low temperature increases. For higher strain relaxation

the number of misfit dislocation rises, leading at a certain point to a material degradation and a decrease of PL intensity.

- Analysis of activation energy in the higher temperature regime substantiate
 the above described influence of defects. Additionally, in the low temperature
 regime localized carriers caused by material fluctuations or crystal defects
 could be detected below 90 K.
- The influence of different heterostructures was investigated at low temperatures. The comparison between DHS and MQW1 revealed a strong influence of excited carriers inside the active region spatially separated from misfit dislocations. Therefore, the 2D density of states (reducing the number of states) in MQW1 as well as confined carriers away from misfit dislocations result in an emission intensity almost one order magnitude higher than in the DHS.
- At higher temperatures the benefit of confining heterostructures disappeared due to low band discontinuities between barrier and well.
- A decreased well thickness in MQW designs leads to a stronger quantization of energies at Γ and L, with a higher impact at Γ due to a lower effective mass.
 The stronger the quantization in the here used material configuration, the lower becomes the directness of the active layer, a very important parameter for efficient light emission. A careful design of MQW structures with large directness leads to structures for more efficient light emitters.

4. Light Emitting Diodes

Contents

4.1. Fabrication and Electrical Characterization	38
4.2. Homojunction LEDs	42
4.3. Heterostructure LEDs	47
4.3.1. Ge Barriers	48
4.3.2. SiGeSn Barriers	53
4.4. Summary	59

One of the main applications of a direct bandgap group IV semiconductor is the realization and integration of a light source into optoelectronic integrated circuits (OEICs). The first step from unprocessed samples, which were optically characterized in the last chapter, to electrically pumped light emitters is the design and fabrication of light emitting diodes (LEDs).

LEDs based on indirect bandgap GeSn and SiGeSn p-i-n homojunctions, or close to indirect to direct bandgap transition, have been presented in literature. ^{103–106} Electroluminescence (EL) was observed at both low and room temperature. The reports on the formation of LED heterostructures include GeSn/Ge double heterostructures ^{107,108} and a few reports on GeSn/Ge multi quantum wells. ^{2,109} Only one study up to now addresses the design of GeSn/SiGeSn MQW LEDs. ⁵

This chapter deals with various designs for light emitting diodes and their characterization. After the introduction of the fabrication process, electrical and optical properties of GeSn homojunctions are presented. These are followed by the analysis

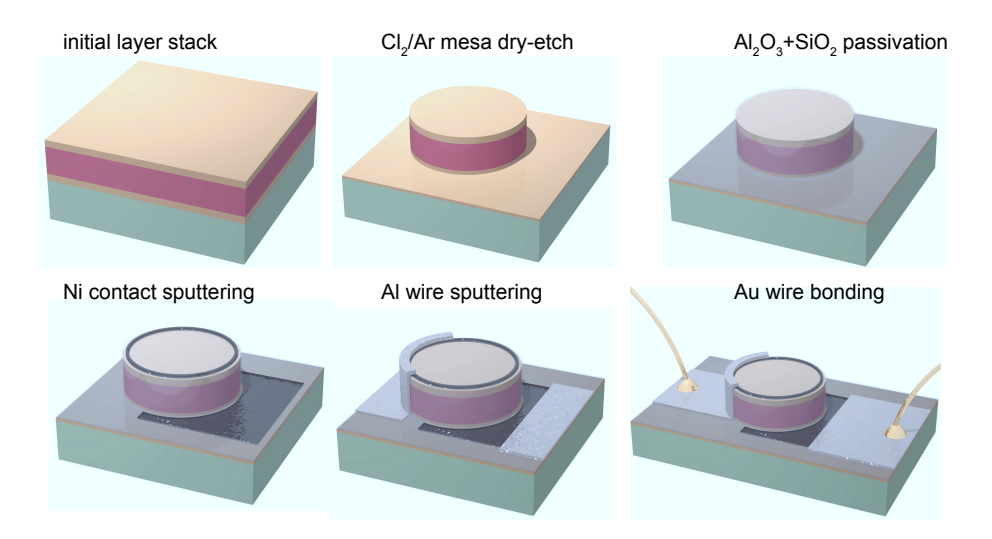


Figure 4.1. Schematic of the fabrication process for GeSn LED structures.

of a GeSn/Ge MQW LED design and a discussion why Ge is here not suitable as confining barrier material. Subsequently, GeSn/SiGeSn MQWs are characterized in depth regarding band structure and emission characteristics as well as the effect of heating.

Parts of the results presented in this chapter have been published in references [2, 4, 5, 7, 8, 10].

4.1. Fabrication and Electrical Characterization

All GeSn diodes introduced in this chapter are fabricated following the same process flow, which is schematically presented in figure 4.1. Standard Si technology, available in the $Helmholtz\ Nano\ Facility\ (HNF)$, was used. First steps include cleaning of samples with solvents, patterning by optical lithography with UV6.06 resist and subsequent development in MF24A. Circular mesas are dry etched in a Cl_2/Ar plasma in a reactive ion etching (RIE) chamber. Afterwards, the resist mask is

Sn (at.%)	$\begin{array}{c} \text{n-doping} \\ \text{(cm}^{-3}) \end{array}$	$\begin{array}{c} \text{p-doping} \\ \text{(cm}^{-3}) \end{array}$	width of i-region (nm)
8.5	4×10^{19}	3×10^{18}	318
11.0	2×10^{19}	1×10^{18}	115
13.0	5×10^{17}	5×10^{18}	485

Table 4.1. Homojunction LED properties with different Sn concentration. The doping values are evaluated by ECV measurements, which overestimate the active dopant density by roughly half an order of magnitude.

removed by acetone and isopropyl alcohol. Then the samples are passivated to reduce surface recombination and leakage currents with either 10 nm Al₂O₃ or HfO₂ by atomic layer deposition (ALD), followed by 150 nm SiO₂ deposited by plasmaenhanced chemical vapor deposition (PECVD). Next, the samples are coated with AZ nlof 2020 resist to be patterned for the first contact step. After light exposure, the resist is developed in MIF326 and contact windows are opened in the oxide by CHF₃ plasma. Then, 10 nm Ni are sputtered and locally removed via lift-off in acetone from the undesired areas. NiGeSn is formed by annealing at $325\,^{\circ}\mathrm{C}$. $^{110-112}$ Ni leftovers are removed in sulfuric acid (H₂SO₄). 200 nm Al is sputtered to ensure the wiring from the Ni contacts to larger Al bond pads. Finally, the completed LED chips are bonded with gold (Au) wires to a chip carrier with ball-wedge technique. Figure 4.2a depicts an X-TEM image of a cut through the wiring region as indicated by the white, dashed line in the inset. The GeSn p-i-n junction etched down to the doped region for the bottom contacts, passivated by Al₂O₃ and 150 nm SiO₂ and topped with Al, is visible. In the inset of figure 4.2a a scanning electron microscope (SEM) micrograph of an LED structure with 100 µm diameter is shown.

The diodes are in-situ doped during CVD growth, using phosphorous (P) for n- and boron (B) for p-doping. Material properties of three presented LEDs are summarized in table 4.1, including their doping concentration and width of the intrinsic region. The doping concentration is evaluated by electrochemical capacitance-voltage (ECV) profiling. Details regarding this method can be found in references [63, 113]. During a capacitance-voltage measurement¹¹⁴ of small bandgap semiconductors like GeSn, the inversion of minority carriers occurs already for low voltages, where Si e.g. is still in depletion. That leads to an overestimation of the carrier concentration,

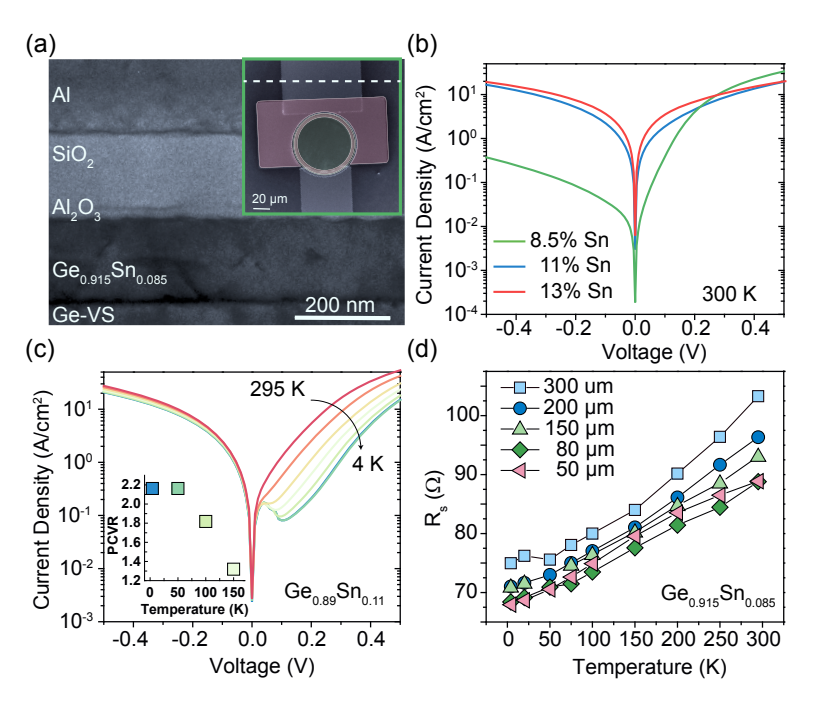


Figure 4.2. (a) An X-TEM graph trough the wire region of an LED shows the different layers, deposited during processing on top of GeSn. The position of the X-TEM record is indicated in the SEM micrograph in the inset by a dashed white line. (b) IV curves of three different diodes. (c) IV curves of Ge_{0.89}Sn_{0.11} reveal an NDR at low temperature. The PVCR is plotted in the inset. (d) Series resistances evaluated exemplarily for one material at different temperatures and diode diameters.

since the carrier concentration is derived from the depletion region. A comparison of evaluated ECV and Hall measurements reveals an overestimation by ECV of roughly one order of magnitude. For example, for a phosphorous-doped $Ge_{0.875}Sn_{0.125}$ layer, a doping of $7.7 \times 10^{18} \, \mathrm{cm}^{-3}$ was evaluated by ECV and a carrier concentration of $1.7 \times 10^{18} \, \mathrm{cm}^{-3}$ by Hall measurements.¹¹⁵

Electrical characterization is performed by current-voltage (IV) measurements. IV curves for diodes with different Sn concentrations differ strongly in their reverse behavior. In figure 4.2b, the reverse current at negative voltage for the $8.5\,\mathrm{at.\%}$ Sn diode is 1.5 orders of magnitude lower compared to the direct bandgap material diodes with $11\,\mathrm{at.\%}$ or $13\,\mathrm{at.\%}$ Sn at a temperature of $300\,\mathrm{K}$. While the current in

forward direction is dominated by excess current at low voltages and diffusion current at higher voltages, the reverse current is determined by band-to-band tunneling.¹⁰ The tunneling current in reverse direction can be approximated by:¹¹⁶

$$J_{t} = \frac{2m^{*}q^{3}\xi V_{R}}{4\pi^{2}\hbar^{2}\sqrt{E_{g}}} \times \exp\left(-\frac{4\sqrt{2m^{*}}E_{g}^{3/2}}{3q\xi\hbar}\right), \tag{4.1}$$

with the effective tunneling mass m^* , electron charge q, electric field ξ , reverse bias V_R , reduced Planck constant \hbar and bandgap E_g . Therefore, the tunneling probability and current increase for smaller effective mass and bandgap. This is exactly the case for direct bandgap GeSn alloys, since the bandgap as well as the effective masses of Γ and L decrease for larger Sn concentrations.¹¹⁷

At lower temperatures, diffusion and the excess current, caused by trap assisted tunneling, in forward direction are reduced. For the diode with the thinnest intrinsic region, this results in a negative differential resistance (NDR) at low temperatures, as visible in figure 4.2c, which is a typical characteristic of tunnel (Esaki) diodes. 118 The direct band-to-band tunneling at negative and very small positive voltages benefits from the increased Γ -valley population of just direct bandgap GeSn alloys at low temperature and processes without phonon participation. In that region, n-type conduction band and p-type valence band overlap slightly, enabling band-toband tunneling. For increasing voltages, the overlap reduces and the band-to-band tunneling current contribution diminishes before the diffusion current compensates. This results in the characteristic NDR feature. Details of simulations regarding the fractions of different currents can be found elsewhere [10, 115]. With increasing temperature, trap assisted tunneling rises, as well as the diffusion current, which leads to a decreasing peak-to-valley current ratio (PVCR) of the NDR, indicated in the inset of figure 4.2c. Our PVCR values between 2.2 and 1.2 for a relatively thick tunnel region match very well literature values of a Ge diode with PVCR between 1.43 and 1.6 and those of up to 7 in SiGe tunnel diodes. 119,120

An important diode parameter is the series resistance, which should be low. In figure 4.2d, the series resistance is evaluated, as it depends on temperature, for different mesa sizes by linearly fitting the higher voltage region of the IV curves and extracting the inverse of the slope. With decreasing diameter of the diode, the

resistance also slightly decreases. The resistance at $300\,\mathrm{K}$, which for different device sizes ranges between $103\,\Omega$ to $88\,\Omega$, drops to $75\,\Omega$ to $67\,\Omega$ at $4\,\mathrm{K}$. This is related to an increasing mobility with decreasing temperature for GeSn epilayers. While the resistance at room temperature is caused by phonon scattering processes, at low temperature defect scattering is more relevant.

In contrast to the series resistance, the parallel or shunt resistance R_{sh} of a diode should ideally be infinite. In reality, surface channels and dislocations cause finite shunt resistance values. They can be extracted by a linear fit of the IV curves at very low voltages, slightly above 0 V.⁷⁶ In the case of homojunctions with different sizes, $R_{\rm sh}$ is evaluated to be between 3300 Ω and 400 Ω at 4 K and in a range of $23\,000\,\Omega$ to $815\,\Omega$ at $300\,\mathrm{K}$, whereas the higher shunt resistances were observed for devices with larger diameter, of up to 300 µm. Side wall roughness, arising from the plasma etching process, can lead to degraded surface passivation, causing an increased number of surface states. For smaller diodes, the impact of the side walls is stronger compared to larger diodes, resulting in lower R_{sh} values for diodes with smaller diameter. The temperature dependence is also related to the electron transport process at the side walls. It might be described by hopping processes requiring a specific activation energy. The available energy is reduced by decreased temperatures, hampering the electron hopping. Evaluation of the shunt resistances reveals a serious leakage current flowing in the diodes. However, the values are comparable to those of GeSn photodetectors with 7 at.% and 11 at.% Sn. 121 Any detailed analysis about characteristic resistances of GeSn diodes is missing in the literature.

4.2. Homojunction LEDs

After the electrical properties of GeSn diodes were shortly discussed, this section is dedicated to light emission of homojunction LEDs. Material strain, bandgap and directness of previously introduced LED layers are summarized in table 4.2. With increasing Sn concentration in the layers, the bandgap is lowered and the directness is enlarged. However, even for the sample with the lowest Sn concentration

Sn (%)	strain (%)	bandgap (meV)	${\rm directness}({\rm meV})$
8.5	-0.18	620	0
11.0	-0.67	560	6
13.0	-0.59	500	46

Table 4.2. Band structure properties of homojunction LEDs at 4 K.

of 8.5 at.% with low residual strain of -0.18%, the energy at Γ and L is the same, resulting in a directness of 0 meV at 4 K.

Before the three kinds of diodes are compared, a detailed view on the Ge_{0.89}Sn_{0.11} diode with a diameter of 100 µm is presented. Figure 4.3a shows temperature dependent EL spectra at a roughly constant current density of 275 A cm⁻² between 295 K and 4 K. A clear intensity increase at lower temperatures is observed, comparable to the PL intensity behavior in section 3.1. The EL intensity at 295 K, in the inset of figure 4.3a, increases linearly for higher current densities between 123 A cm⁻² to 590 A cm⁻², indicating a dominant band-to-band recombination. 122 Normalized power dependent spectra at 4 K are plotted on a semi-logarithmic scale in figure 4.3b to fit the high energy tail of the spectra, $\propto \exp(\frac{-E}{k_B \cdot T})$, for extraction of the carrier temperature of recombining electrons. 109,123 Figure 4.3c sums up the derived values at 4 K and 295 K. In general, the extracted electron temperatures are higher than the junction temperatures due to high injection levels and reveal an upper limit of the real junction temperature [76]. By rising the current density, the electron temperature increases. At 4 K the raise of absolute carrier temperature compared to ambient temperature is not as strong as at 295 K, since cooling with a high He flux in the cryostat partially compensates the heating.

Normalized spectra of diodes with different Sn concentration and a diameter of 100 µm are juxtaposed in figure 4.4a. For higher Sn content, the emission shift to lower energies, and therefore, smaller bandgap, is clearly visible. Peak positions of the emission energy are plotted against the whole temperature range in figure 4.4b, while the legend for the complete figure can be found above figure 4.4d. The change in emission energy at higher temperatures is due to the temperature dependent lattice dilatation, which induces a linear change in band structure with temperature. But at lower temperature, the change of energy bands is mainly caused by

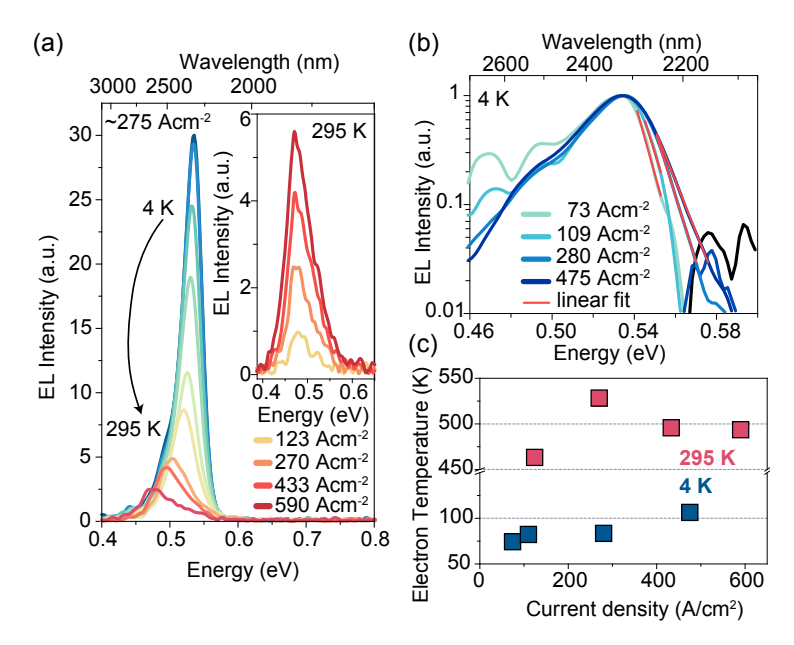


Figure 4.3. EL spectra of a $Ge_{0.89}Sn_{0.11}$ LED. In (a) temperature dependence at $275\,\mathrm{A\,cm^{-2}}$ is shown, while power dependent spectra at $295\,\mathrm{K}$ are plotted in the inset. Power dependence is analyzed in (b) at $4\,\mathrm{K}$ by a semi-logarithmic plot. The electron temperature is extracted by linearly fitting the high temperature tail and the results are shown in (c).

the electron-phonon (lattice) interaction. 92 One empirical model for the behavior of emission energy dependence describes the temperature shift by electron-phonon interaction with the Bose-Einstein occupation rule. 124,125 This model was shown to describe the trend of emission energy more accurately than Varshni's model in the low temperature regime. Here, the simplest version, applying one oscillator, is used 126

$$E(T) = E_0 - \frac{2 \cdot a}{\exp(\theta/T) - 1},$$
 (4.2)

where E_0 is associated to the bandgap energy at 0 K, a is the strength of the electronphonon interaction and θ represents the average phonon energy. The extracted parameters are listed in table 4.3. While the energy gaps match quite well the calculated ones in table 4.2 and parameters a and θ are of the same order of magnitude

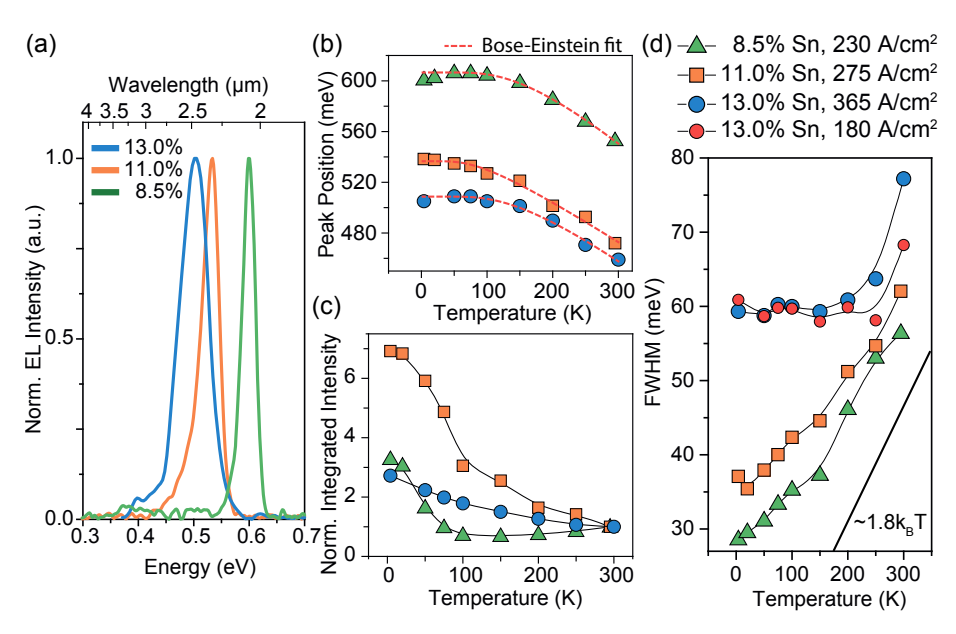


Figure 4.4. A comparison of LEDs with different Sn concentration. Normalized spectra are shown in (a). In (b) peak energies are plotted against temperature together with a Bose-Einstein fit for peak position and (c) depicts the integrated intensity normalized to room temperature. The peak width dependence on temperature is shown in (d).

as those fitted to different transitions in Ge by *Vina et al.*[127], at low temperature there is still a deviation from the fit. As already explained in section 3.1, the slight decrease in emission intensity might be due to carrier localization in regions with higher Sn concentration. This effect can only be hardly noticed and therefore, should not have a great impact.

In figure 4.4c, integrated EL intensities are normalized to that at 295 K so that the relative intensity rise can be compared. For the 8.5 at.% diode in green a small intensity decrease is apparent, which is typically observed for indirect bandgap semi-conductors. With our calculations, the sample has a directness of 0 meV at 4 K. However, due to errors in the estimation of Sn content and strain and the resulting band structure calculation, the sample might be slightly indirect. In any case, the carrier occupation of the Γ valley is smaller than that of L, since the density of

Sn (%)	E_0 (eV)	a (meV)	$\theta(\mathbf{K})$
8.5	0.61	126	511
11.0	0.54	45	267
13.0	0.51	96	469

Table 4.3. Fitting parameters of *Bose-Einstein* fit for peak energy.

states is larger in the latter, which limits the amount of carriers available for direct bandgap radiative recombination. In the higher temperatures range, the sample is more direct $\Delta E_{L\Gamma} = 14 \text{ meV}$, causing the slight decrease of intensity with decreasing temperature due to reduced directness. At temperatures below 100 K, non-radiative SRH recombination starts to be suppressed. This increases the non-radiative lifetime and leads to a stronger increase of emission intensity at low temperature. For the diode with 11.0 at.% Sn (orange), the calculated directness of 6 meV is still quite low due to a high compressive strain, which cannot be released in a layer thickness of only 265 nm. Therefore, the carrier distribution between Γ and L and the change with decreasing temperature results in a continuous, intensity increase. Compared to the diode with 8.5 at.%, this sample exhibits the behavior of a direct bandgap semiconductor, since the intensity drop at higher temperatures is missing. In contrast to the previously discussed diodes, the LED with 13.0 at. % Sn offers a strong directness of 46 meV, which means that a larger percentage of carriers at 295 K already reside in the Γ-valley and should result in an overall enhanced emission intensity, which cannot be observed. Compared to the 11.0 at.% diode, the relative intensity rise of this diode (blue) is much lower. Both aspects indicate a strong influence of defects, decreasing the non-radiative recombination time and explaining the deteriorated light emission. Additionally, the n-doping level is lower in this diode and the series resistance is found to be roughly $100\,\Omega$ higher than in the 8.5 at.% diode in section 4.1. Therefore, the electron temperature at an ambient temperature of 4 K is evaluated to be in the range of 160 K to 200 K at current densities below 200 A cm⁻², indicating a pronounced Joule heating.⁷⁶ According to the electronic properties, as well as the higher number of defects, the distinct intensity increase, which can be found for the other diodes at ambient temperature of 100 K, is missing.

In contrast to the electron temperature at 4 K, at 300 K the values lie between 320 K to 420 K. It means that the absolute temperature rise is smaller at room temperature, opposite to the behavior shown in figure 4.3c. This behavior can be related to the temperature dependence of the series resistance, which is almost constant in this diode, causing a stronger heating at low temperature compared to the other devices. Furthermore, the non-radiative recombination rate seems to be higher in this device, refer to figure 4.4. In non-radiative recombination processes, energy of the recombining charge carrier is converted to lattice vibration, which produces additional heat. The effect of higher electron temperature on the 13.0 at.% diode is also visible in the full width at half maximum (FWHM), which is shown in figure 4.4d. Up to a temperature of 200 K, the FWHM is constant, independent on the ambient temperature for two different injection current densities. At higher ambient temperature the width starts to increase. Therefore the influence of the resistance seems to dominate up to a temperature of 200 K. At that point, the FWHM at an injection of 180 A cm⁻² drops below that at 365 A cm⁻². An overall larger FWHM for this device at two different current densities, points to a stronger heating in this device. Further reasons for a broader spectrum of LEDs with higher Sn concentration are the presence of radiative recombination at defect states close to conduction or valence band. Regarding the other two diodes, the FWHM rises continuously with temperature. The higher temperature behavior corresponds to the theoretical, linear trend, which can be expressed as $\propto 1.8 k_B T$, without taking into account any heating and is illustrated by the black line.⁷⁶

To improve the light emission properties of a semiconductor light emitter, the application of heterostructures is inevitable. Therefore, in the next section different heterostructure designs are characterized and discussed.

4.3. Heterostructure LEDs

Boosting the LED's performance is a universal target for all light emitters. As already discussed, the application of heterostructures can change the band alignment in a beneficial way, by confining the electrons to the active regions and therefore

reducing the losses originating from diffusing carriers into buffer material or defective regions. Additionally, the number of states can be reduced by application of quantum structures, which is advantageous in terms of efficiency and therefore of the reduction of power consumption. In this section the suitability of Ge and SiGeSn as barrier material is studied for indirect bandgap LED structures with a Sn concentration of 8.5 at.%.

4.3.1. Ge Barriers

In literature a few studies of GeSn/Ge heterostructures have been reported. Schwartz et al. 109 show for a pseudomorphically grown GeSn/Ge quantum well with 7 at.% Sn that the design offers a quantum confinement with the drawback of indirect bandgap active material with $-60\,\mathrm{meV}$ directness. Furthermore, a study of Ge/GeSn/Ge DHS grown on Ge-buffered Si with indirect bandgap material and Sn concentrations up to 9 at.% confirms a type-I band alignment between Ge and GeSn with band offsets between $11\,\mathrm{meV}$ to $47\,\mathrm{meV}.^{108}$ These are first GeSn heterostructures, but the confinement is still not strong enough and further improvement is mandatory.

In this section, another GeSn/Ge MQW LED is characterized, before a general conclusion about Ge as barrier material is drawn. In contrast to literature studies, the GeSn layer is partially relaxed and not pseudomorphically grown on Ge offering a lower bandgap and a larger directness of the active material.

First, a p-doped 115 nm thick $Ge_{0.92}Sn_{0.08}$:B layer is grown, which ensures a partial strain relaxation on top of the Ge-VS. The doping concentration was extracted from ECV to be 4×10^{18} cm⁻³. Thereafter, an MQW structure follows, consisting of 7 periods of $Ge/Ge_{0.92}Sn_{0.08}$, each with 14 nm barrier and 20 nm well thickness, respectively. Finally, the top cladding is formed by 60 nm n-doped $Ge_{0.92}Sn_{0.08}$:P with a doping concentration of 7.5×10^{19} cm⁻³ (determined by ECV). An X-TEM is overlaid with a SIMS measurement in figure 4.5a, confirming the clear separation between well and barrier material. To determine the strain inside the layer stack, XRD-RSM of the (224) reflection was performed, revealing an equal in-plane lattice

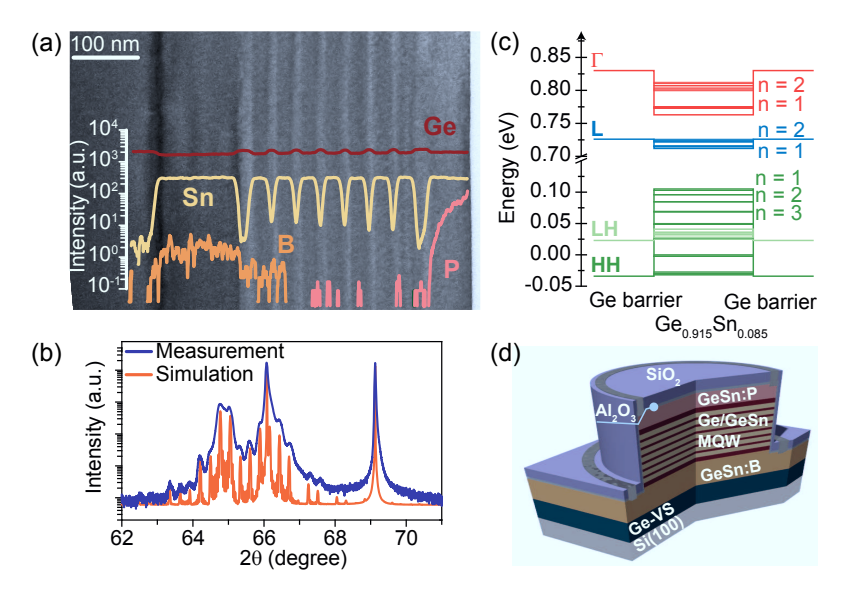


Figure 4.5. Structural characteristics of a GeSn/Ge MQW. (a) An X-TEM is overlaid with a SIMS profile of the GeSn/Ge MQW. (b) XRD $\theta - 2\theta$ scan (blue) matches the simulation (red) by courtesy of *G. Mussler*. (c) Band structure calculation at 4 K shows a weak confinement of electrons in Γ and L. (d) A schematic of the processed LED. Adapted with permission from reference [2], OSA Optics Express.

constant for the wells as for the GeSn:B layer. This pseudomorphic growth results in $-0.71\,\%$ compressive strain inside the GeSn layers and $0.48\,\%$ tensile strain inside the Ge barriers. To clarify whether the observed satellite peaks are in agreement with expectations, a $\theta-2\theta$ scan around the (004) reflex is compared to a simulation in figure 4.5b, from which the thickness as well as Sn concentrations were derived, matching the experimental evaluated data. Calculated band structure alignment is shown in figure 4.5c for 4 K. The confinement inside the conduction band provided by this kind of heterostructure is 57 meV at Γ and at the valence band 137 meV for heavy and 13 meV for light holes. At L, the electrons are less confined with a band offset of 12 meV. The semiconductor is indirect with a difference between L and Γ of -58 meV. The offsets are always calculated between the first quantized states of the well and the bulk band edge of the barrier. If calculations are carried out at room temperature the confinement diminishes. At L, type-I band alignment is lost,

MQW structure	strain (%)	$E_g \pmod{\mathrm{meV}}$	$\Delta E_{L\Gamma}$ (meV)	$\begin{array}{c} \textbf{barrier height} \\ \textbf{at } \Gamma \\ \textbf{(meV)} \end{array}$
${\rm Ge_{0.920}Sn_{0.080}/Ge}$	-0.71	670	-58	57
$\rm Ge_{0.914}Sn_{0.086}/Si_{105}Ge_{0.786}Sn_{0.109}$	-0.24	639	-17	161

Table 4.4. Material and band structure properties of heterostructure MQW LEDs at $4\,\mathrm{K}$.

and actually carriers are slightly confined inside the barrier.² Material and band structure properties are summarized in table 4.4. A schematic of a processed device is depicted in figure 4.5d. The material stack with doped layers and MQW is visible in the incised mesa. It is etched down around the mesa to the GeSn:B region, so that the metal, drawn in black, contacts the doped GeSn layers at the bottom and top. Passivation layers are indicated in orange and blue. The following evaluation refers to devices with 100 µm diameter.

The emission intensity measured at 4 K for current densities between 25 A cm⁻² and 620 A cm⁻² in figure 4.6a increases with higher current injection. With rising current densities, the energy states at Γ are filled up to a higher energy, broadening the spectra, as it is displayed in figure 4.6b. The trend of higher emission energy with increasing current density for the limited current density range in figure 4.6c confirms the explanation of increasing spectral width due to band filling. Additionally, the electron temperatures, extracted at an ambient temperature of 4 K, are in a similar range, from 51 K to 113 K, as for the homojunction LED in figure 4.3 (in the same current density range). This effect also influences the FWHM and seems to be the dominant reason for the much slower increase at current densities above 200 A cm⁻², when the peak position remains constant. So, in view of the above two aspects, the trend of FWHM dependence on current density can be well understood. At second glance, the emission energy for all current densities in figure 4.6c is more than 50 meV smaller than from the calculations. In contrast, the deviation between emission energy at low temperature and bandgap calculation of homostructures is just around 20 meV. Variations of Sn content and strain along the wafer cannot result in a deviation to lower emission energies, since material parameters are always determined from wafer center with the highest Sn concentration. A systematic error of the calculations is expected to have the same influence on all structures and can be therefore excluded in this case. The only difference for the MQW are the quantized energy levels. These quantized levels can be overestimated, when the interplay between valence bands close to each other, like heavy and light hole, are not considered. Since these values are only in the range of a few meV, they do not have such a strong impact. That raises the question of the emission origin, which is discussed next.

To gain more insight, a look at the temperature dependence can be helpful. Temperature dependent FWHMs in figure 4.6d show a comparable value to homojunctions at 4 K. But at 300 K, values between 70 meV to 80 meV are reached, for comparable current densities, which is more than 20 meV broader than for the homojunction. Emission from recombination at L is expected to occure at a lower energy than emission from Γ . The bandgap at L is calculated to be 612 meV at 4 K. Therefore, emission from two different recombination processes might overlap and be responsible for one broad peak, especially at room temperature. Another indication gives the integrated intensity in figure 4.6e, which increases at lower temperatures for all investigated current densities. In general, a rise of intensity with lower temperature, associated to radiative transitions at Γ of direct bandgap material, is caused by condensed carriers inside the Γ -valley at decreasing temperatures. In the case of an indirect bandgap semiconductor, the Γ-valley can only be filled if enough electrons are injected. On the other hand, the transition at L is an indirect transition, relying on available phonons to enable radiative recombination, which decrease when temperature is very low. However, recombination at L and at Γ benefits from the increase of non-radiative recombination times with decreasing temperature, by reduced rate of defect-assisted recombination, leading to higher emission efficiencies at low temperatures. Finally, these components' interplay is crucial for the radiative characteristics.

In literature all EL peaks for comparable Sn concentration are attributed to radiative transitions at Γ , 105,108,128 only one group reports distinct emission from Γ and L. 107 The indirect single quantum well LEDs in ref. [108] show only emission from Γ with decreasing intensity at lower temperature. This is opposite to the behavior found here. For bulk Ge, an increase of PL emission intensity at lower temperatures is observed and attributed to transverse optical phonons. 123

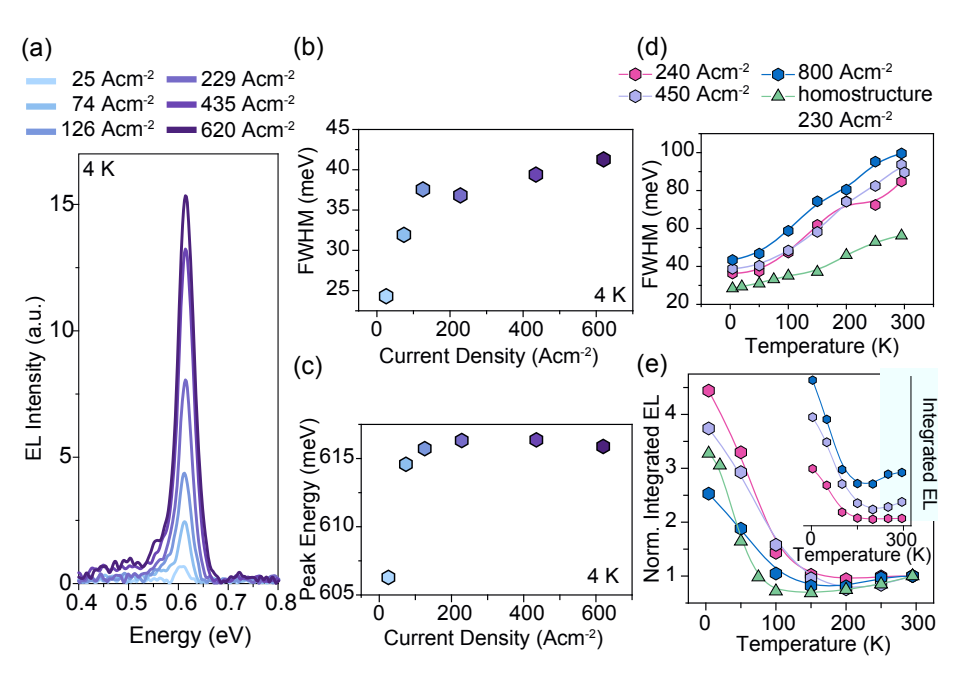


Figure 4.6. Optical characteristics of a GeSn/Ge MQW LED. (a) EL spectra at 4 K for different current densities. From these spectra width (b) and emission energy (c) are evaluated. (d) Temperature dependent trends of spectral width (d) and of integrated PL intensities in (e) are displayed. Adapted with permission from reference [2], OSA Optics Express.

At last, the emission from tensile strained Ge can be considered, but since the bandgap is over 700 meV, this can be excluded as origin for the here observed emission. Anyhow, in this case it is not completely clear which recombination is observed here, but the broad FWHM indicates a superposition of recombination from Γ and Γ .

The trend of integrated intensity with temperature is illustrated in figure 4.6e and will be now further discussed. By direct comparison of integrated intensities, indicated in the inset of figure 4.6e, higher carrier injection leads to a higher emission intensity. This is due to the amount of carriers, available for radiative recombination. Data points in the actual graph are normalized to room temperature for different current densities and therefore show the relative intensity enhancement.

As the current density is enlarged, the relative intensity enhancement reduces, visible for $450\,\mathrm{A\,cm^{-2}}$ (lilac points) and $800\,\mathrm{A\,cm^{-2}}$ (blue points). For high injection current densities, a higher number of carriers is available at room temperature for radiative recombination. At $4\,\mathrm{K}$, the carriers condensate in Γ , which has a higher impact for lower injection current densities, since fewer carriers are available from the start. Therefore the benefit of the change in population at Γ is larger for lower carrier injection. This phenomenon can be described by the JDOS model, resulting in a similar order of magnitude of the relative intensity change. 46,63 In this modelling recombination times are left constant as a first approximation. Consequently, loss mechanisms like SRH recombination or Auger recombination, which become stronger for higher carrier injection, do not dominate the trend here.

A further comparison of the relative intensity trend for the homostructure with 8.5 at.% Sn is included (green triangles), revealing no advantage of this GeSn/Ge MQW design. In a comprehensive study of Ge as barrier material, especially for direct bandgap GeSn, it turned out that due to a high tensile strain in Ge barriers, the confinement is always limited.² Only a small region in a wide parameter range leads to type-I alignment in a direct bandgap well material. But even in this region, barrier heights will never surpass a limit of $E_{\rm barrier} < 1.5 k_{\rm B}T$ at higher temperatures which is not sufficient for effective carrier confinement.

4.3.2. SiGeSn Barriers

After it was found that Ge is not appropriate for efficient carrier confinement, studies concentrated on GeSn/SiGeSn heterostructures. Hence, a multi quantum well stack is grown on top of a 280 nm thick $Ge_{0.914}Sn_{0.086}$ buffer leading to a residual strain in $Ge_{0.914}Sn_{0.086}$ wells of -0.24% and in $Si_{0.105}Ge_{0.786}Sn_{0.109}$ barriers of -0.09%. 60 nm below the first SiGeSn barrier, n-doping of 3×10^{19} cm⁻³ is applied. After seven periods of barrier/well with 11 nm/19 nm width, respectively, the structure is finished by a last barrier and a p-doped GeSn top layer. Here, the doping concentration amounts to $7 \times 10^{18} \text{ cm}^{-3}$. The elemental distribution throughout the layers was evidenced by atom probe tomography and elemental maps of the different atomic

species are displayed in figure 4.7a-e. Sn concentration of $8.6\,\mathrm{at.\%}$, Si of $10.5\,\mathrm{at.\%}$ in the barrier and Sn $10.9\,\mathrm{at.\%}$ are extracted from this measurement. In figure 4.7f concentration profiles of the central well/barrier region are plotted, revealing the variation of Sn concentration between wells and barriers.

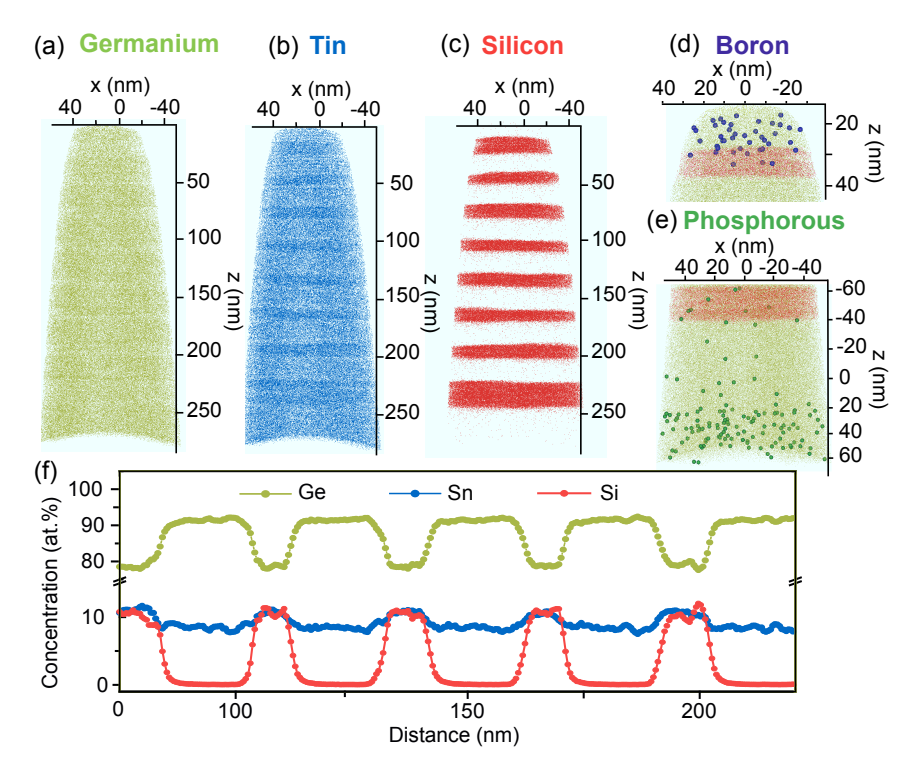


Figure 4.7. APT elemental maps of (a) Ge (b) Sn (c) Si (d) B and (e) P. A line scan of Ge, Sn and Si shows the elemental concentrations through the layer stack. Adapted with permission from reference [5], OSA Optica.

The band structure calculations for SiGeSn include a strong uncertainty on the bowing parameter b_{SiSn} as explained in section 2.1.3. Similar to the calculations in section 3.2 about PL from heterostructures, in this case $b_{SiSn} = 3.915 \, \text{eV}$ is used. The calculated band structure is depicted in figure 4.8a for 4 K asserting that type-I

band alignment is present. Si, Ge, Sn concentrations and strain are summarized in table 4.4 together with the resulting band alignment (for the first quantized states, close to the bulk band edge). Due to the Sn concentration of 8.6 at.% in the GeSn wells and to the low residual compressive strain, the active regions are slightly indirect with a directness of $-17\,\mathrm{meV}$. The confinement for holes is weaker, compared to electrons, and amounts to $47\,\mathrm{meV}$ and $24\,\mathrm{meV}$ for heavy and light holes, respectively. Bandgap and directness are strongly affected by energy quantization, which furthermore critically depends on the SiGeSn barrier heights, calculated with b_{SiSn} . For bowing parameters larger than 3.915 eV, the barrier height drops and the quantization effect becomes smaller. For example, a value of $b_{\mathrm{SiSn}} = 19\,\mathrm{eV}$, instead of 3.915 eV, results in a reduction of the barrier height at Γ of 160 meV at room temperature.⁵ That would cause an increase of 13 meV and 36 meV of the directness and bandgap, respectively. Hence, the chosen bowing parameter can overestimate barrier height, bandgap and directness.

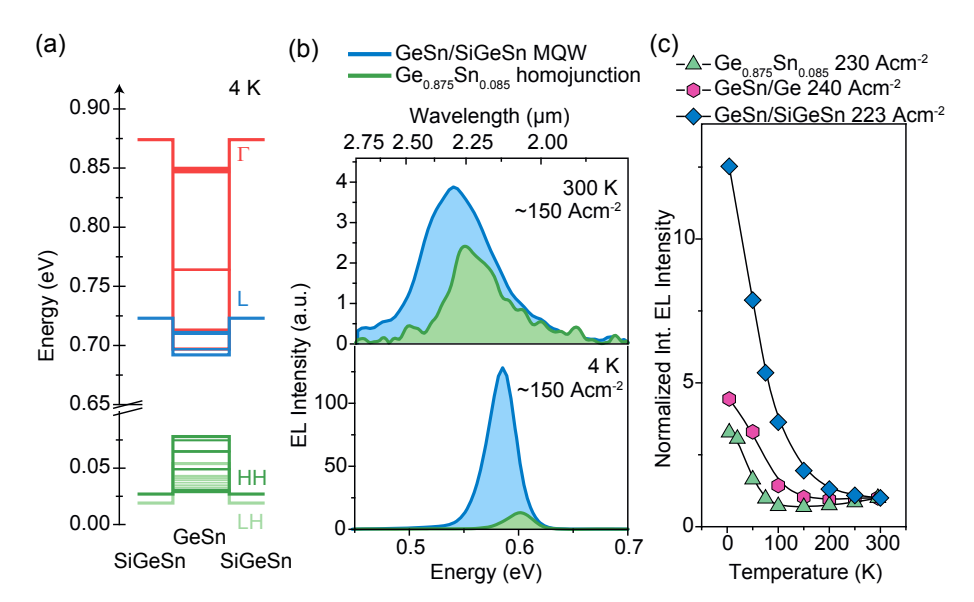


Figure 4.8. (a) Band alignment of the GeSn/SiGeSn MQW LED stack with a bowing parameter of $b_{SiSn}=3.915\,\mathrm{eV}$ shows strong confinement for electrons in Γ for a slightly indirect bandgap material. (b) Comparison of a GeSn homojunction and the GeSn/SiGeSn MQW LED at 300 K (top) and 4 K (bottom) for similar current densities and Sn concentrations.(c) Temperature dependence of integrated EL intensities shows the difference between two MQW designs and the homojunction. The data are normalized to their intensities at 300 K. Adapted with permission from reference [5], OSA Optica.

Spectra at $300\,\mathrm{K}$ (top) and $4\,\mathrm{K}$ (bottom) are illustrated in figure 4.8b in blue for an injection current density of $150\,\mathrm{A}\,\mathrm{cm}^{-2}$ in comparison to the homojunction with $8.5\,\mathrm{at.\%}$ discussed in section 4.2 (green). The emission energy of the homojunction is $15\,\mathrm{meV}$ blue shifted compared to the heterostructure emission. This trend does not match the band structure calculations, however, the errors of measured Sn and strain values and the variation over the whole wafer lead to deviations of the bandgap of $15\,\mathrm{meV}$ and might be the reason for that.

In contrast to all other investigated LEDs, the overall emission is stronger for the GeSn/SiGeSn MQW sample. Already at room temperature, the emission of the

MQW LED is stronger even though the calculated directness is slightly below that of the homojunction (-17 meV versus 0 meV, respectively). This enhancement results from the impact of barriers, which start to screen carriers from the defective GeSn/Ge-VS interface. Secondly, the carrier density inside the wells is higher compared to the homojunction due to smaller volume of active material, leading to increased radiative recombination. At low temperature the benefit is even more evident, which is pointed out in figure 4.8c, where the temperature dependent trend of integrated intensities for the homojunction, the GeSn/Ge MQW and the GeSn/SiGeSn MQW are provided. All intensities are normalized to 300 K, so relative changes can be compared. Data for the homojunction and for the GeSn/Ge MQW LED are known from the latter section. At 4 K the impact of the barriers is stronger, because carriers have a lower thermal energy to overcome barriers or to transfer to L. The steep increase of GeSn/SiGeSn LED's intensity is attributed to an increase of emission efficiency by the increase of non-radiative recombination times. Carriers at low temperature are completely prevented to reach the defective interface between Ge-VS and the GeSn buffer, which in turn increases non-radiative recombination times. All these aspects lead to the superiority in light emission yield of GeSn/SiGeSn MQW compared to both of the other 8.5 at.% Sn structures. A more detailed evaluation of the GeSn/SiGeSn EL is demonstrated in figure 4.9. Peak positions shift to lower energies for increasing injection current densities in figure 4.9a. The shift increases for rising temperatures from 2.5 meV to 20 meV, at 4 K and 300 K, respectively. At 4 K the peak energies are similar for any pumping power and the change in energy, converted to equivalent temperature by $E_{\text{emission}}/k_{\text{B}} = T$, equals 29 K. In contrast, at 300 K a reduced emission energy for stronger pumping indicates a heating of 232 K of the device. The calculation is not entirely valid, since different effects like bandgap renormalization due to exchange-correlation effects in electron-hole plasma by strong pumping ^{129,130} can reduce or band filling can also increase the emission energy. For the same current densities as in a, the spectral width is displayed in figure 4.9b. At low temperature, the width is comparable to direct bandgap emission from GeSn/GeSn single quantum well LEDs in ref. [128]. Since the LED presented here still has an indirect semiconductor as active material, the peak broadens at elevated temperatures due to possible contributions from radiative recombination at L. To investigate the spectral broadening a bit further, electron

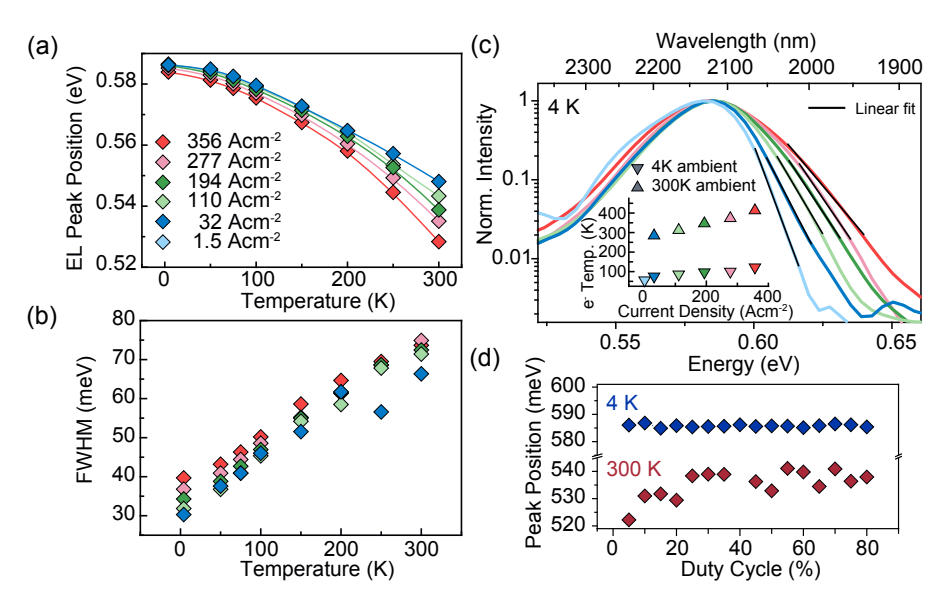


Figure 4.9. (a) Peak positions of the emission at different injection current densities are plotted dependent on temperature. (b) For the same current densities the spectral width was evaluated. (c) For further insight, electron temperature is extracted at different pumping and for two temperatures, 4 K and 300 K in the inset. (d) Dependent on the duty cycle, the peak positions does not reveal significant heating of the device for longer pulses.

temperatures for spectra at 4 K (see figure 4.9c) and 300 K are evaluated by a linear fit of the high energy tail \propto k_BT, like in section 4.2. The extracted temperatures are plotted in the inset of figure 4.9c for two different ambient temperatures. Here the temperature change at 4 K ambient temperature amounts to 47 K for different injection levels, a stronger deviation from the value calculated from the peak positions. Therefore band filling, i.e. level filling in MQWs, seems to influence the peak position at low temperature counteracting the red shift due to heating. At 300 K the change in electron temperature with increased pumping is 129 K, which is in this case 100 K below the temperature calculated from the peak position shift. This might be related to contribution from radiative recombination at L, which is not apparent at low temperature.

As a last point, the peak position is analyzed as it depends on the duty cycle (DC).

The carrier injection in all measurements is pulsed with a duty cycle of 50 %. In figure 4.9d the emission energy dependence on the duty cycle is plotted at 4 K (blue) and 300 K (red). When the sample in the cryostat is cooled to 4 K and charge carriers are confined in Γ , the peak position is very constant. At 300 K, when the amount of carriers in Γ is smaller anyway, a slight filling effect can be observed between 10 % and 50 % DC resulting in a peak shift of 20 meV. The choice of a duty cycle of 30 % is therefore a stable point for measurements and no heating is caused by long pulse durations.

Thus, the behavior of the GeSn/SiGeSn MQW was well understood and the main goal, a proof of carrier confinement in LEDs, was found. This forms a solid base for further studies of optically pumped lasers in the next step and electrically pumped direct bandgap devices in the future.

4.4. Summary

In this chapter various LED structures were discussed. In a first step, the fabrication process as well as some electrical characteristics were introduced, followed by the characterization of indirect and direct bandgap homojunctions. In the second part, two different MQW LED designs, one with Ge and the other with SiGeSn as barrier material, were tested.

The key results are listed below.

- The fabrication was done by standard CMOS process steps, adapted for GeSn with process temperatures only up to 300 °C to maintain the material quality.
- Negative differential resistance, a typical feature for tunnel diodes, was obtained for just-direct bandgap material at low temperature. This observation clarifies the transport mechanisms inside the investigated devices.
- Homojunction LEDs with Sn contents of 8.5 at.%, 11 at.% and 13 at.% Sn offer tunable emission, i.e. lower energy emission for higher Sn concentrations.

- The directness of the samples influences the relative increase of integrated intensity at low temperatures. In case of moderate directness, the intensity increases with increasing directness, since a larger amount of carriers resides in Γ . Defects can strongly deteriorate the emission efficiency by decreasing the non-radiative recombination time, as seen for an LED with 13.0 at.% Sn.
- The investigation of the GeSn/Ge MQW LED shows that Ge is not a suitable barrier material for confining electrons in the active GeSn wells.
- In contrast, a SiGeSn barrier offers a strong carrier confinement which is enhanced at low temperature for the here presented, slightly indirect bandgap active wells. Therefore, carriers are screened from defects at the Ge interface and the radiative recombination efficiency is enhanced.
- Heating dependent on DC could be excluded, confirming the measurement procedure as appropriate.

After the investigation of spontaneous radiative recombination in blanket material as well as light emitting devices, the next chapter deals with the study of stimulated radiative recombination in GeSn cavities with several material combinations.

5. Optically Pumped Lasers

Contents

5.1. L	aser Theory	63
5.2. F	abrication and Measurement Routine	68
5.3. G	eSn Single Layer Lasers	69
5.3	1. Strain Distribution in Suspended Disk Structures	71
5.3	2. Lasing Characteristics	73
5.4. G	eSn:P for Lasers	7 9
5.4	1. Material Overview	80
5.4	2. Lasing Characteristics	83
5.5. G	eSn/SiGeSn Heterostructure Lasers	85
5.5	1. Strain and Band Structure in Undercut MQW Microdisks	86
5.5	2. Lasing Characteristics	89
5.6. S	ımmary	96

The interest in an infrared laser that can be integrated on electronic chips, grows rapidly and covers the field of III-V lasers bonded^{131–133} or directly grown on Si,^{37,134–137} as well as those consisting of group IV materials.⁵⁸ While the laser development of direct bandgap III-V materials already reached several milestones, the study of group IV lasers is still in an infancy state. Regarding the latter, many approaches like highly doped or strained Ge are under investigation.^{138–145} Although tensily strained Ge can be turned into a direct bandgap semiconductor, only a few

groups claim the observation of lasing in Ge until now. 44,146 While stimulated emission in Si via erbium (Er) doping required tremendously high quality (Q)-factor cavities and electrical injection is still a challenge, 147-151 the light generation from Si nanocrystals was strongly restricted to spontaneous emission until the first optical lasing was shown in $2018.^{152-155}$ A further Si-only laser solution is based on stimulated Raman scattering. 156-159 To operate such laser, an optically pumping source is obligatory, making this application inapplicable for large scale wafer integration. Thus, a very promising approach of a group IV-only light source is formed by alloving Ge with Sn. In 2015, the dream of a laser, solely consisting out of group IV elements became reality. 46 For the first time, lasing was demonstrated in optically pumped Fabry-Pérot (FP) cavities made from $Ge_{0.875}Sn_{0.125}$. The performance was limited to a threshold value of 325 kW cm⁻² and a maximum lasing temperature of 90 K, but improvements should follow fast. Next to FP cavities, microdisk and photonic crystal geometries have been used and the maximum lasing temperature was increased to 180 K^{3,49,50,54,160,161} by increasing the Sn concentration and therefore the directness. Furthermore, the threshold was slightly decreased, but stayed in the same order of magnitude, until the application of heterostructures leveraged the threshold reduction.^{6,11}

The following chapter deals with the development of optically pumped GeSn microdisk (MD) lasers. Starting with a short theoretical recapitulation on the physics of stimulated emission, the introduction of single layer GeSn MDs follows. In this regard, their fabrication as well as their geometrical properties like local strain distribution and lasing performance are discussed. The second part of this chapter addresses the option of n-type doping using phosphorus, similar to the approach used for Ge. Its aim is to improve the lasing performance of materials with only moderate directness by increasing their intrinsic carrier concentration. The last part deals with GeSn/SiGeSn heterostructure microdisk lasers, their opportunities and limitations.

All mode analyses and strain simulations in this chapter result from collaboration with the group of *Prof. Jeremy Witzens* from *IPH*, *RWTH Aachen University* and were conducted by *Bahareh Marzban*.

All lasing spectra presented here were obtained in cooperation with the group of Dr. Hans Sigg from the Paul Scherrer Institut (PSI). I travelled there to use their

micro-PL set-up and measurements were performed together with different group members, namely *Richard Geiger*, *Esteban Marin*, *Thomas Zabel* and *Francesco Armand-Pilon*, as well as the first measurement series was accompanied by my former colleague *Stephan Wirths*. *Raman* spectroscopy was conducted at *ETH Zürich* and the measurements have been performed together with *Thomas Zabel*. The results in the upcoming chapter have been previously published in references [3, 4, 6, 11, 162, 163].

5.1. Laser Theory

The physics of lasers (light amplification by stimulated emission of radiation) is based, as the name already indicates, on stimulated emission processes, which were firstly postulated by Einstein in 1917.¹⁶⁴ In the following, stimulated emission in semiconductors is discussed. In contrast to spontaneous emission, which occurs randomly in time, stimulated emission may contain spatially and temporally coherent components. In an atom, an incident photon stimulates the transition of an excited electron to its ground state. The analogue process in solid crystals involves transitions from conduction to valence bands. An incident photon therefore stimulates the recombination of an electron-hole pair, which accordingly emits a photon. The thus generated photon is in phase with the stimulating one. The transition rate for stimulated emission depends on the occupation probability of electrons f_c in the conduction band and hole states in the valence band $1 - f_v$, as well as their densities of states ρ_c and ρ_v , respectively:¹¹⁶

$$R_{st} = B_{21} \int f_c(1 - f_v) \rho_c \rho_v \rho_{ph} dE.$$
 (5.1)

The photon density is given by ρ_{ph} , while the transition probability from state 2 to state 1 is determined by the Einstein coefficient B_{21} . To achieve a positive stimulated emission rate from equation 5.1, population inversion is necessary, which can be expressed by $pn > n_i^2$, with n_i being the intrinsic carrier concentration. With the pre-requirement of photon energy $h\nu$, with photon frequency ν and Planck constant

h, to be larger than the semiconductor bandgap (so that absorption is possible), lasing is reached when the quasi Fermi levels are degenerate and lie inside the conduction- and valence band:¹⁶⁵

$$E_q < h\nu < E_{Fn} - E_{Fp}. \tag{5.2}$$

Here, E_{Fn} and E_{Fp} represent the quasi Fermi levels for electrons and holes. Photons, stimulated by other photons with the same wavelength, can on their part stimulate further transitions which makes the process self-amplifying, as long as the condition in equation 5.2 is fulfilled.¹⁶⁶

The gain (negative absorption), $g = (-1)\alpha(E)$ of the direct transition at the Γ point can be written as:⁸⁰

$$\alpha(E) = \frac{q^2 h |M_b|^2}{4\pi^2 \epsilon_0 m_0^2 c n_m E} \left(\frac{2m_r}{\hbar^2}\right)^{3/2} (E - E_g)^{1/2} [1 - f_c(E_c) - f_v(E_v)]$$
 (5.3)

Here, ϵ_0 is taken as vacuum permittivity, n_m as mode index, m_0 as free-electron mass and m_r as reduced effective mass $\frac{m_c m_{bh}}{m_c + m_{hh}}$ for heavy hole transitions. M_b expresses an average matrix element of the Bloch wave functions. The equation results from the integration over all states described by the conduction and valence band density of states and their occupation. Additionally, the transition matrix element has to be included. For the complete gain, transitions into light and heavy hole band have to be summed up.

In a QW system with 2D DOS, the equation changes to:

$$\alpha^{2D}(E) = \frac{q^2 m_r |M_b|^2}{\epsilon_0 m_0^2 c \hbar n_m E L_z} [1 - f_c(E_c) - f_v(E_v)], \tag{5.4}$$

which is in contrast to the latter coefficient inversely dependent on the QW width L_z .

To build lasers, an optical cavity is necessary including the gain material. The simplest example is the FP laser, which consists of a waveguide with typically two mirroring facets. Such cavities offer feedback and thus increased amplification since they allow photons to repeatedly pass through the gain medium.

A general way to experimentally proof if lasing is observed, was concluded by Samuel

et al.[167]. The main indicators for lasing are a directional beam and a threshold in line width when turning from spontaneous to stimulated and amplified emission and, accordingly a narrow line width of the laser emission. Furthermore, a threshold in output power should be observed for the onset of stimulated emission. When the maximum gain is reached the intensity saturates, so that the typical s-shaped curve (light output dependent on input power) is generated. Next to that, temporal coherence and the polarization of laser light, which is specific for the transition and geometry, are typical characteristics of laser emission. However, these are difficult to measure and therefore, in this chapter the previously mentioned characteristics are emphasized.

For indirect GeSn semiconductors, pumping has to be very high, until population inversion can be reached, since first the states in L will be filled, till the excitation of Γ electrons takes place. Evidentially, gain calculations predict a higher gain for increased directness, which can be reached by rising the Sn content. Based on that, also the threshold should be reduced for higher Sn content lasers, at least from theory, while calculations implicating neither defects nor the accompanying losses. Values from experimental literature tell another story, though: In two different studies, a lower threshold value was found for the lower Sn content, direct bandgap material. However, it is not always straight forward to compare threshold values, since optical losses have a strong impact on the threshold. It was shown that the reduction of threshold can be fostered by confining the mode to create an enhanced optical mode overlap with gain material.

Beside simulations of the gain for bulk material, calculations for GeSn/SiGeSn quantum wells can be found in literature. While the gain is reduced in those calculations, the MQWs benefit from the 2D density of states. The smaller number of states reduces the required pumping power to achieve population inversion and therefore the threshold. 169,170

In this work, laser cavities consist of undercut microdisks, which in the following shall be shortly introduced.

Microcavities are used to confine light to small volumes. This enables to meet demands for integration into an OEIC, i.e. a small gain medium and low power consumption. Using a high ratio of refractive index between the active medium (GeSn with n(2.5 µm)= 4.2)¹⁷¹ and the surrounding (in our case air n=1) helps to obtain a further requirement, the confinement of the optical field to the cavity. For the chip integration, SiO₂ (n=1.5)¹⁷² or silicon nitride (SiN) ($n\sim1.9$)¹⁷³ are suitable materials for encapsulation.

In the disk, light may travel in form of whispering gallery modes (WGM) along the circumference. Due to total reflection for incident angles $> \arcsin(1/n_{\rm eff})$ at the disk's surface, the light is strongly confined to the disk volume and no metallic mirrors are necessary compared to FP cavities. $n_{\rm eff}$ refers to the effective refractive index of the disk. After one round trip in the circular cavity, the wave matches the resonance condition and by constructive interference of the two counter propagating waves, standing waves are formed along the radius.

WGM are complex solutions of the Maxwell's equations in a cylindrically symmetric system. They can be characterized by two mode numbers, one for the azimuthal (M), one for the radial (N) part of the solution. M appears in the phase factor $\exp(iM\Phi)$ describing a mode degeneracy for M and -M, resulting in 2M numbers of modes along the circumference. The radial number N defines the number of nodes along the radius via N-1.¹⁷⁴

In a perfect MD cavity, light is almost fully confined. Since in reality there are many possible sources for losses, a quality factor Q is defined, describing the deviations from the ideal case.¹⁷⁵ MD cavities are known for their possible extremely high Q factors.^{176,177} A common expression for the internal Q_{int} , where modes are not coupled to waveguides etc. is:

$$Q_{int} = \omega_0 \frac{\text{stored energy}}{\text{intrinsic power loss}},$$
 (5.5)

with angular frequency ω_0 . It is often expressed as $Q = \omega_0/\Delta\omega$, with emission frequency ω_0 and line width $\Delta\omega$.¹⁷⁵ Internal power losses maybe due to:¹⁷⁵

- (i) the material absorption in the cavity, other than the interband absorption, but for example free carrier and intervalence band absorption; or absorption from the cavities' coating,
- (ii) scattering losses due to side wall roughness and imperfections of the geometry

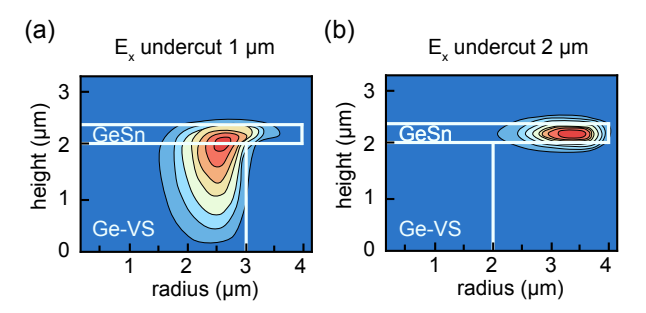


Figure 5.1. Mode simulation of TE_0 WGM mode with (a) $1\,\mu m$ and (b) $2\,\mu m$ undercut of a $Ge_{0.875}Sn_{0.125}$ disk with a Ge pillar by courtesy of *B. Marzban*. The white lines represent half of the microdisk geometry, while the intensity of the mode is shown in a false colour plot.

and

(iii) bending losses (also called tunneling losses) originating from the fact that not all the light is totally reflected at the surface and a portion of light is transmitted to the low refractive index medium.

Bending losses are inversely dependent on the refractive index contrast.¹⁷⁸ The modes are able to tunnel through the potential at the disk edge, while they are evanescent and decay exponentially in the tunnel region with radius $R_{tunnel} \sim n_{\text{eff}} \cdot R_{\text{disk}}$, they freely onward for distances $> R_{\text{tunnel}}$.

In our case of a GeSn disk with a Ge pillar, additional losses are caused by coupling of WGM into the high index pillar region. To avoid this, the disk undercut of the GeSn disk has to be large enough. An example is shown for the transversal electrical mode (TE_0) in figure 5.1 for two different undercuts, courtesy of *B. Marzban*. This is an essential difference to non-undercut FP modes, where a large fraction of the mode is located in the Ge-VS.⁶⁵

5.2. Fabrication and Measurement Routine

Fabrication of GeSn microdisk cavities follows the same process in all discussed samples throughout the thesis and was first described by S. Gupta et al., ¹⁷⁹ Meanwhile more groups are using this process for fabrication. 180,181 Circular mesas with different diameter sizes between 7 µm and 140 µm were defined by optical lithography in HSQ XR5114 resist. After the development in MFCD26, steep mesas were dry-etched in a Cl₂/Ar plasma, as sketched in figure 5.2a, depicting the main steps of the process flow. In the following step, Ge is selectively etched in a barrel reactor with an isotropic CF₄ plasma. The selectivity of Ge over Ge_{0.875}Sn_{0.125} was found to be $\sim 270.^{115}$ In this manner Ge is dry-etched until only small pillars are left on top of the Si wafer. Afterwards, the resist was removed by a hydroflouric acid (1%) wet etch. The surface was passivated in an ALD reactor by 10 nm Al₂O₃ for the single layer devices and with 10 nm HfO₂ for the heterostructure devices below. In figure 5.2b an SEM of a fabricated device from a GeSn/SiGeSn DHS is shown. An X-TEM of one of the $Ge_{0.875}Sn_{0.125}$ single layer MDs in figure 5.2c emphasizes the undercut of the disk. It is visible that threading dislocations, which are formed at the interface to Ge-VS from strain relaxation, still remain at the bottom part of the disk and are not removed by CF_4 etch.

All laser measurements were performed in a μ -PL set-up, in which the sample can be cooled to 20 K in a cold-finger cryostat. For pumping either a pulsed Nd:YAG (1064 nm) or a pulsed telecom laser (1550 nm) was used. The pulse length and repetition rate amount to 5 ns and 17 kHz, and 800 ps and 20 kHz, respectively. These can be translated to duty cycles (DC) of 8.5×10^{-5} for the 1064 nm and 1.6×10^{-5} for the 1500 nm laser. In Ge_{0.875}Sn_{0.125} the absorption of light at 1550 nm is approximated to be 30 % lower compared to absorption at 1064 nm.^{6,87} The laser light was guided to a 15× Schwarzschild objective and focused to a sub-10 µm diameter spot size, which is later used to calculate the excitation power density. The spot size was determined by scanning through the sample position with a razor blade in 1 µm steps and measuring simultaneously the evolution of the intensity. This procedure was executed in horizontal as well as in vertical direction. An example of the measured data of the 1064 nm laser spot is shown in figure 5.3a. By taking the first derivative,

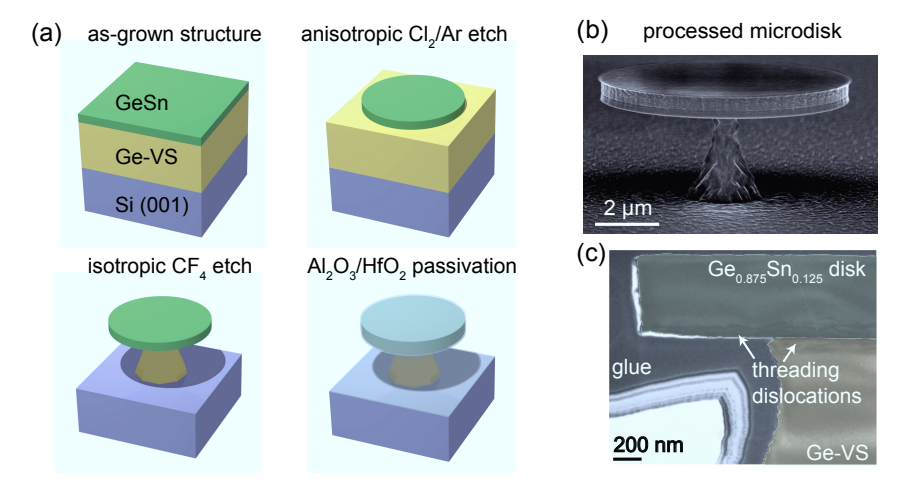


Figure 5.2. (a) Schematically drawn process flow for MD cavities. An SEM of an 8 µm GeSn/SiGeSn DHS MD is shown in (b). (c) An X-TEM of a single layer MD reveals remaining threading dislocations in the disk layer. Reprinted and adapted with permission from [6, 182]. Copyright 2018 American Chemical Society.

the gaussian spot shape can be evaluated and in this case spot diameters of $7.7\,\mu m$ in horizontal and $6.8\,\mu m$ in vertical direction are determined. For convenience, a circular spot size is assumed with a mean of $7.3\,\mu m$ as the diameter.

After excitation, the emitted light is guided to an FTIR interferometer via the same objective, where it is detected by a liquid nitrogen cooled InSb detector. All pumping power densities mentioned in the following, refer to peak power densities, meaning the power density, which is applied to the MDs during one pulse.

5.3. GeSn Single Layer Lasers

First of all, single layer GeSn MD lasers are studied. The disks are fabricated from two different layer stacks grown on top of Ge-VS: One $560 \,\mathrm{nm}$ thick $\mathrm{Ge_{0.875}Sn_{0.125}}$ layer as well as a $770 \,\mathrm{nm}$ thick $\mathrm{Ge_{0.915}Sn_{0.085}}$ layer, which are referred respectively as sample A and B in the following. While sample A exceeds a residual strain

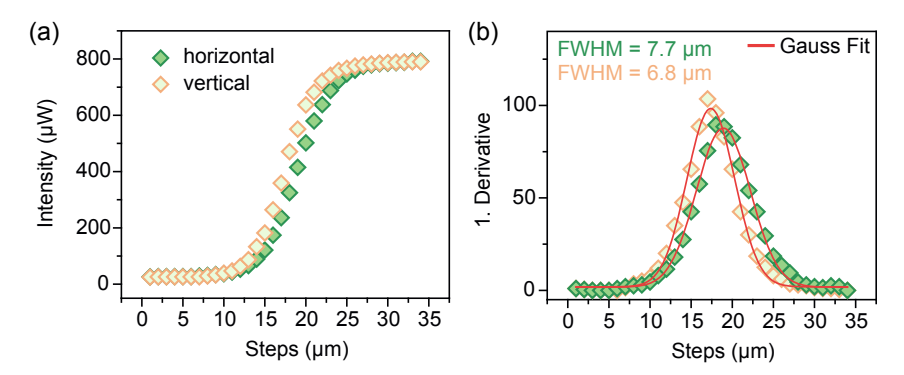


Figure 5.3. Spot size determination of the 1064 nm excitation laser. (a) Measured power while moving a razor blade through the spot. (b) First derivative of the data, to extract a spot diameter from the FWHM of the gauss peak. Adapted with permission from [102]. Copyright 2018 American Chemical Society.

of $-0.40\,\%$, sample B sample has a value of $-0.15\,\%$, which places it just at the transition from an indirect to a direct bandgap semiconductor. An overview on the unprocessed material parameter is given in table 5.1. From sample A, it is already known that it works as a laser in FP geometry. Here, the advantages and disadvantages of an undercut MD cavity shall be explored. Additionally, it is very interesting to study a material with very low directness of 3 meV (at 4 K) in the unprocessed layer, as sample B, to see whether lasing can be observed at all. In the following section, the strain distribution of the undercut MD geometry is analyzed via *Raman* spectroscopy and the band structure is considered, before the lasing results are presented.

Name	Sn (at.%)	thickness (nm)	strain $(\%)$
A	12.5	560	-0.40
В	8.5	770	-0.15

Table 5.1. Overview on unprocessed sample parameter of MD laser material.

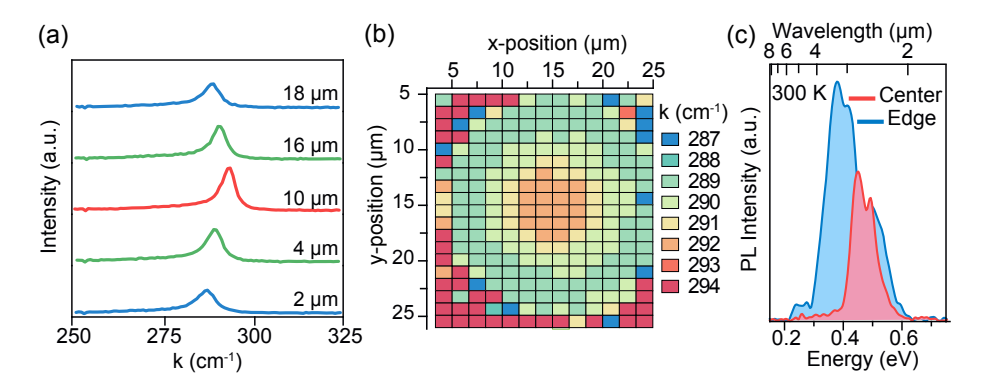


Figure 5.4. Influence of strain in the undercut MDs. (a) Line scans correspond to different μ m-steps along the vertical direction of a 20 µm diameter Ge_{0.875}Sn_{0.125} disk. (b) Raman mapping of the same disk matches the shift measured in (a). (c) The bandgap narrowing of the undercut and relaxed region of the disk, can be seen in PL measurements of a 140 µm diameter disk with a 532 nm laser. Adapted with permission from reference [4].

5.3.1. Strain Distribution in Suspended Disk Structures

In an undercut disk structure it is expected that residual strain in the layer is released for the under-etched parts. To get experimental verification, Raman measurements were performed. In these kind of measurements, the Raman-scattered light, which changes its energy because of the Raman process going along with the emission of lattice vibrations (phonons), sheds light on the atom species and their bonding. In the case of GeSn in this work, the photon interaction with the Ge-Ge phonon mode is analyzed. It does not seem to be clear distinguishable if transversal (TO) or longitudinal optical (LO) or both phonons are involved, since their energies are degenerated in a cubic crystal and only very slightly split due to strain. In Raman shift depends on the Ge bond length and the mass of involved atoms, which is both influenced by Sn content and strain. Some studies in literature discuss, how to calculate the interplay between Sn content and strain from a Raman shift. Some shift. Some studies in literature discuss, how to calculate the interplay between Sn content and strain from a Raman shift. Micro-Raman measurements of MDs were performed in a WiTec set-up using a continuous wave 532 nm excitation laser with $\sim 500 \, \mathrm{nm}$ spot size. In a power

dependent measurement, the Raman shift due to heating of the structures was evaluated and used as correction for the measured data. 190 The laser power was chosen so that the influence of the heating was below a peak shift of $0.3 \,\mathrm{cm}^{-1}$. Typically, Ge-Ge vibrations in bulk Ge layers are observed at $\sim 300\,\mathrm{cm}^{-1}.^{191-193}$ Measurement results of a 20 µm diameter Ge_{0.875}Sn_{0.125} disk with 3.5 µm undercut are presented in figure 5.4a and b. Raman shifts at different positions along the disk are visible in the spectra in figure 5.4a. For figure 5.4b the peak positions were evaluated by a Lorentzian fitting procedure and are plotted in 1 µm steps. The Raman shift in the center of the disk is at 292.5 cm⁻¹ and changes at the undercut part to 289.5 cm⁻¹. Since the composition is constant along the disk, this shift is exclusively caused by strain relaxation. The evaluation of the precise strain over the disk structure is complicated, since the strain is not biaxial anymore. Due to the geometry and the radial relaxation, in-plane strain components $\epsilon_{xx} = \epsilon_{yy}$ change with the azimuthal angle, while their sum changes with the radius. Most known models, which are used to correlate a Raman shift to strain in GeSn, refer to biaxially strained layers. Therefore, the strain is modelled later. Additional confirmation of the strain relaxation at the rim of the disk is given by PL measurements in figure 5.4c, which were performed with a 532 nm laser at a 140 µm diameter disk center and edge. Due to strain relaxation the conduction band shifts downwards and the bandgap is reduced. Caused by the large excitation laser spot of 10 µm, the spectra superpose each other partly. Nevertheless, the edge spectrum is 23 meV red shifted. Band structure calculations for the same alloy with -0.4% and 0.0% biaxial strain gives a change in bandgap of 19 meV, which is in good agreement with the observed shift.

To model the strain distribution in the disk, a strain simulation was executed with COMSOL multiphysics by B. Marzban. In figure 5.5a, the $\epsilon_{xx} + \epsilon_{yy}$ strain field is shown in a false color plot. The Ge-VS pillar of 13 µm diameter is large enough to anchor the GeSn layer in that region and the layer's as-grown strain is maintained. Details of the simulation (not shown here) reveal a still remaining strain in azimuthal direction of the disk's rim, while in radial direction the strain becomes slightly tensile. If the pillar region is reduced, like in 8 µm diameter disks with the same undercut, the pillar region is one order of magnitude less compressively strained and also deforms by the full relaxation of the disk.

Using the calculated strain values of the 20 µm disk, the band structure is derived

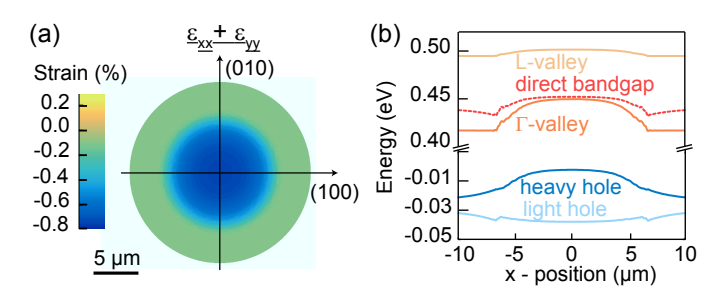


Figure 5.5. Strain simulation of an undercut microdisk with 20 µm diameter and 3.5 µm undercut is shown in (a) in $\epsilon_{xx} + \epsilon_{yy}$ direction. Courtesy of *B. Marzban*. The corresponding band structure is depicted in (b) for 295 K. Courtesy of *Dr. Z. Ikonić*. Adapted with permission from [3]. Copyright 2018 American Chemical Society.

in figure 5.5b for 295 K thanks to Dr.~Z.~Ikonić. Since the strain is not biaxial at the rim of the disk, the naming of heavy and light hole bands is only valid in the pillar region. Between pillar and rim region, the conduction band is shifted down by strain relaxation causing an increase of the directness by 26 meV and, therefore, a higher electron population at $\Gamma.$ Additionally, the bandgap is decreased leading to an energy gradient through the disk diameter, so more electrons recombine at the rim region, enhancing the intensity of WGMs.³ However, for a smaller disk of 8 μ m diameter with the same undercut of 3.5 μ m, this potential gradient is strongly reduced due to the relaxation of the pillar region. In return the improvement of the directness to 84 meV due to a stronger relaxation, is even higher for such small pillar disks.

With these lattice and band structural analysis as a background, lasing performance of different MDs is discussed in the next section.

5.3.2. Lasing Characteristics

The $8\,\mu\mathrm{m}$ diameter disks are measured with the previously described set-up and the $1064\,\mathrm{nm}$ laser as excitation source.

Results for a disk from sample A (12.5 at.%) are presented in figure 5.6. Power dependent measurements with peak powers from $114\,\mathrm{kW\,cm^{-2}}$ to $816\,\mathrm{kW\,cm^{-2}}$ at $50\,\mathrm{K}$

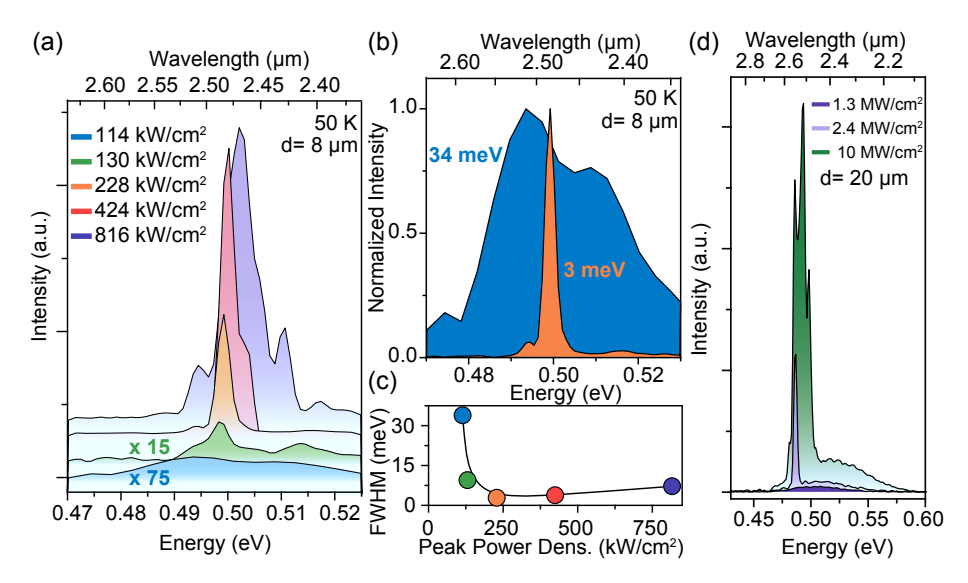


Figure 5.6. Sample A. (a) Lasing spectra of Ge_{0.875}Sn_{0.125} 8 μm MDs at 50 K at different pumping power. (b) Line width narrowing from spontaneous to stimulated emission, adapted with permission from [4]. (c) Line width trend with pumping power. (d) Lasing spectra of a 20 μm diameter disk.

in figure 5.6a show the evolution from spontaneous emission to stimulated emission around $0.50\,\mathrm{eV}$ when increasing the pumping power. Above $228\,\mathrm{kW\,cm^{-2}}$, the spectra reveal multi mode lasing. Normalized spectra below and above threshold in figure 5.6b exhibit the typical line width collapse from $34\,\mathrm{meV}$ to $3\,\mathrm{meV}$ when stimulated emission sets in. The progression of line width with pumping power is additionally depicted in figure 5.6c.

Measurements of a $20\,\mu m$ diameter $Ge_{0.875}Sn_{0.125}$ (sample A) MD are plotted in figure 5.6d. There, much higher pumping powers are needed to observe laser emission around $0.49\,eV$. Furthermore, a large background around $0.52\,eV$ becomes visible especially for increasing pumping power. This spontaneous background emission is attributed to the disk region with pillar underneath, which amounts to $13\,\mu m$ in diameter for a $3.5\,\mu m$ undercut. In this center part, the GeSn lattice is less relaxed and therefore exhibits a larger bandgap, refer to section 5.3.1. Dependent on the carrier lifetime, carriers at the center are able to drift and diffuse to the

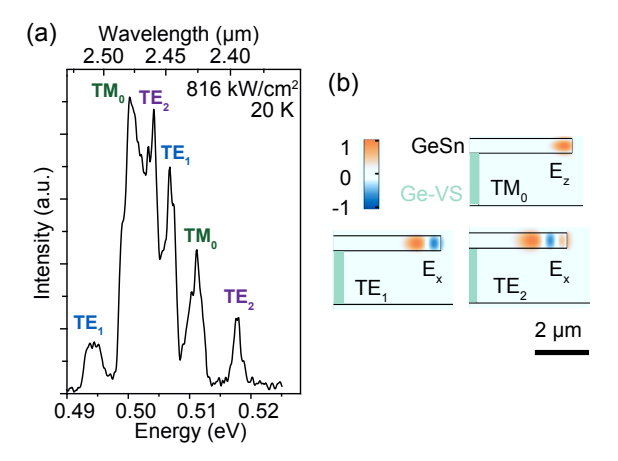


Figure 5.7. Sample A. (a) High resolution $(2 \, \mathrm{cm}^{-1})$ spectrum at 20 K of an 8 µm MD at 816 kW cm⁻² revealing different WGMs. (b) E_x of TE_1 , TE_2 and E_z of the TM_0 is schematically shown by courtesy of *B. Marzban*. Adapted with permission from [3]. Copyright 2018 American Chemical Society.

lower bandgap region at the disk edge. However, lifetimes above 1 ns are necessary to accumulate 8% of the carriers from the center to the edge part of the disk. 182 Carrier lifetime measurements of $\rm Ge_{0.875}Sn_{0.125}$ unprocessed layers via pump probe spectroscopy provide numbers between 170 ps and 260 ps at temperatures from 25 K to 300 K. 54 Since in this set-up most of the excited carriers are generated in the undesired region by using such large MDs, in the following, exclusively disks with 8 μ m diameter are used for characterization.

From the spectrum measured at $20 \,\mathrm{K}$ with a resolution of $2 \,\mathrm{cm}^{-1}$ in figure 5.7a different WGM can be identified. Therefore, the free spectral range (FSR), which describes the energy/frequency spacing between two resonance peaks of a mode, is evaluated from peak energies in figure 5.7a, the latter are summarized in table 5.2. The extracted FSR is compared to theoretically calculated modes and attributed to those listed in table 5.3. The calculation of WGMs was performed with the software $Synopsis \,RSoft$ by $B. \,Marzban$. Modes oriented along the radial direction (transversal electrical (TE)) and those along z-direction (transversal magnetic (TM)) were included in the calculation. As can be seen by the comparison, TE₁, TE₂ and TM₀ can be attributed to the observed peaks, sketched in figure 5.7b, serving as a con-

$\mathbf{E}_a \; (\mathbf{meV})$	$\mathbf{E}_b \; (\mathbf{meV})$	$\mathbf{E}_c \; (\mathbf{meV})$	$\mathbf{E}_d \; (\mathbf{meV})$	$\mathbf{E}_e \; (\mathbf{meV})$	$\mathbf{E}_f \; (\mathbf{meV})$
494.4	500.3	504.2	506.7	511.1	517.8

Table 5.2. Peak positions of the high resolution spectrum from MD-A ordered from low to high energies.

mode	$egin{array}{l} \mathbf{n}_g \ \mathbf{at} \ 2.4 \mathbf{\mu m} \end{array}$	FSR at 2.4 µm (meV)	$egin{array}{l} { m n}_g \ { m at} \ { m 2.5 \mu m} \end{array}$	FSR at $2.5\mu m$ (meV)	measured FSR (meV)
TE_1	3.9681	12.4	3.9611	12.5	12.3
TE_2	3.5127	14.0	3.8088	13.0	13.6
TM_0	4.5883	10.8	4.6404	10.6	10.8

Table 5.3. Calculated FSR and group indices at $2.4\,\mu\mathrm{m}$ and $2.5\,\mu\mathrm{m}$ compared to measured FSR of an $8\,\mu\mathrm{m}$ diameter $\mathrm{Ge}_{0.875}\mathrm{Sn}_{0.125}$ disk (MD-A). Courtesy of B. Marzban. Reprinted with permission from [182]. Copyright 2018 American Chemical Society.

firmation of WGM lasing.

From the high resolution spectrum, quality factors up to 305 are extracted by dividing the line width by the emission energy.

Temperature dependent lasing spectra at pump powers of $\sim 820\,\mathrm{kW\,cm^{-2}}$ are presented in figure 5.8a for disk laser A ($12.5\,\mathrm{at.\%}$ Sn) and B ($8.5\,\mathrm{at.\%}$ Sn). Due to the lower Sn content and therefore larger bandgap of MD-B, the emission energy at 0.61 eV is blue shifted compared to MD-A. While MD-A reveals lasing until $130\,\mathrm{K}$, lasing is observed up to $90\,\mathrm{K}$ for MD-B. This difference can be attributed to the amount of directness of both structures. Whereas for an unstrained lattice with $12.5\,\mathrm{at.\%}$ Sn a directness of $84\,\mathrm{meV}$ is calculated, a fully relaxed lattice with $8.5\,\mathrm{at.\%}$ has a value of $14\,\mathrm{meV}$ at $20\,\mathrm{K}$. Therefore, the electron distribution in MD-B leads to less efficient radiative recombination, especially for higher temperatures, when the fraction of electrons in Γ decreases and, in return, rises at L.

This affects also the light-in light-out (LL) curves at the investigated temperatures, shown in figure 5.8b and c for both lasers, MD-A and MD-B, respectively. The higher the temperature, the earlier occurs an intensity roll-over for MD-B, which is not observed for MD-A, where only an intensity saturation is visible. Such roll-over

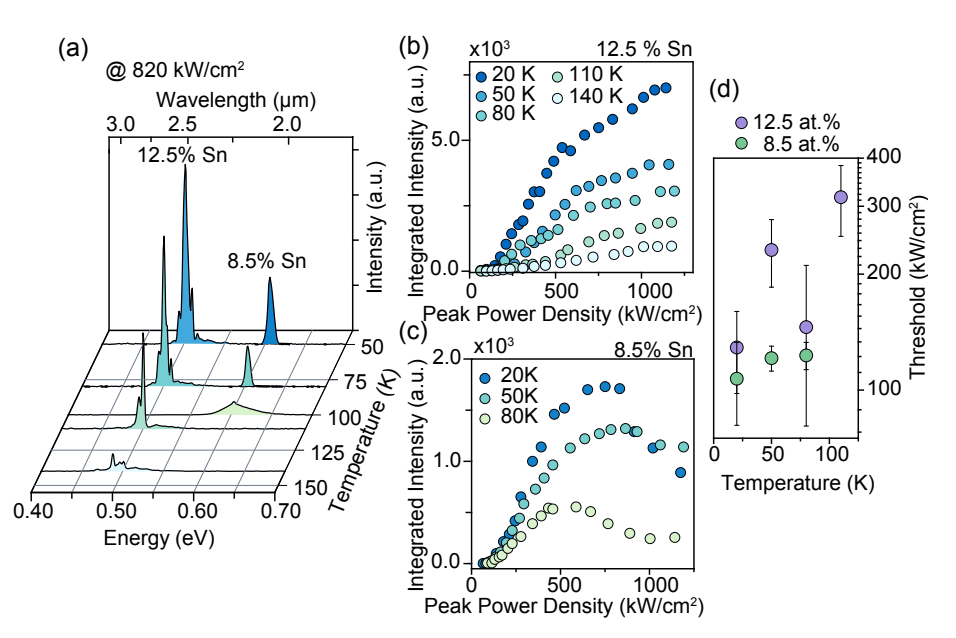


Figure 5.8. Lasing spectra of $8\,\mu\mathrm{m}$ MDs at $\sim\!820\,\mathrm{kW\,cm^{-2}}$ for MD-A and B at different temperature in (a). (b) and (c) show light-in light-out curves at similar temperatures as in (a) for sample A and B, respectively. (d) Temperature dependent thresholds are plotted for both MD types. Adapted with permission from [3]. Copyright 2018 American Chemical Society.

behavior is also known from III-V input-current versus output-power experiments, especially in vertical cavities, were thermal heating is a major challenge. 194,195 From the LL curves the threshold values of the two devices are extracted. Surprisingly, the threshold is smaller for MD-B $((130\pm31)\,\mathrm{kW\,cm^{-2}}$ versus $(107\pm26)\,\mathrm{kW\,cm^{-2}}$ at 20 K, for A and B respectively), in spite of the lower maximal lasing temperature. The error of the threshold is derived from the uncertainty of the fit, which was applied to the LL-curves. An overview of threshold values is given in figure 5.8d. The uncertainty arises from the different linear fits which are possible. The lower threshold power densities for sample MD-B are attributed to the higher material quality, i.e. less misfit dislocations as well as a lower number of point defects/vacancies (from growth at higher temperature). This is in agreement with findings from another group, where also lower thresholds for lower Sn content sam-

ples were obtained,⁵⁰ indicating confirmation of the previous explanation. There, a higher material quality, and thus a lower threshold, was achieved by a graded buffer technology. A further reason might be the higher mode confinement in the thicker 8.5 at.% sample B. Due to the larger volume of the active layer, losses from surface roughness might be reduced.

The increasing threshold at higher temperature and ceasing of lasing in the structures is affected by many processes. The carrier occupation at higher temperatures becomes relatively smaller in Γ and carriers accumulate in L which has a higher density of states. Moreover, SRH and Auger recombinations increase for higher temperatures. Since the required excitation density is high, it facilitates Auger recombination which rises with the cube of carrier concentration. Simulations show that Auger recombination is probably one of the limiting processes in GeSn lasers. It can be suppressed by using 2D designs, like GeSn/SiGeSn MQWs. 82

However, in comparison to the $\rm Ge_{0.875}Sn_{0.125}$ FP laser, ⁴⁶ some improvements are achieved. The lasing temperature was increased from 90 K to 130 K and the threshold was reduced at 20 K from 325 kW cm⁻² to $(130\pm31)\,\rm kW\,cm^{-2}$. These advancements are attributed to

- (i) a modified band structure with a larger directness due to strain relaxation,
- (ii) a better mode confinement in the undercut disks due to a larger refractive index contrast between GeSn and air and
- (iii) reduced surface recombination due to surface passivation of the MDs, not present in the FP cavity.

In the following, two modifications of the GeSn gain material are explored, (1) doping of GeSn and (2) the application of GeSn/SiGeSn heterostructures.

5.4. GeSn:P for Lasers

Several theoretical studies are available in literature, promising enhanced gain and reduced thresholds for indirect bandgap n-doped GeSn or Ge. 65,70,138,168,196 In those indirect bandgap semiconductors, any increase of carriers at Γ yields an improvement of lasing characteristics. For alloys with increasing Sn content the situation becomes more complex. In one study, it is shown that a threshold reduction by doping can be only achieved up to a concentration of $1 \times 10^{19} \,\mathrm{cm}^{-3}$ for fully relaxed, direct bandgap GeSn. Above that, the threshold increases, which is undesirable. 196 This is due to the interplay between the alloy's DOS and the occupation at Γ . For increasing Sn concentrations with constant strain, the effective mass and therefore the DOS decreases. This would lead to a decreasing gain and increasing threshold. But simultaneously, the electron occupation increases for higher Sn concentrations, since the directness rises, which leads to a higher gain and lower thresholds. For lower Sn contents the latter has the major impact, so that the threshold decreases with doping and Sn content. At a certain Sn concentration and doping (which differs depending on the strain), the majority of carriers resides in the Γ -valley, so that the degradation of threshold and gain due to decreased DOS, dominates. A decreasing optimum doping concentration for increasing Sn content is also found by B. Dutt et al., 168 which lies for 10 at.% at 3×10^{18} cm⁻³.

Calculations of material gain in figure 5.9a show the impact of doping concentration on in-plane gain for a direct bandgap $Ge_{0.875}Sn_{0.125}$ layer with -0.4% compressive strain at 300 K, which have been executed by D. Rainko. In these calculations free carrier absorption (FCA) is included with different contributions, explained in detail in reference [197]. At low doping concentrations of $2 \times 10^{18} \, \mathrm{cm}^{-3}$ and carrier injections of $5 \times 10^{17} \, \mathrm{cm}^{-3}$ and $1 \times 10^{18} \, \mathrm{cm}^{-3}$, the lasing condition in equation 5.2 is not fulfilled. Therefore, more injected carriers lead to higher FCA (red and green points). Above a doping concentration of $\sim 2 \times 10^{19} \, \mathrm{cm}^{-3}$ and for carrier injection of $1 \times 10^{18} \, \mathrm{cm}^{-3}$ quasi Fermi levels are shifted, so that equation 5.2 is fulfilled. Still the losses prevail, but now for higher injection the gain increases (green line). For injection of $5 \times 10^{18} \, \mathrm{cm}^{-3}$ the gain continuously increases over the whole doping range shown here (blue line). Material gain spectra are exemplarily

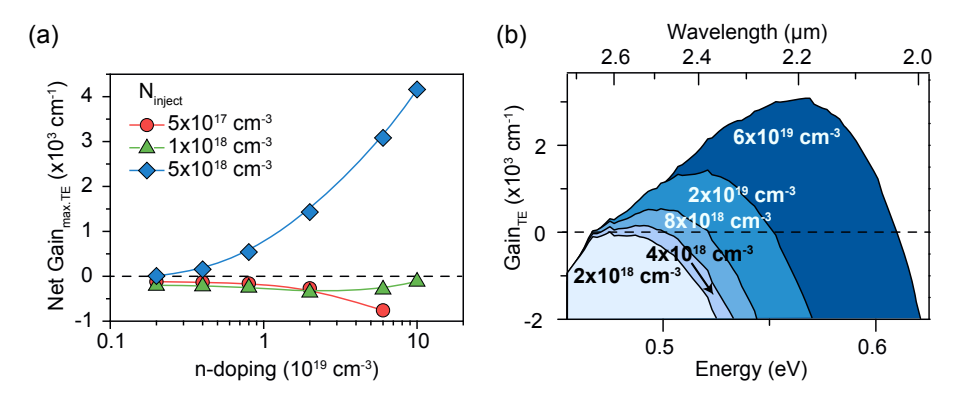


Figure 5.9. Material gain calculation of $Ge_{0.875}Sn_{0.125}$, including free carrier absorption, at different injection carrier densities depending on n-doping concentration. In (a), the maximum of the in-plane (TE) net gain is plotted. (b) Gain spectra at an injection carrier density of 5×10^{18} cm⁻³ at different doping concentrations are shown. Calculations were conducted by *D. Rainko*.

shown for different doping concentrations in figure 5.9b. At doping concentrations above $2 \times 10^{18}\,\mathrm{cm^{-3}}$ gain rises for increased doping without attaining a saturation regime.

Experimental studies on the effect of doping in indirect bandgap GeSn show a PL intensity enhancement for n-doped layers,⁸³ which can be also observed in pure Ge,¹⁹⁸ together with bandgap narrowing effects. This behavior was confirmed also for direct bandgap GeSn layers accompanied with a clear peak broadening of n-doped layer PL.¹⁹⁹ Any experimental study on lasing of n-doped GeSn is missing. In the following section, a set of three differently n-doped Ge_{0.875}Sn_{0.125} layers is analyzed via PL measurements of the unprocessed layer and PL of microdisk cavities.

5.4.1. Material Overview

Phosphorous doped $Ge_{0.875}Sn_{0.125}$ layers with similar thickness but different doping concentrations were grown. ECV measurements of the samples in figure 5.10a show n-type doping levels in blue, orange and red. As explained in section 4.1, ECV

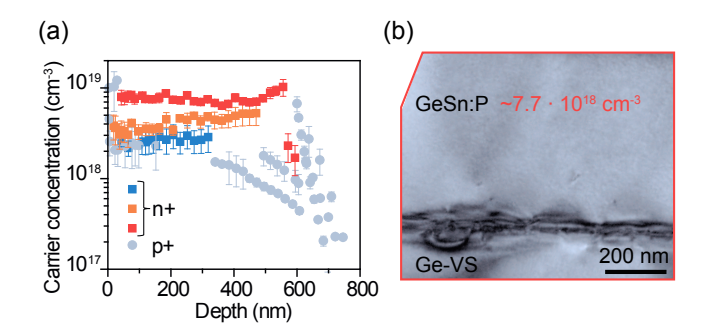


Figure 5.10. (a) ECV measurement of three differently doped $Ge_{0.875}Sn_{0.125}$ layers. Grey data points refer to the p-type background doping common for GeSn layers. (b) X-TEM of the layer with an average doping concentration of 7.7×10^{18} cm⁻³ reveals defects close to the interface between Ge-VS and GeSn layer.

name	$\begin{array}{c} \text{doping} \\ \text{concentration} \\ \text{(cm}^{-3}) \end{array}$	thickness (nm)	Sn (at.%)	strain (%)	bandgap (meV)	$\begin{array}{c} \text{directness} \\ \text{(meV)} \end{array}$
С	2.7×10^{18}	568	12.7	-0.34	495	61
D	4.1×10^{18}	569	12.7	-0.14	486	76
\mathbf{E}	7.7×10^{18}	546	13.2	-0.43	485	62
Ref.	-	560	12.5	-0.40	504	53

Table 5.4. Sample properties of n-doped $Ge_{0.875}Sn_{0.125}$ layers and the undoped reference sample.

seems to overestimate doping concentrations. An overview of the sample properties is given in table 5.4. The layer quality is influenced by strain relaxation in these relatively thick samples, leading to a misfit dislocation network at the interface to GeSn, which is visible in figure 5.10b. Besides defect loops parallel to the TEM cross section, threading dislocations in perpendicular direction can be detected as darker points.

Before lasing is investigated, the unprocessed layers are characterized by PL measurements, shown in figure 5.11. Normalized spectra in (a) show the peak broadening of at least $\sim 35 \,\mathrm{meV}$ for n-doped samples in comparison to an undoped $\mathrm{Ge_{0.875}Sn_{0.125}}$ (FWHM of 27 meV) layer with similar thickness and strain. Noticeable is also the peak evolving around $0.4 \,\mathrm{eV}$, which is cut at $0.37 \,\mathrm{eV}$ due to a filter in the set-up.

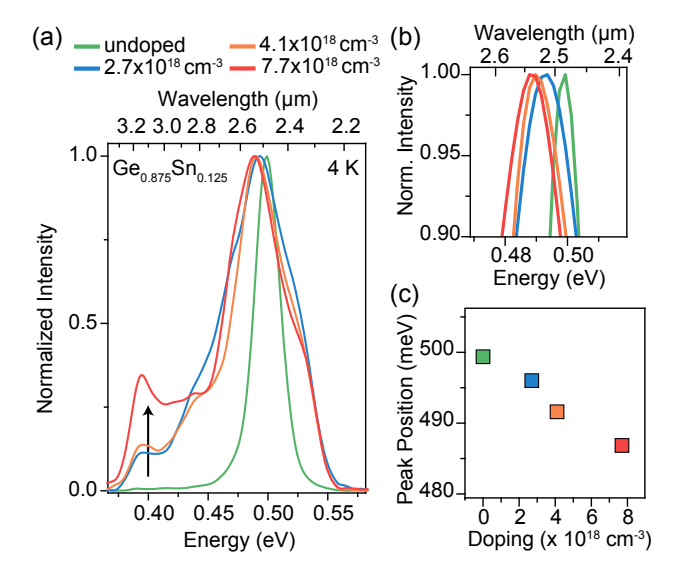


Figure 5.11. (a) Normalized PL of n-doped and undoped $Ge_{0.875}Sn_{0.125}$ layers at 4 K. The arrow indicates radiative defect recombination. (b) shows a zoom to the peak region of (a) and (c) gives an overview of the fitted peak positions.

The peak, which is attributed to radiative defect recombination, increases at higher doping concentration, suggesting a rising defect density related to the increased doping concentration. Optimized epitaxial growth could increase the material quality and reduce the defect recombination here. The peak shift between the individual samples is resolvable as can be seen in figure 5.11b, with the fitted peak positions plotted in figure 5.11c. For increased doping concentration, the emission energy is decreased, which is partly attributed to the difference in band structure, but also a sign for bandgap narrowing, refer to table 5.4. The extracted peak energies match the calculated bandgaps within the uncertainties of strain and Sn content determination.

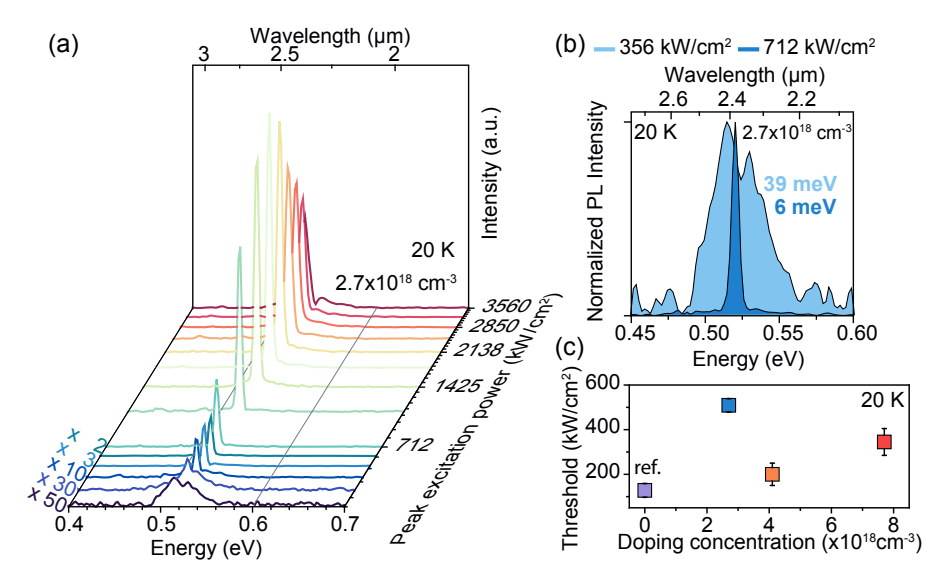


Figure 5.12. Lasing of n-doped GeSn MDs. (a) Power dependent spectra of MD-C at 20 K and (b) the line width collapse of the same sample at increased pumping power is shown. Thresholds of all three samples at 20 K are evaluated and depicted in (c).

5.4.2. Lasing Characteristics

The same fabrication process as before is used to fabricate MD cavities from n-doped layers. Power dependent spectra at 20 K of a disk with $2.7 \times 10^{18} \, \mathrm{cm^{-3}}$ doping is shown in figure 5.12a. For the lowest pumping powers, spectra are multiplied to ease the identification by factors written at the left border of the plot. With increased pumping, the spectra show a transition from broad, spontaneous to narrow, stimulated emission. Above $2 \, \mathrm{MW \, cm^{-2}}$ the intensity decreases again, comparable to the roll over observed for MD lasers in section 5.3. The transition to lasing is accompanied by line width collapse, which can be observed in the normalized intensity plots at $356 \, \mathrm{kW \, cm^{-2}}$ and $712 \, \mathrm{kW \, cm^{-2}}$ in figure 5.12b. FWHMs decrease from 39 meV to 6 meV measured with a resolution of $32 \, \mathrm{cm^{-1}}$. Lasing thresholds are evaluated from the integrated intensities of the power dependent spectra at $20 \, \mathrm{K}$ for each of the three samples. They lie in a range between $(509 \pm 30) \, \mathrm{kW \, cm^{-2}}$ (MD-C)

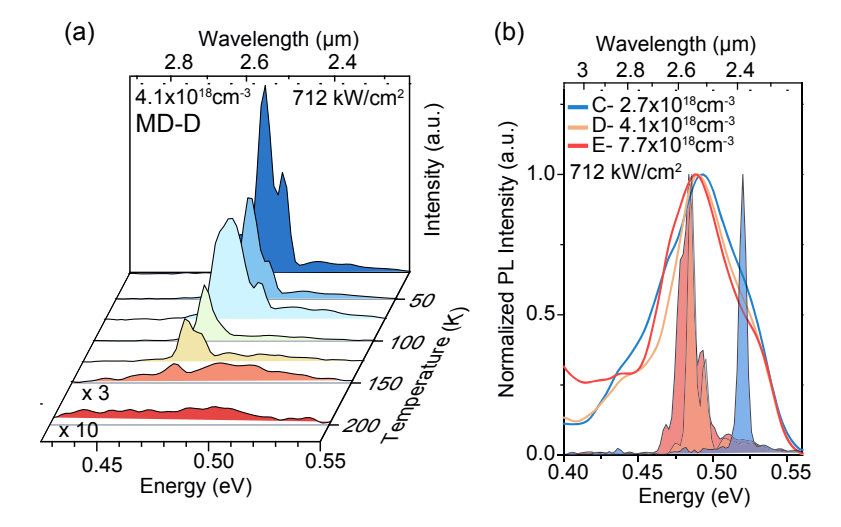


Figure 5.13. (a) Temperature dependent PL spectra of MD-D shows lasing up to $125\,\mathrm{K}$ at a peak power density of $712\,\mathrm{kW\,cm^{-2}}$. (b) Comparison of normalized spectra of lasing emission at $20\,\mathrm{K}$ to unprocessed layer PL at $4\,\mathrm{K}$.

and (200 ± 50) kW cm⁻² (MD-D) comparable to but higher than threshold values of single layer MD lasers. Gain calculations of material with properties equal for the three layers from table 5.4 reveal different trends of gain in in- and out-of-plane direction. For the in-plane direction, the gain maximum increases for increased doping concentration. In contrast, for the out-of-plane direction the maximum calculated gain values for three ascending doping values mirror the trend of extracted threshold values (C- 7782 cm⁻¹, D-11950 cm⁻¹ and E- 8831 cm⁻¹). However, the light detection during measurement is done in z-direction of the MD, and the detected light is scattered from the imperfections at the disk's edges. No experiments on the light's polarization have been performed. The trend of thresholds is also strongly influenced by material defects and the directness of the alloys.

The temperature dependence of MD-D is shown in figure 5.13a. At pumping of $712 \,\mathrm{kW \, cm^{-2}}$, the spectra become broader due to multiple mode lasing, which cannot be resolved at the resolution of $32 \,\mathrm{cm^{-2}}$. The maximum observable lasing temperature is $125 \,\mathrm{K}$. For even higher pumping of $1.4 \,\mathrm{MW \, cm^{-2}}$, modes are observed until

150 K with a broad background. This behavior is similar to the measurements of undoped Ge_{0.875}Sn_{0.125} MDs in section 5.3. Temperature limitations are attributed to a combination of still moderate directness, defect and Auger recombination at higher temperatures and stronger pumping.

A normalized comparison of laser emission at 20 K and PL emission of unprocessed samples at 4 K reveals a remarkable characteristic of MD-C with the lowest doping. While MD-D and E emit coherent light at energies slightly below the PL emission energies of unprocessed layers, the laser emission of MD-C is blue shifted. The behavior of the former can be explained with the interplay between relaxation of the lattice, caused by the undercut geometry and the high pumping needed for population inversion, increasing the emission energy. In the case of MD-C two explanations might be valid. Since the Sn concentration declines from the center to the edge of the wafer, a sample from the edge would have a lower Sn concentration, which could cause an energy shift in different pieces of the wafer. Another explanation could also be a different mode that emits at higher energies.

Summarizing, lasing was observed for MDs of GeSn with three different n-doping concentrations. A systematic trend to lower (higher) threshold (gain) for increased doping, could not been proven in the experiment. The extracted threshold values are all above those for the undoped MDs, indicating a degrading material quality in n-doped layers. Therefore, no advantage for the lasing performance with doping was found. However, not all observed trends were understood and require a more comprehensive study to exclude any advantage of doping.

In the next section, a more advanced approach than doping is investigated by the utilization of heterostructures.

5.5. GeSn/SiGeSn Heterostructure Lasers

As is known from the development of III-V lasers, heterostructures improve the performance of lasers by confining carriers to the active regions.^{73,200} With the concept of double heterostructures it was possible to reduce threshold values of GaAs-AlGaAs lasers about one order of magnitude compared to GaAs bulk.²⁰¹ The next devel-

opment of quantum well (QW) lasers, which came up ten years later, led to even lower thresholds. A reduction of the threshold by more than a factor of 5 through a change of DOS in 2D structures was achieved. In those QW structures, the DOS follows a Haeviside function and the number of states is reduced by confinement in one direction, which facilitates inversion population. Following this trend, around the year 2000, 0D quantum dot structures offered a DOS, described by a δ -function, and confinement in three directions reaching the lowest thresholds until then. Weeping the background of III-V lasers history in mind, the next step from single layer GeSn lasers is the application of heterostructures. Already in 2003 first GeSn/SiGeSn heterostructures were grown by ultrahigh vacuum CVD. After that, more advanced structures like DHS and QWs followed, whereas most of them exhibit an indirect bandgap active material.

Details regarding the heterostructure growth of samples used in the following, can be found in references [8, 63]. MD cavities are fabricated from the previously discussed material stacks in section 3.2. An overview on band structure and material properties of those stacks, namely DHS, MQW1 and MQW2, can be found there. The next subsection deals with strain distribution and band structure of an MD processed from MQW1. Later a comprehensive lasing measurement study is presented. Some of the conclusions have been published in references [6, 11].

5.5.1. Strain and Band Structure in Undercut MQW Microdisks

Since the heterostructures are all grown on $Ge_{0.90}Sn_{0.10}$ buffers, which also withstand the selective CF_4 etching, the microdisks consist of the GeSn/SiGeSn heterostructures as well as the GeSn buffer. Caused by the different Sn contents of the layers, the strain relaxation process of a layer stack with varying lattice constants differs compared to the single layer disks in section 5.3. As an example, the properties of an MQW1 MD are discussed in the following.

Figure 5.14a shows an SEM micrograph of an $8\,\mu m$ diameter disk with $3.5\,\mu m$ undercut, similar to all MD lasers discussed before. A zoom on the disk itself shows the multi layer stack on top of the buffer with its relatively rough side wall at the

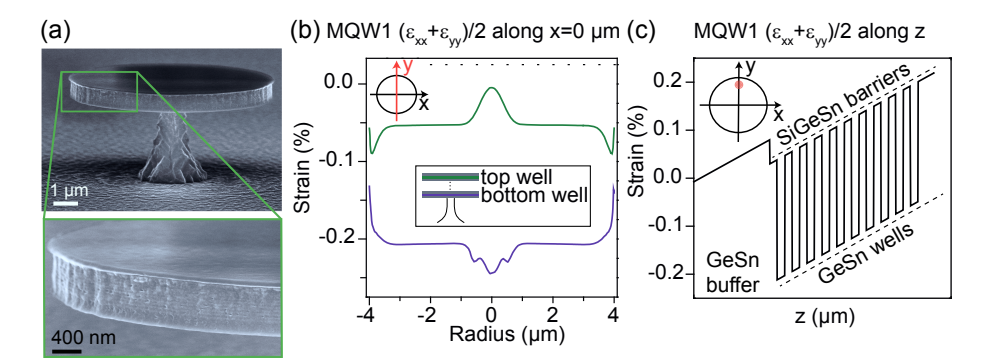


Figure 5.14. (a) SEM of an MD cavity from sample MQW1 with 3 μm undercut. The zoom-in reveals the buffer and MQW structure. Strain calculations along different directions by courtesy of *B. Marzban*, (b) for the bottom and top well along radial y-direction and (c) along z-direction at a point indicated in the inset of the disk. Adapted with permission from [6]. Copyright 2018 American Chemical Society.

circumference. In a first step, the strain distribution inside the MD is considered in radial direction. In a completely relaxed alloy the buffer material Ge_{0.90}Sn_{0.10} would have an in-plane lattice constant of 5.74 Å, the barrier of 5.76 Å and the active wells of 5.77 Å. The interplay between relaxation of the different layers leads to the final strain distribution of the disk. This means, none of the layers is fully relaxed and strain decreases slightly in z-direction (corresponding to [001] direction of the crystal), perpendicular to the disk surface. This behavior is also influenced by a downwards bending of the disk of calculated 43 nm at its rim. The strain component $\frac{1}{2}(\epsilon_{xx} + \epsilon_{yy})$ along the radius in y-direction is shown in figure 5.14b for the top (green) and bottom (violet) well by courtesy of B. Marzban. In the bottom well, the region above the pillar remains stronger partially strained as the undercut region. Such distribution is also known from the single layer disks, while in the case of MQW1, due to the constraining buffer, the relaxation at the bottom disk edge leads to a compressive strain of -0.2%. The sudden changes at the outer rim of the disk are numerical artefacts without physical relevance. Due to the bending of the disk, the top well is slightly tensily strained with a peak of the strain in the pillar region. At the rim, the top well reaches a strain of -0.05%. The strain in z-direction at $x = 0 \, \mu m$ and $y = 2.9 \, \mu m$, which is indicated by the red point in the

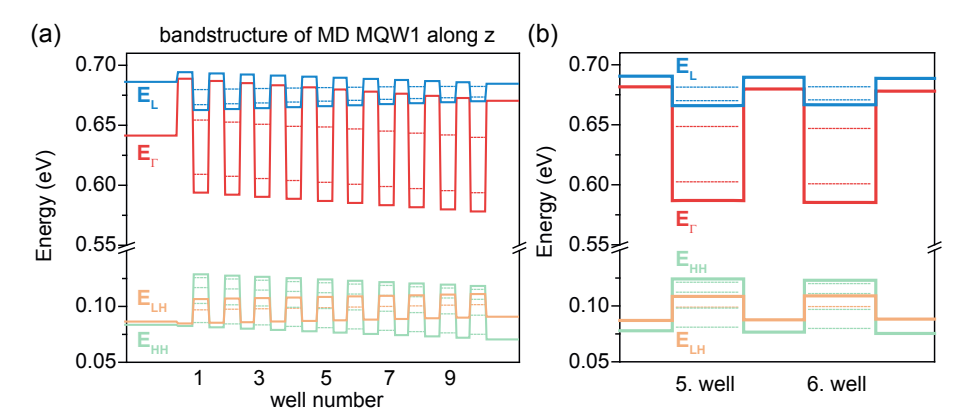


Figure 5.15. (a) Band structure calculation of MQW1 MD at 4 K along z, based on previous strain calculations. (b) A close-up on the 5th and 6th well in the middle. Adapted with permission from [6]. Copyright 2018 American Chemical Society. Courtesy of *D. Rainko*.

inset, is depicted in figure 5.14c. Caused by the difference in material composition, the GeSn wells are more compressively strained than the SiGeSn barriers which become more tensile, the closer they are to the top surface of the disk. This behavior will lead to slight changes in the band structure, as discussed in the following. Based on strain simulations, band structure calculations are conducted by D. Rainko with the results shown in figure 5.15. In figure 5.15a the cut in z-direction through the whole layer is plotted, while 5.15b shows an excerpt from the two middle wells for a closer view. The impact of changes in strain distribution on the local band structure is marginal, but strain relaxation of the full disk slightly changes the band structure compared to the unprocessed layer. Different strains in barrier and QW will reduce the band offsets between the Γ -valleys in average from 79 meV to 77 meV. At the same time, the directness is increased by 26 meV to 47 meV accompanied by a decrease of the bandgap to \sim 480 meV.

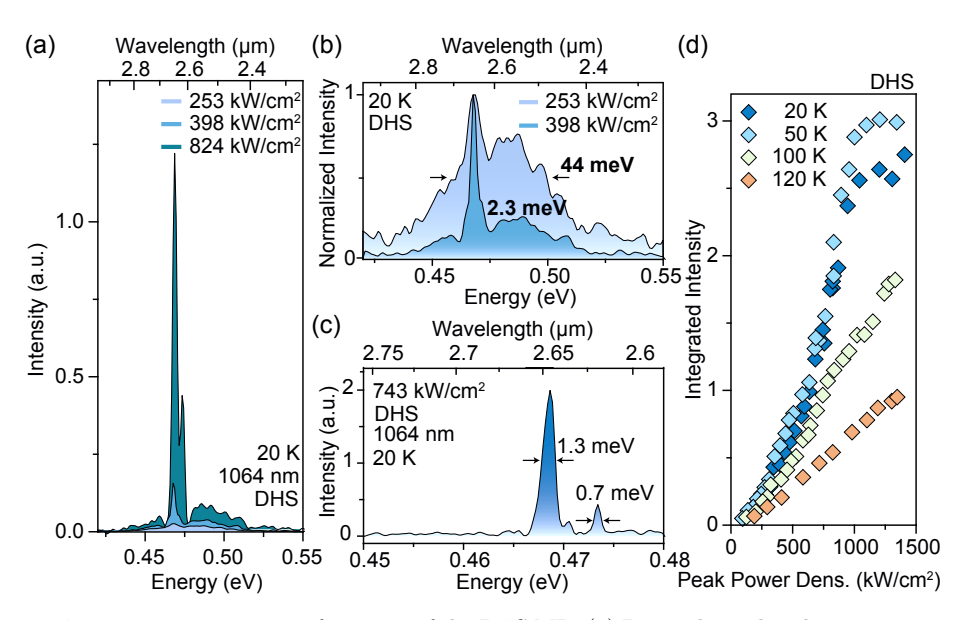


Figure 5.16. Lasing performance of the DHS MD. (a) Power dependent lasing spectra at 20 K pumped with Nd:YAG (1064 nm) laser. (b) Line width collapse and (c) high resolution spectrum $(4\,\mathrm{cm}^{-1})$ at 20 K. In (d) LL curves at four different temperatures are depicted. Adapted with permission from [102]. Copyright 2018 American Chemical Society.

5.5.2. Lasing Characteristics

Microdisks of the three material stacks are investigated in the same manner as the disk lasers before, only with the difference that two excitation lasers are used with wavelengths of $1550\,\mathrm{nm}$ ($0.8\,\mathrm{eV}$) and $1064\,\mathrm{nm}$ ($1.2\,\mathrm{eV}$). By pumping with $1550\,\mathrm{nm}$ wavelength, hot carriers shall be reduced and subsequently this impact is investigated.

Figure 5.16 shows the results of the DHS MD laser pumped at $1064\,\mathrm{nm}$. The low temperature power dependence in figure 5.16a shows the transition from spontaneous emission to lasing, which is specified by the normalized spectra in figure 5.16b when the line width decreases from $44\,\mathrm{meV}$ to $2.3\,\mathrm{meV}$. At a higher resolution of $4\,\mathrm{cm}^{-1}$, different peaks can be resolved and widths of $1.3\,\mathrm{meV}$ to $0.7\,\mathrm{meV}$ were obtained in

figure 5.16c, with Q factors between 350 and 600. As visible in the high resolution spectrum in 5.16c and the strongly pumped spectrum in 5.16a (824 kW cm⁻²), at higher photon injection the mode pattern changes. This behavior is also indicated in the LL curves in figure 5.16d when the slope efficiency increases above $650\,\mathrm{kW\,cm^{-2}}$ at temperatures of 20 K and 50 K. Lasing efficiency in general decreases with higher temperatures and already at 120 K the integrated intensity versus peak power density trend becomes linear indicating spontaneous emission behavior. The threshold at 20 K is extracted to be $(300 \pm 25) \,\mathrm{kW \, cm^{-2}}$. Compared to the single layer disk lasers, the characteristic of this DHS MD laser is slightly worse, the threshold is larger and the maximum lasing temperature lower. One of the reasons might be a higher Sn content in the DHS active layer, reducing the material quality of the alloy. The advantages of carrier confinement cannot be observed since the material exhibits a misfit dislocation network between bottom barrier and active layer. This provides non-radiative recombination centers degrading the positive effect of confining barriers, as already discussed in section 3.2. To investigate solely the impact of a DHS system on lasing, different samples without additional misfit dislocation network are needed.

In the following, the focus lies on MQW MDs, especially on MQW1 which already showed the most promising PL performance. Results of an MD laser, pumped by the 1064 nm laser, are summarized in figure 5.17. The line width collapse observed at 50 K is plotted in figure 5.17a, whereas the spontaneous emission is even more narrow as of the DHS MD. FWHMs below 1 meV are obtained in the highly resolved spectrum in figure 5.17b with Q factors between 570 and 650. LL-curves in figure 5.17c show lasing below 120 K, like for the DHS MD. However, the extracted threshold at 20 K is strongly reduced to $(35 \pm 4) \,\mathrm{kW\,cm^{-2}}$. This characteristic is attributed on one hand to the separation of defects from the active wells by the SiGeSn potential barriers at low temperatures. On the other hand, the reduced number of states is expected to strongly decrease the required excitation density to reach population inversion.

Exactly the same MD was investigated under $1550 \,\mathrm{nm}$ (0.79 eV) excitation and results are presented in figure 5.18. Power dependent spectra with $16 \,\mathrm{cm}^{-1}$ (a) and $4 \,\mathrm{cm}^{-1}$ (b) resolution show the mode evolution for higher pumping with comparable narrow line width and Q-factors as previously for $1064 \,\mathrm{nm}$ excitation at $20 \,\mathrm{K}$. Dur-

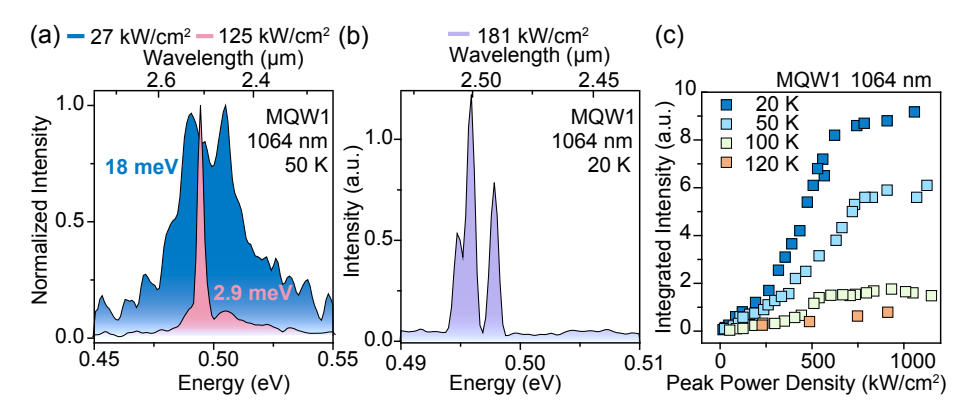


Figure 5.17. Lasing performance of MQW1 MD pumped with 1064 nm. (a) The line width collapse at 50 K is observed at the transition from spontaneous to stimulated emission. (b) A high resolution spectrum (4 cm⁻¹) at 20 K reveals three different modes. (c) LL-curves are shown up to 120 K. Adapted with permission from [6]. Copyright 2018 American Chemical Society.

ing mode analysis, it was possible to relate the three modes in the spectrum pumped at $187\,\mathrm{kW\,cm^{-2}}$ in figure 5.18b with energies at $494\,\mathrm{meV}$, $495\,\mathrm{meV}$ and $497\,\mathrm{meV}$ to WGM with different radial but same azimuthal numbers, meaning that the amount of maxima and minima of the standing waves differs along the radius for the different modes. At a peak power density of $670\,\mathrm{kW\,cm^{-2}}$, a dominant higher order mode evolves at $506\,\mathrm{meV}$, which might correspond to an increase of the azimuthal mode number by one. The possibility to assign different mode numbers to the spectra confirms the observation of WGM.

Temperature dependent LL-curves are depicted in figure 5.18c with a threshold of $(45\pm3)\,\mathrm{kW\,cm^{-2}}$ at 20 K and confirm previously measured low threshold results under 1064 nm excitation. The primary idea of pumping with a lower energy laser was to improve the laser performance by reducing the amount of excited hot carriers. In regard to the threshold this expectation was not met, meaning the hot carriers do not seem to be the main obstacle for low lasing thresholds at cryogenic temperatures. However, LL-curves for increased temperatures in figure 5.18c show lasing above 120 K, in contrast to the data measured under 1064 nm pumping.

A more detailed comparison of the temperature characteristics of the MD laser for

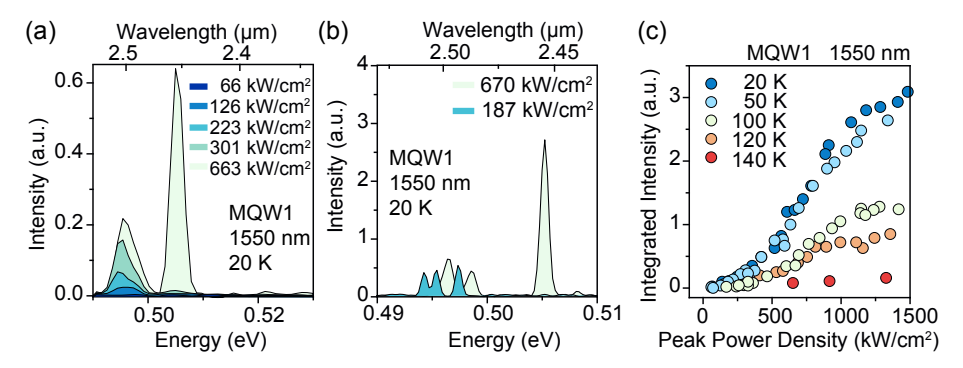


Figure 5.18. Lasing performance of MQW1 MD pumped with 1550 nm. (a) Power dependent spectra with a resolution of 16 cm⁻¹. (b) Highly resolved spectra (4 cm⁻¹) at two different peak power densities. (c) LL-curves at five different temperatures. Adapted with permission from [6]. Copyright 2018 American Chemical Society.

different excitations is given in figure 5.19. LL-curves for both pumping wavelengths are juxtaposed at 20 K and 120 K in figure 5.19a and b, respectively. The overall pumping efficiency of excitation at 1550 nm is seen by the higher intensity of the respective LL-curve and its saturation at higher peak power densities. Additionally, when the integrated intensity of MDs pumped with 1064 nm already becomes linear, MDs pumped with 1550 nm still exhibit lasing at 120 K. Spectra pumped with different lasers at $660\,\mathrm{kW\,cm^{-2}}$ and $450\,\mathrm{kW\,cm^{-2}}$ in figure 5.19c support the analysis of integrated intensities. At 120 K the spectrum pumped with 1064 nm becomes broad indicating spontaneous emission, while the spectrum measured at 1550 nm excitation still shows a distinct laser peak. To verify that this difference is not caused by the different peak power densities, the inset of figure 5.19c shows a spectrum at 120 K and 1190 kW cm⁻² pumped with 1064 nm, showing spontaneous emission, while evolving modes are slightly visible. In that regard, the advantage of lower energy pumping is obvious and is attributed to lower excess photon energy (difference between excitation and emission energy) of 0.30 eV compared to 0.66 eV for the 1064 nm laser even if the absorption for longer wavelength is lower. A similar effect was observed by pumping with 1064 nm and 1950 nm resulting in an increase of maximal lasing temperature of 30 K.²⁰⁶

At the end, the MQW2 MD is studied. Indicated by the worse PL efficiency, the

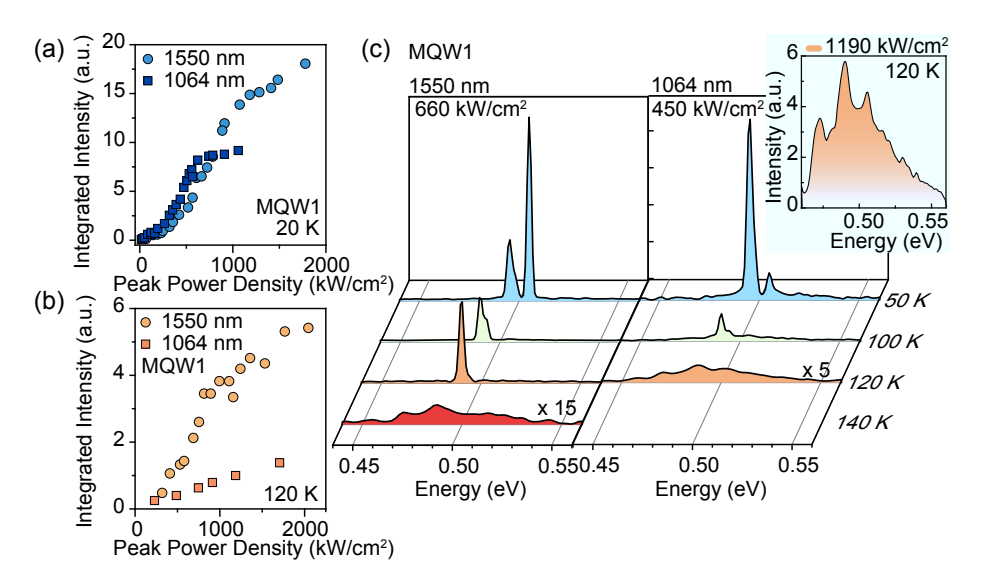


Figure 5.19. Temperature dependent lasing performance of MQW1. LL curves at 20 K (a) and 120 K (b) for pumping with 1550 nm and 1064 nm excitation. (c) Lasing spectra at increasing temperatures with $660 \,\mathrm{kW} \,\mathrm{cm}^{-2}$ (at $1550 \,\mathrm{nm}$) and with $450 \,\mathrm{kW} \,\mathrm{cm}^{-2}$ (at $1064 \,\mathrm{nm}$). The inset shows a spectrum pumped with $1064 \,\mathrm{nm}$ at $120 \,\mathrm{K}$ for an excitation density of $1190 \,\mathrm{kW} \,\mathrm{cm}^{-2}$. Adapted with permission from [6]. Copyright 2018 American Chemical Society.

expectations regarding lasing are low. Figure 5.20 shows its lasing spectra measured at 20 K with both excitation lasers. In every case, the required peak excitation power was much higher compared to the other MD lasers. While laser emission, excited by the 1064 nm laser, shows only broad peaks, spectra under 1550 nm pumping exhibit signs of lasing at peak power densities above 1.8 MW cm⁻². At 20 K even the LL-curve in figure 5.20b shows a power dependent change in the slope efficiency, however it is questionable if coherent lasing emission can be reached here. Since lasing was also observed in MDs with 8.5 at.% Sn and very low directness, the weak performance of MQW2 MD cannot only be ascribed to the directness. In this case, the amount of active material is very small, compared to MQW1 and DHS, and the mode cannot be confined very well in the lasing material of cumulative 120 nm. Furthermore, through the strong quantization in very thin QWs, excited carriers might be pushed into the buffer and barrier material of the disk. By comparing the

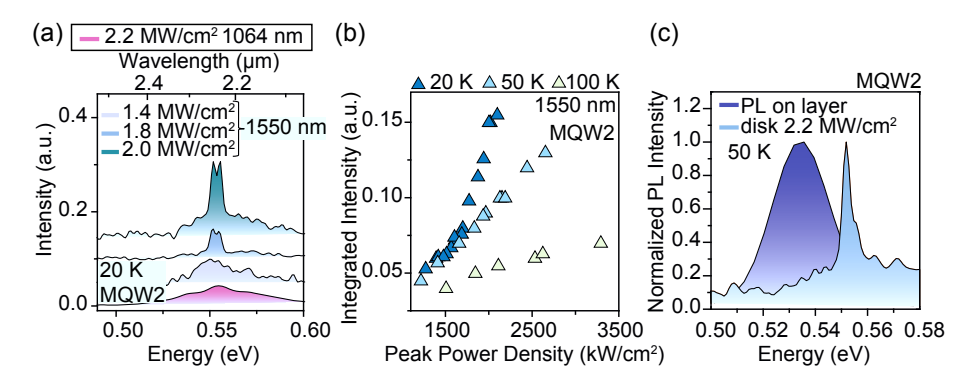


Figure 5.20. Lasing performance of an MQW2 MD. (a) Spectra at very high pumping above 1 MW cm⁻² show only an onset of lasing pumped with 1550 nm, in contrast only spontaneous emission for pumping with 1064 nm. (b) Integrated intensities at three temperatures pumped with 1550 nm. (c) Comparison of PL spectra of unprocessed layers and a lasing spectrum at 50 K. Adapted with permission from [6]. Copyright 2018 American Chemical Society.

emission energy of PL from an unprocessed layer (violet) at 535 meV and MD (blue) at 552 meV in figure 5.20c, the emission is blue shifted. This behavior was only observed for one of the doped MDs, while in all other cases the peak was similar or red shifted due to relaxation of the disks compared to unprocessed layers. Regarding the band structure of MQW2, the bandgap of the unprocessed active material is calculated to be at 529 meV and 550 meV for the buffer layer. While these values might be a little reduced in a more relaxed disk system, it is obvious, that laser emission is better matched by the buffer bandgap, than that of the active material. These results show the unsuitability of too strongly quantized 2D GeSn/SiGeSn systems, degrading the benefit of 2D confining heterostructures for lasing.

In a last paragraph lasing of different disks is compared. LL-curves at 20 K of MQW1 and DHS MD, excited by the 1064 nm laser, are overlaid in figure 5.21a revealing not only a smaller lasing threshold, but also an emission intensity increase by a factor of ~ 3 . The threshold determination for the following comparison was done with two different data sets and then averaged between the two obtained values. The procedure is exemplarily shown in figure 5.21b. On one hand the integrated intensities from the lock-in amplifier were taken (violet data points). On the other

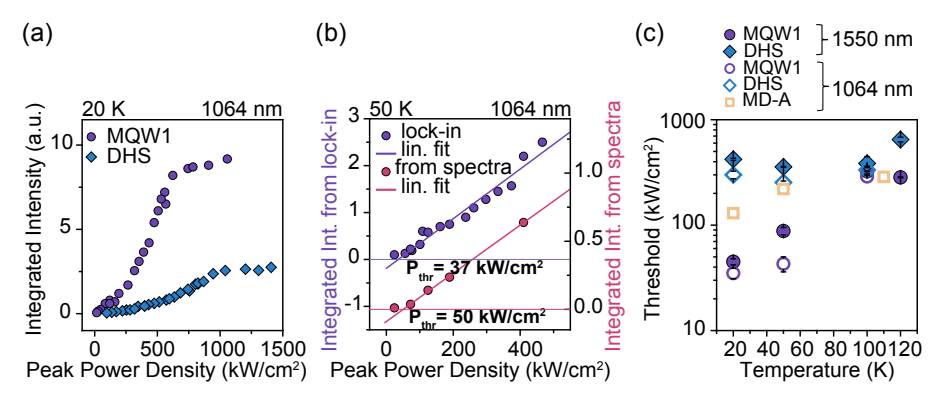


Figure 5.21. (a) Comparison of LL curves at $50\,\mathrm{K}$ of MQW1 and DHS MDs pumped with $1064\,\mathrm{nm}$. (b) Example of threshold determination for heterostructure MDs. (c) Comparison of threshold values from DHS and MQW1 pumped with different excitation lasers and a single layer $\mathrm{Ge_{0.875}Sn_{0.125}}$ MD. Adapted with permission from [6, 102]. Copyright 2018 American Chemical Society.

hand, the integrated intensities of individual spectra were extracted and plotted against the peak power densities (pink points). Lines were fitted to the low injection region, where lasing was observed, and the intersection with the abscissa gives the extracted threshold value. Thresholds of MQW1 DHS and single layer MDs are compared in figure 5.21c including pumping under the two excitation lasers. The plot clearly illustrates that the MQW1 MD outperforms MD-A and DHS MDs at temperatures below 100 K. While threshold values of the single layer and DHS MD stay almost constant, a strong temperature dependent trend to higher thresholds for increasing temperature is observed for the MQW1 MD. At elevated temperatures, the electron quasi Fermi level increases leading to a higher L-valley occupation due to the moderate directness $\Delta E_{L\Gamma}$ and smaller density of states at Γ . Additionally, the thermionic energy enables carriers to overcome potential barriers and reach defective interfaces. Both points will lead to more non-radiative recombination and losses that have to be saturated before reaching population inversion, causing the temperature dependent threshold evolution. A similar effect was discussed during the PL study in section 3.2. Lasers from MQW1 system showed the superiority of 2D and confining heterostructures in terms of lasing threshold and emission intensity at low temperature. Still, a lot of optimization has to be done. The processed

disks have a rough surface inducing optical losses and increasing the threshold. Also the heterostructures have to be more effective in confining carriers. A comprehensive study of suitable SiGeSn barrier and GeSn well combinations can be found in reference [207].

5.6. Summary

This chapter dealt with the study of various GeSn microdisk lasers. Undercut MD lasers from single GeSn layers with different Sn concentrations are fabricated and analyzed. They reveal lower threshold and higher lasing temperatures than non-undercut FP cavities of similar material. To further improve the performance, studies on n-doped GeSn, as well as on heterostructure MD lasers were conducted. Lasing, investigated from n-doped GeSn disks, shows no improvement in threshold or lasing temperature due to a high defect density. In contrast, heterostructures of GeSn/SiGeSn MQWs are found to exhibit a considerable threshold reduction at low temperatures.

The main results of the previous chapter are summarized in the following items.

- Microdisk cavities were fabricated and analyzed. Strain relaxation at the rim of the undercut MDs was experimentally confirmed by Raman and PL measurements. Single layer disks of $8\,\mu m$ diameter and an undercut of $3.5\,\mu m$ have a fully relaxed lattice in the undercut region.
- First lasing at two different wavelength from $2.0\,\mu\mathrm{m}$ to $2.5\,\mu\mathrm{m}$ from GeSn MDs was demonstrated in single layer disks by line width narrowing, trend of LL characteristics and optical mode analysis. One disk consisting of an alloy with $12.5\,\mathrm{at.\%}$ Sn has a direct bandgap, the other disk with $8.5\,\mathrm{at.\%}$ Sn is just at the transition to a direct bandgap semiconductor.
- In general, higher maximum lasing temperatures were ascribed to a larger directness of the alloy.

- For single layer lasers, the lowest threshold was found for the MD with less Sn. This was attributed to the higher material quality for lower Sn content alloys as well as the decreased overlap of the mode with surfaces caused by a larger active volume.
- The undercut $Ge_{0.875}Sn_{0.125}$ MD laser achieved higher lasing temperature and lower thresholds than the same FP cavity laser (130 K versus 90 K and $(130 \pm 31) \, \mathrm{kW \, cm^{-2}}$ versus $325 \, \mathrm{kW \, cm^{-2}}$) due to reduced surface recombination at a passivated surface, better mode confinement and a modified directness of the undercut geometry.
- Lasing was shown for n-doped Ge_{0.875}Sn_{0.125} MDs. However, measurements deliver inconclusive results. All obtained threshold values lie above the once of undoped lasers, indicating a decreased material quality in the doped layers. A benefit of doping by increased carrier numbers could not be confirmed.
- Lasing was shown for the first time in GeSn/SiGeSn double hetero- and multi quantum well structures.
- DHS MDs showed comparable performance as single layer MDs, due to the drawback of a second misfit dislocation network close to the active region, which degrades the advantage of carrier confining barriers.
- One order of magnitude lower thresholds are required for the MQW1 MD laser, namely $(35\pm4)\,\mathrm{kW\,cm^{-2}}$ at 20 K, demonstrating the benefit of carrier confinement and 2D DOS.
- MQW1 MDs exhibited a temperature dependent increase of threshold and temperature limitations in lasing. These are ascribed to the moderate directness and barrier offsets which both lead to a carrier filling of L-valleys and buffer material at elevated temperatures.
- Lasing from MQW2 MDs was hardly observed. Therefore, it can be concluded that a trade-off between barrier heights and thickness of the wells has

5. Optically Pumped Lasers

to be carefully chosen to avoid degrading the lasing performance by too strong quantization effects.

6. Towards Electrically Pumped Lasing

For the implementation of a GeSn laser on a chip, electrical injection is mandatory. Until now, only GeSn-based LEDs are developed. This chapter provides brief insight into the fabrication of structures for future electrically pumped lasers.

Several constraints have to be imposed to achieve electrically pumped lasing. Losses through metal contacts have to be avoided and a strong mode confinement in the active GeSn layer is needed, when the Ge-VS underneath is still present.

A design with certain GeSn/SiGeSn heterostructure stacks was developed using simulations by *Bahareh Marzban* from *IPH*, *RWTH Aachen University*. These layouts, which include micro ring as well as waveguide cavities, were used to develop a process flow for the fabrication of electrically pumped structures. Schematics of the two basic designs are depicted in figure 6.1a and b, respectively.

The process development was done on GeSn/SiGeSn heterostructures. An addi-

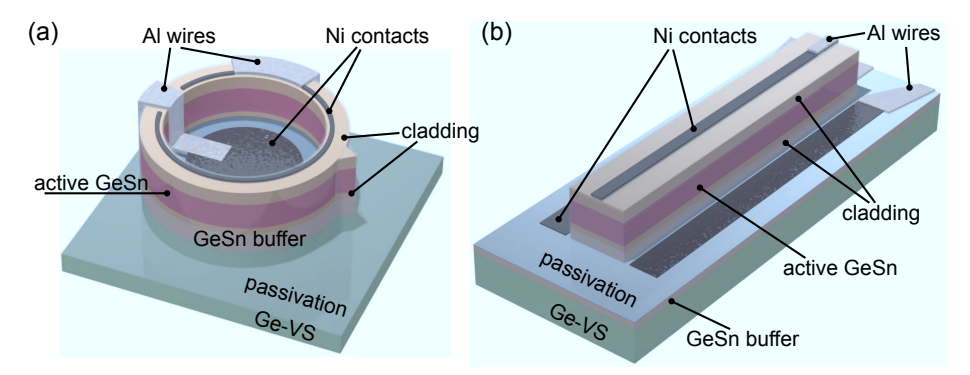


Figure 6.1. Sketch of the design layouts for micro ring (a) and FP lasers (b) with an example of a DHS layer stack.

tional approach was started to increase the top layer thickness of a GeSn/SiGeSn MQW stack and therefore increase the distance between active layer and metallic contacts. The MQW1 sample from previous chapters, which includes an unintentionally p-doped GeSn buffer layer, was used for testing growth of antimony (Sb) doped Ge on top by molecular beam epitaxy (MBE). To avoid Sn precipitations, the growth temperature in the MBE chamber was kept below 300 °C. Samples were cleaned in an HF(1%):HCl dip for 7 minutes, before they were transferred to the MBE chamber under nitrogen ambient. Growth tests were performed on different layer stacks with Sn content > 12.0 at.%. Figure 6.2a shows an ECV measurement of a Ge:Sb/GeSn:P test structure. Here, only the coloured distribution of Sb-doping is of interest. Antimony tends to segregate to the surface during MBE growth, which is used to achieve a graded doping concentration, as the blue data points indicate.²⁰⁸ At the top of the layer, where the metal contacts are intended to be, the doping concentration reaches a maximum far away from the GeSn active region, to reduce light absorption in the metal. Due to the lattice mismatch between Ge and the relaxed GeSn/SiGeSn stack, the Ge:Sb on top relaxes fast, which introduces many undesirable misfit dislocations, as can be seen in the SEM in figure 6.2b. The SIMS profile in figure 6.2c shows 200 nm Ge:Sb on top of the MQW1 stack. Due to contamination in the MBE chamber, the top layer also contains a significant Si content (violet line). However, at growth temperatures of 180°C Sn segregation is not visible, only the interface between MQW1 stack and Ge:Sb exhibits a peak in Sn and Sb content as well as in carbon and oxygen (not shown here), meaning there is a lot of potential to improve the interface.

The sheet resistances of this stack were measured with the van der Pauw method and offer values around $100\,\Omega/\Box$, which is acceptable since studies of GeSn:P revealed sheet resistances between $100\,\Omega/\Box$ and $500\,\Omega/\Box$. After these tests it seems to be clear that external overgrowth is quite challenging and an in-situ grown top layer would have the important advantage of a clean interface.

The previously mentioned simulation results were used to design masks for electron beam lithography containing several sizes of the cavities. For the micro rings, widths and diameters as well as the positioning of the contacts are varied and for waveguide cavities different lengths and widths are applied. The micro ring mesa process consists of two mesa etching steps. For the deep etching, SiO₂ hard masks

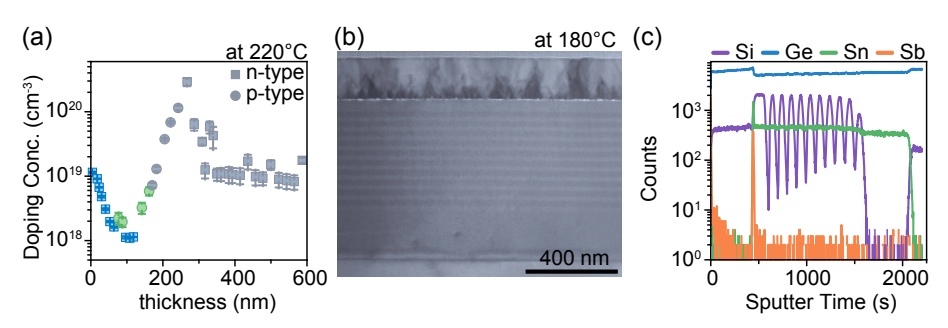


Figure 6.2. (a) Doping concentration of an Ge:Sb overgrown GeSn layer. (b) SEM of a Ge:Sb overgrown MQW1 stack. (c) SIMS profile of the layer stack in (b).

were used to avoid etching through the thinner nlof2020 resist. The first step defines the larger circles, which are dry etched in a combination of CHF₃ and Cl₂/Ar to 1.7 µm depth. In the second step, the ring is formed by etching a smaller circle till the bottom doped region of the material is reached. To uncouple the coherent light of the disk in a directed way, notch structures were partially included in the layout. SEM micrographs of two mesas with different sizes are depicted in figure 6.3a. The close-up at the top shows the overgrown MQW structure, while a notch for laser light uncoupling is visible on the bottom figure. After passivation with 10 nm HfO₂ and 250 nm SiO₂, nickel (Ni) ring contacts at the outside and circular contacts in the inside of the cavity are formed lithographically. Subsequently, the contact windows are defined to wire the smaller Ni contacts to the bondpads, which are realized by aluminum (Al) sputtering. In figure 6.3b, Ni contacts, as well as the open Al contact windows, can be seen in optical microscope images. Two completed ring cavities are displayed in figure 6.3c.

Processing the FP cavities follows the same route, only skipping the second mesa step. Different micrographs of the FP cavity fabrication process are illustrated in figure 6.3. An SEM after the mesa step is shown in figure 6.3d, followed by an optical micrograph after Ni contact formation in (e). Different length from $10\,\mu m$ to $500\,\mu m$ and width between $2\,\mu m$ and $6\,\mu m$ were fabricated. Structures before and after Al deposition are depicted in figure 6.3f and g, respectively.

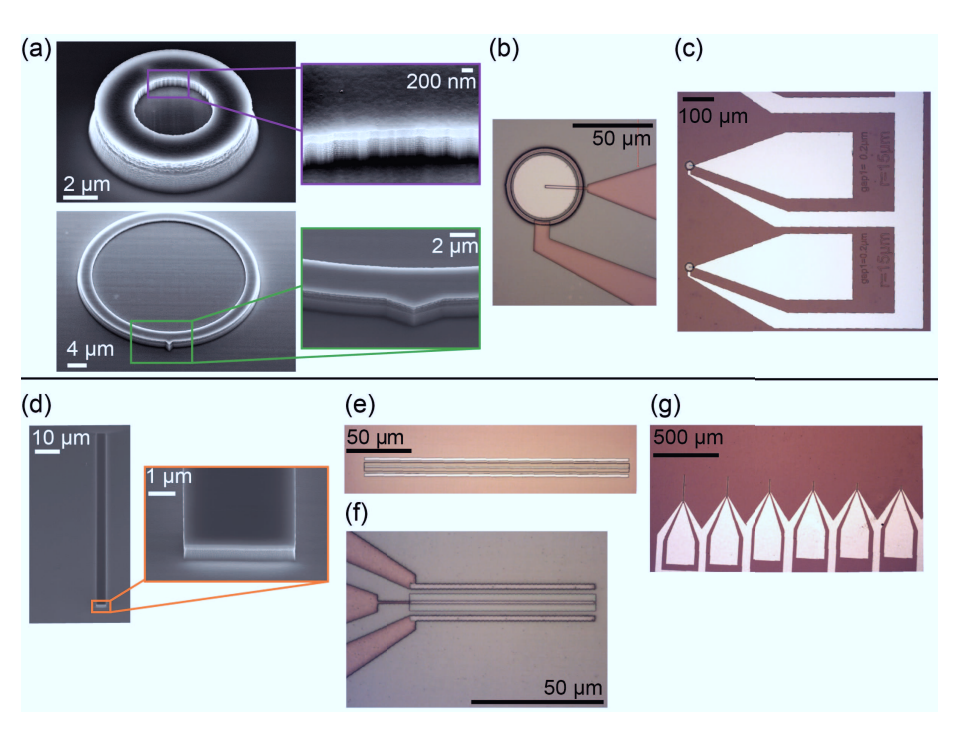


Figure 6.3. Micro ring cavities during process (a)-(c). (a) Mesa structures with zoom to the MQW structure (top) and zoom to the notch for light outcoupling (bottom). (b) Mesa with Ni contacts and open windows in SiO₂ for Al contacts. (c) Finished structure with Al contacts.

FP cavities during process show (d) a SEM of a mesa structure, (e) an optical microscope picture after Ni contact formation, (f) after window opening for Al contacts, and (g) some of the completed cavities.

The previously presented results show that the fabrication of electrically pumped GeSn/SiGeSn cavities with standard Si CMOS processing technology is possible. For the realization of such a laser, a suitable trade-off has to be found in growth between a doped GeSn buffer thickness, a pseudomorphically grown heterostructure stack and a relatively thick, lattice matched doping graded top layer, to avoid relaxation anywhere than at the Ge-VS/GeSn buffer interface. Even more advanced would be the application of a separate confinement heterostructure^{210,211} with an additional

wide bandgap cladding or a refractive index gradient 212 so that the optical mode is more strongly confined to the active region. There, a high Si incorporation might be beneficial. Other approaches like SiN stressor layers instead of SiO₂ passivation are under discussion, since it would help to decrease compressive strain or even tensily strain the GeSn layer stack.

7. Conclusion and Outlook

In the scope of this work, (Si)GeSn alloys were analyzed for the development of mid infrared group IV lasers. The primary focus was laid on the optical characterization and investigation of light emission. The suitability of the material system was revealed by detailed PL studies of direct bandgap GeSn alloys, which gave insight into their emission characteristics. Typical peculiarities of spontaneous emission in heterostructures showed prospects and challenges in the GeSn/SiGeSn system. First steps in the direction of light emitters were done by the fabrication of homo- and heterojunction LEDs. Therefore, similar material designs, as analyzed previously by PL, were used, proving the option of electrically pumped light emitters in this material system. For the generation of lasing, optical cavities are mandatory. Hence, lasing from microdisk cavities was comprehensively studied for various material configurations to confirm the applicability of the material for lasers. The first optically pumped lasing from GeSn microdisks could be observed. By the use of heterostructures, the threshold was tremendously reduced, but additional limitations of the system from strongly quantized energy states emerged. Finally, the development of a fabrication process of electrically pumped GeSn/SiGeSn micro ring and Fabry-Pérot cavities paves the way for one important future goal, an electrically pumped GeSn-based laser.

The influence of radiative and non-radiative recombination in GeSn alloys can be excellently probed by PL spectroscopy. Non-radiative defect recombination in GeSn showed a pronounced reduction for lower temperatures. In contrast, the electron population in Γ , increasing continuously for more direct alloys, enhances the radiative recombination rate and decreases for higher temperatures when the L-valley becomes more populated. Both aspects lead to a PL intensity increase with decreas-

ing temperature giving an indication of the directness of the alloy.

In this manner the purely strain-induced indirect-to-direct bandgap transition was demonstrated on the example of a $\rm Ge_{0.875}Sn_{0.125}$ series. It was shown that thicker layers lead to a higher strain relaxation by forming misfit dislocations. The trade-off between larger directness and material degradation, both provoked by strain relaxation, showed maximum performance at a thickness of 560 nm.

Consequently, defect engineering for heterostructures is essential to control defect formation close to the active region. Strain relaxed GeSn buffers offer a larger lattice constant for on top grown GeSn/SiGeSn heterostructures, which should avoid further strain relaxation of the latter. This aim was achieved for three different MQWs, but in a DHS, a second misfit dislocation network was formed caused by a beyond-critical volume strain. Low temperature PL probed the effect of carrier confinement to the active region, which includes the screening of carriers from the defective interface at Ge-VS, and quantization. This resulted in one order of magnitude higher PL intensity. For very thin wells (< 20 nm) the energy shift due to quantization becomes too large, pushing carriers out of the wells, decreasing barrier heights as well as the directness of the active material. Then, the benefit of confinement and increased intensity is lost. Temperature dependence of heterostructure PL is influenced by the barrier height, which was not sufficient to confine carriers at room temperature with the present SiGeSn composition.

After an extensive study of PL from various GeSn alloys and heterostructures, first light emitting devices were fabricated from simple p-i-n homojunctions with 8.5 at.%, 11.0 at.% and 13.0 at.% Sn. Electroluminescence shows similar temperature trends compared to PL investigations. Due to the different Sn concentrations, an emission wavelength tuning between $2.0\,\mu\mathrm{m}$ and $2.5\,\mu\mathrm{m}$ was possible. A strong performance degradation due to crystal defects was found in the highest Sn content LED with 13.0 at.% emphasizing the need of defect engineering.

The investigations were followed by two different MQW LED designs with Ge and SiGeSn as barrier material, respectively. While Ge turned out to be strongly tensily strained and therefore offering no efficient confinement for electrons, the performance of GeSn/SiGeSn MQW LEDs benefits at low temperature from carrier confinement and 2D density of states. The same advantages as from heterostructure PL studies were found, showing a promising strategy for GeSn heterostructures.

To move from the study of spontaneous to stimulated emission, GeSn microdisk lasers with a Ge-VS pedestal on Si were analyzed by micro-PL. The MD geometry for GeSn single layers leads to an almost completely strain-relaxed lattice in 8.0 µm diameters disks with 3.5 µm undercut. Compared to a non-undercut FP laser from the same $Ge_{0.875}Sn_{0.125}$ layer, the MD lasers reached a higher lasing temperature of $130\,\mathrm{K}$ and a lower threshold of $(130\pm31)\,\mathrm{kW\,cm^{-2}}$. These characteristics were attributed to a larger directness, surface passivation, as well as a better mode confinement given by the increased refractive index contrast of GeSn and air. Interestingly, also an MD with 8.5 at.% Sn and a low directness of only $\sim 14\,\mathrm{meV}$ showed typical signs of lasing, such as line width narrowing and S-shaped LL-curves. Even a reduced threshold of $(107\pm26)\,\mathrm{kW\,cm^{-2}}$ at 20 K was found, originating from higher mode overlap and better material quality. The lower directness only impacts the maximum lasing temperature, which is decreased to $90\,\mathrm{K}$.

The approach to increase gain and therefore the lasing performance by n-doping of single layers, indicated no benefit from the conducted experiments. While all of the MDs showed lasing, the performance was worsened pointing to a lower material quality.

The same heterostructures already analyzed in PL were used for MD cavities. The drawback of additional misfit dislocations at the interface to the active layer in the DHS MD was confirmed by laser performance, which was slightly worse than single layer MD lasers. However, MDs from an MQW design outperform all other MD lasers with a one order of magnitude reduced threshold of only $(35 \pm 4) \, \mathrm{kW \, cm^{-2}}$ at 20 K. This improvement is caused by the 2D density of states, as well as the carrier confinement screening them from misfit dislocation defects. The evolution of lasing with temperature is limited as seen from PL pre-characterization, so that stimulated emission is restricted to 120 K with increasing thresholds. A very strong quantization effect in MQW MDs with 12 nm QW width and a total amount of material of only 120 nm hinders the observation of distinct lasing in those structures. This emphasizes the need of a sophisticated trade-off between large energy barriers and a sufficient QW thickness to benefit from confinement and 2D density of states without losing the directness of the alloy.

Aiming for electrically driven GeSn lasers, a process flow for micro ring and FP cavities was developed based on simulated structure designs. With a suitable in-situ

doped heterostructure stack, the fabrication could be performed by means of standard Si CMOS technology.

The overall purpose is to develop a GeSn laser on a chip working at room temperature, which has not been realized yet. Some measures that can be taken to overcome the existing obstacles are discussed in the following. Studies show that the temperature limitations in lasing can be solved by increasing the directness of the active material. Two solutions are possible,

- (i) increase of Sn content, 50,160 or
- (ii) application of tensile strain by external stressor layers. 44,101,140,213

For the latter, lower Sn contents are feasible, which may avoid a large point defect density, expected for high Sn content alloys.

In heterostructures, the realization of large enough band offsets requires a higher Si incorporation, while keeping the Sn content in the well high enough for direct bandgap active layers. In this respect, the incorporation of carbon is debated to generate even larger band offsets and to decrease defect densities. Carbon could also help to suppress Sn precipitations during growth.^{214–216}

When these requirements are fulfilled, more advanced designs like a separate confinement heterostructures with larger barriers around the MQW and/or index graded claddings can be designed.

For electrically driven laser designs, a thick, doped top layer is needed to keep the electrodes away from the active region. Depending on the top material and its lattice constant, it is important to design the total stack in a way that further strain relaxation is avoided.

Improvement of the process modules for fabrication, e.g. decreasing the surface roughness, will strongly reduce losses and help to boost the laser performance.

To expand the general understanding of the laser and its limiting processes for light emission, it is crucial to accurately study radiative and non-radiative lifetimes in the GeSn material system. The same holds true for the band structure of SiGeSn, which is poorly understood up to date. Using such knowledge, simulations can be tweaked to design laser structures more accurately.

Overall, the great potential of (Si)GeSn was shown, as a promising group IV material system with many degrees of freedom for designing opto- and nanoelectronic devices on the Si platform. The use of OEICs or even devices like tunnel field effect transistors could significantly reduce the energy consumption of electronic chips. Furthermore, with its mid infrared bandgap it can enrich medical diagnostics, as well as gas- and bio sensing applications and might advance many interesting research fields in future.

A. Appendix

PL of heterostructures

A comparison of PL spectra of a $Ge_{0.875}Sn_{0.125}$ bulk layer to the heterostructures DHS, MQW2 and MQW3 is depicted in figure A.1a. The emission intensity of the bulk sample is lower compared to DHS, which can be described to the lower directness of the former of 52 meV. At 4 K also the intensity of MQW3 overcomes the bulk sample, which is caused by the screening of carriers from the misfit dislocation network at the interface to Ge-VS in MQW3. In the bulk sample, a part of the carriers recombines non-radiatively at these misfit dislocations.

At 295 K the intensity of the samples scales with their directness as well as available amount of active material (560 nm for the case of the bulk sample). Figure A.1b shows the carrier distribution in Γ , L (inside the active region), and in the barriers/buffer (here for Γ and L), for a given total electron concentration of $4 \cdot 10^{16}$ cm⁻³ averaged over the complete layer stacks. The data was provided by *Prof. J. Witzens* from *IPH*, *RWTH Aachen University*. Calculations for MQW1 are illustrated by solid, for DHS by dashed lines. Going from 4 K to 300 K the number of carriers in Γ changes dramatically for MQW1, as well as for DHS. At higher temperatures, carriers are easily able to overcome the energy barriers and start populating the SiGeSn barrier/cladding and GeSn buffer material. As already seen in bulk structures, at higher temperature electrons also scatter into the L-valley of the active layer and are not condensed in Γ anymore. The major difference between MQW1 and DHS is the temperature, when the distribution of electrons changes abruptly. Already at 100 K, the population of electrons at Γ is below 50%, which occurs for DHS at temperatures above 150 K. The earlier occupation of L-valley, barrier and buffer

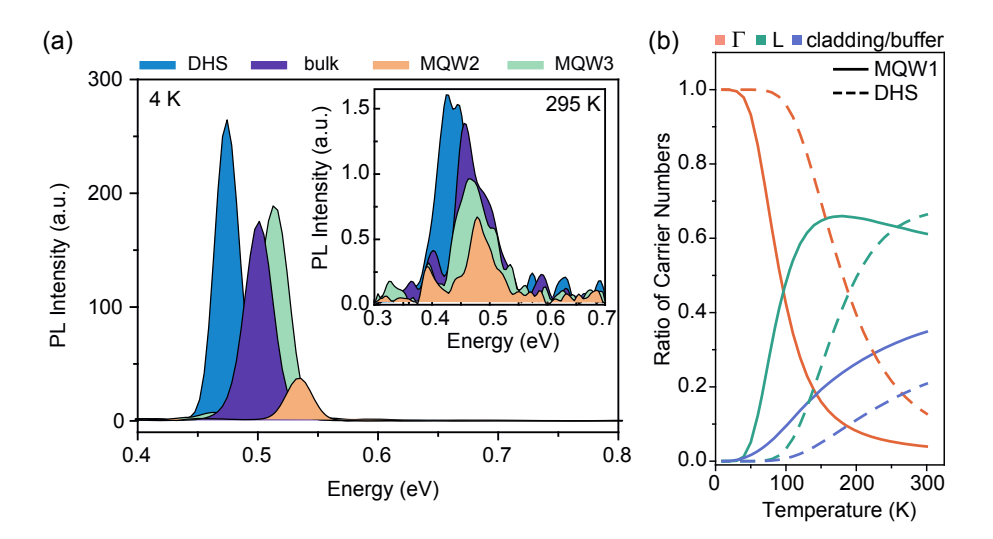


Figure A.1. PL measurements of GeSn/SiGeSn heterostructures at room temperature and 4K are shown in (a) comparison of heterostructure PL and $Ge_{0.875}Sn_{0.125}$ bulk. (b) presents a calculation of the ratio of carrier population in the Γ-valley and the total carrier population at Γ and L inside the active layers. Adapted with permission from [6]. Copyright 2018 American Chemical Society.

material in the MQW1 compared to DHS, is due to the lower directness, which is caused by the quantization and the lower Sn concentration in MQW1.

Bibliography

- [1] D. Stange, S. Wirths, N. von den Driesch, G. Mussler, T. Stoica, Z. Ikonic, J. M. Hartmann, S. Mantl, D. Grützmacher, and D. Buca. "Optical Transitions in Direct-Bandgap Ge_{1-x}Sn_x Alloys". In: ACS Photonics 2.11 (Nov. 2015), pp. 1539–1545. DOI: 10.1021/acsphotonics.5b00372.
- [2] D. Stange, N. von den Driesch, D. Rainko, C. Schulte-Braucks, S. Wirths, G. Mussler, A. T. Tiedemann, T. Stoica, J. M. Hartmann, Z. Ikonic, S. Mantl, D. Grützmacher, and D. Buca. "Study of GeSn based heterostructures: towards optimized group IV MQW LEDs". In: Optics Express 24.2 (Jan. 2016), p. 1358. DOI: 10.1364/0E.24.001358.
- [3] D. Stange, S. Wirths, R. Geiger, C. Schulte-Braucks, B. Marzban, N. von den Driesch, G. Mussler, T. Zabel, T. Stoica, J.-M. Hartmann, S. Mantl, Z. Ikonic, D. Grützmacher, H. Sigg, J. Witzens, and D. Buca. "Optically Pumped GeSn Microdisk Lasers on Si". In: ACS Photonics 3.7 (July 2016), pp. 1279–1285. DOI: 10.1021/acsphotonics.6b00258.
- [4] D. Stange, C. Schulte-Braucks, N. von den Driesch, S. Wirths, G. Mussler, S. Lenk, T. Stoica, S. Mantl, D. Grützmacher, D. Buca, R. Geiger, T. Zabel, H. Sigg, J.-M. Hartmann, and Z. Ikonic. "High Sn-Content GeSn Light Emitters for Silicon Photonics". In: Future Trends in Microelectronics- Journey into the unknown. Ed. by S. Luryi, J. Xu, and A. Zaslavsky. Wiley, 2016. Chap. 2.6, pp. 181–191.
- [5] D. Stange, N. von den Driesch, D. Rainko, S. Roesgaard, I. Povstugar, J.-M. Hartmann, T. Stoica, Z. Ikonic, S. Mantl, D. Grützmacher, and D. Buca.

- "Short-wave infrared LEDs from GeSn/SiGeSn multiple quantum wells". In: *Optica* 4.2 (Feb. 2017), p. 185. DOI: 10.1364/OPTICA.4.000185.
- [6] D. Stange, N. von den Driesch, T. Zabel, F. Armand-Pilon, D. Rainko, B. Marzban, P. Zaumseil, J.-M. Hartmann, Z. Ikonic, G. Capellini, S. Mantl, H. Sigg, J. Witzens, D. Grützmacher, and D. Buca. "GeSn/SiGeSn Heterostructure and Multi Quantum Well Lasers". In: ACS Photonics 5.11 (Nov. 2018), pp. 4628–4636. DOI: 10.1021/acsphotonics.8b01116.
- [7] N. von den Driesch, D. Stange, S. Wirths, D. Rainko, G. Mussler, T. Stoica, Z. Ikonić, J.-M. Hartmann, D. Grützmacher, S. Mantl, and D. Buca. "Direct bandgap GeSn light-emitting diodes for short-wave infrared applications grown on Si". In: SPIE Photonics West. Ed. by G. T. Reed and A. P. Knights. Vol. 9752. Mar. 2016, p. 97520C. DOI: 10.1117/12.2211641.
- [8] N. von den Driesch, D. Stange, S. Wirths, D. Rainko, I. Povstugar, A. Savenko, U. Breuer, R. Geiger, H. Sigg, Z. Ikonic, J.-M. Hartmann, D. Grützmacher, S. Mantl, and D. Buca. "SiGeSn Ternaries for Efficient Group IV Heterostructure Light Emitters". In: Small 13.16 (Apr. 2017), p. 1603321. DOI: 10.1002/smll.201603321.
- [9] N. von den Driesch, D. Stange, D. Rainko, I. Povstugar, P. Zaumseil, G. Capellini, T. Schröder, T. Denneulin, Z. Ikonic, J.-M. Hartmann, H. Sigg, S. Mantl, D. Grützmacher, and D. Buca. "Advanced GeSn/SiGeSn Group IV Heterostructure Lasers". In: Advanced Science 5.6 (June 2018), p. 1700955. DOI: 10.1002/advs.201700955.
- [10] C. Schulte-Braucks, D. Stange, N. von den Driesch, S. Blaeser, Z. Ikonic, J. M. Hartmann, S. Mantl, and D. Buca. "Negative differential resistance in direct band-gap GeSn p-i-n structures". In: Applied Physics Letters 107.4 (July 2015), p. 042101. DOI: 10.1063/1.4927622.
- [11] D. Stange, N. von den Driesch, D. Rainko, T. Zabel, B. Marzban, Z. Ikonic, P. Zaumseil, G. Capellini, S. Manti, J. Witzens, H. Sigg, D. Grützmacher, and D. Buca. "Quantum confinement effects in GeSn/SiGeSn heterostructure lasers". In: 2017 IEEE International Electron Devices Meeting (IEDM). IEEE, Dec. 2017, pp. 24.2.1–24.2.4. DOI: 10.1109/IEDM.2017.8268451.

- [12] T. H. Maiman. "Stimulated Optical Radiation in Ruby". In: Nature 187.4736(Aug. 1960), pp. 493–494. DOI: 10.1038/187493a0.
- [13] T. H. Maiman. "Stimulated Optical Emission in Fluorescent Solids. I. The-oretical Considerations". In: *Physical Review* 123.4 (Aug. 1961), pp. 1145–1150. DOI: 10.1103/PhysRev.123.1145. arXiv: arXiv:1011.1669v3.
- [14] J. Hecht. "A short history of laser development". In: Applied Optics 49.25 (Sept. 2010), F99. DOI: 10.1364/AO.49.000F99.
- [15] M. Chalmers. "World's smallest laser unveiled". In: *Nature* News (2009). DOI: 10.1038/news.2009.823.
- [16] M. A. Noginov, G. Zhu, A. M. Belgrave, R. Bakker, V. M. Shalaev, E. E. Narimanov, S. Stout, E. Herz, T. Suteewong, and U. Wiesner. "Demonstration of a spaser-based nanolaser". In: *Nature* 460.7259 (Aug. 2009), pp. 1110–1112. DOI: 10.1038/nature08318.
- [17] R. Dupuis. "An introduction to the development of the semiconductor laser". In: *IEEE Journal of Quantum Electronics* 23.6 (June 1987), pp. 651–657. DOI: 10.1109/JQE.1987.1073450.
- [18] T. M. Quist, R. H. Rediker, R. J. Keyes, W. E. Krag, B. Lax, A. L. McWhorter, and H. J. Zeigler. "Semiconductor MASER of GaAs". In: Applied Physics Letters 1.4 (Dec. 1962), pp. 91–92. DOI: 10.1063/1.1753710.
- [19] M. I. Nathan, W. P. Dumke, G. Burns, F. H. Dill, and G. Lasher. "Stimulated Emission Of Radiation From GaAs p-n Junctions". In: Applied Physics Letters 1.3 (Nov. 1962), pp. 62–64. DOI: 10.1063/1.1777371.
- [20] R. N. Hall, G. E. Fenner, J. D. Kingsley, T. J. Soltys, and R. O. Carlson. "Coherent Light Emission From GaAs Junctions". In: *Physical Review Letters* 9.9 (Nov. 1962), pp. 366–368. DOI: 10.1103/PhysRevLett.9.366.
- [21] N. Holonyak and S. F. Bevacqua. "Coherent (Visible) Light Emission From $Ga(As_{1-x}P_x)$ Junctions". In: *Applied Physics Letters* 1.4 (Dec. 1962), pp. 82–83. DOI: 10.1063/1.1753706.

- [22] A. Sobiesierski and P. Smowton. "Quantum-Dot Lasers: Physics and Applications". In: Comprehensive Semiconductor Science and Technology. Elsevier, 2011, pp. 353–384. DOI: 10.1016/B978-0-44-453153-7.00034-1.
- [23] A. Lally, S. Bagchi, M. A. Barborak, D. W. Buchanan, J. Chu-Carroll, D. A. Ferrucci, M. R. Glass, A. Kalyanpur, E. T. Mueller, J. W. Murdock, S. Patwardhan, and J. M. Prager. "WatsonPaths: Scenario-Based Question Answering and Inference over Unstructured Information". In: AI Magazine 38.2 (July 2017), p. 59. DOI: 10.1609/aimag.v38i2.2715.
- [24] D. Silver, J. Schrittwieser, K. Simonyan, I. Antonoglou, A. Huang, A. Guez, T. Hubert, L. Baker, M. Lai, A. Bolton, Y. Chen, T. Lillicrap, F. Hui, L. Sifre, G. van den Driessche, T. Graepel, and D. Hassabis. "Mastering the game of Go without human knowledge". In: *Nature* 550.7676 (Oct. 2017), pp. 354–359. DOI: 10.1038/nature24270.
- [25] Cisco. "Cisco Visual Networking Index: Forecast and Methodology, 2016-2021". In: Forecast and Methodology (2017), p. 22. DOI: 1465272001663118. arXiv: 1454457600809267.
- [26] A. F. Benner, M. Ignatowski, J. A. Kash, D. M. Kuchta, and M. B. Ritter. "Exploitation of optical interconnects in future server architectures". In: *IBM Journal of Research and Development* 49.4.5 (July 2005), pp. 755–775. DOI: 10.1147/rd.494.0755.
- [27] D. Miller. "Rationale and challenges for optical interconnects to electronic chips". In: *Proceedings of the IEEE* 88.6 (June 2000), pp. 728–749. DOI: 10.1109/5.867687.
- [28] S. Rumley, M. Bahadori, R. Polster, S. D. Hammond, D. M. Calhoun, K. Wen, A. Rodrigues, and K. Bergman. "Optical interconnects for extreme scale computing systems". In: *Parallel Computing* 64 (May 2017), pp. 65–80. DOI: 10.1016/j.parco.2017.02.001.
- [29] G. Chen, H. Chen, M. Haurylau, N. Nelson, D. Albonesi, P. Fauchet, and E. Friedman. "On-Chip Copper-Based vs. Optical Interconnects: Delay Uncertainty, Latency, Power, and Bandwidth Density Comparative Predictions".

- In: 2006 International Interconnect Technology Conference. IEEE, 2006, pp. 39–41. DOI: 10.1109/IITC.2006.1648640.
- [30] A. Boletti, D. Giacomuzzi, G. Parladori, P. Boffi, M. Ferrario, and M. Martinelli. "Performance comparison between electrical copper-based and optical fiber-based backplanes". In: *Optics Express* 21.16 (Aug. 2013), p. 19202. DOI: 10.1364/0E.21.019202.
- [31] D. Thomson, A. Zilkie, J. E. Bowers, T. Komljenovic, G. T. Reed, L. Vivien, D. Marris-Morini, E. Cassan, L. Virot, J.-M. Fédéli, J.-M. Hartmann, J. H. Schmid, D.-X. Xu, F. Boeuf, P. O'Brien, G. Z. Mashanovich, and M. Nedeljkovic. "Roadmap on silicon photonics". In: *Journal of Optics* 18.7 (July 2016), p. 073003. DOI: 10.1088/2040-8978/18/7/073003.
- [32] T. Hu, B. Dong, X. Luo, T.-Y. Liow, J. Song, C. Lee, and G.-Q. Lo. "Silicon photonic platforms for mid-infrared applications (Invited)". In: *Photonics Research* 5.5 (Oct. 2017), p. 417. DOI: 10.1364/PRJ.5.000417.
- [33] T. Spuesens, D. Van Thourhout, P. Rojo-Romeo, P. Regreny, and J.-M. Fedeli. "CW operation of III-V microdisk lasers on SOI fabricated in a 200 mm CMOS pilot line". In: 8th IEEE International Conference on Group IV Photonics. IEEE, Sept. 2011, pp. 199–201. DOI: 10.1109/GROUP4.2011.6053762.
- [34] G. Roelkens, A. Abassi, P. Cardile, U. Dave, A. D. Groote, Y. D. Koninck, X. Fu, A. Gassenq, N. Hattasan, Q. Huang, S. Kumari, S. Keyvaninia, B. Kuyken, L. Li, P. Mechet, M. Muneeb, D. Sanchez, H. Shao, T. Spuesens, A. Z. Subramanian, S. Uvin, M. Tassaert, K. V. Gasse, J. Verbist, R. Wang, Z. Wang, J. Zhang, J. V. Campenhout, X. Yin, J. Bauwelinck, G. Morthier, R. Baets, and D. V. Thourhout. "III-V-on-Silicon Photonic Devices for Optical Communication and Sensing". In: *Photonics* 2.3 (2015), pp. 969–1004. DOI: 10.3390/photonics2030969.
- [35] G. Crosnier, D. Sanchez, S. Bouchoule, P. Monnier, G. Beaudoin, I. Sagnes, R. Raj, and F. Raineri. "Hybrid indium phosphide-on-silicon nanolaser diode". In: *Nature Photonics* 11.5 (2017), pp. 297–300. DOI: 10.1038/nphoton. 2017.56.

- [36] H. Guan, A. Novack, T. Galfsky, Y. Ma, S. Fathololoumi, A. Horth, T. N. Huynh, J. Roman, R. Shi, M. Caverley, Y. Liu, T. Baehr-Jones, K. Bergman, and M. Hochberg. "Widely-tunable, narrow-linewidth III-V/silicon hybrid external-cavity laser for coherent communication". In: Optics Express 26.7 (2018), p. 7920. DOI: 10.1364/0E.26.007920.
- [37] S. Chen, W. Li, J. Wu, Q. Jiang, M. Tang, S. Shutts, S. N. Elliott, A. Sobiesierski, A. J. Seeds, I. Ross, P. M. Smowton, and H. Liu. "Electrically pumped continuous-wave III-V quantum dot lasers on silicon". In: *Nature Photonics* 10.5 (2016), pp. 307–311. DOI: 10.1038/nphoton.2016.21.
- [38] T. Stettner, T. Kostenbader, D. Ruhstorfer, J. Bissinger, H. Riedl, M. Kaniber, G. Koblmüller, and J. J. Finley. "Direct Coupling of Coherent Emission from Site-Selectively Grown III-V Nanowire Lasers into Proximal Silicon Waveguides". In: *ACS Photonics* 4.10 (Oct. 2017), pp. 2537–2543. DOI: 10.1021/acsphotonics.7b00805.
- [39] P. Chaisakul, D. Marris-Morini, J. Frigerio, D. Chrastina, M.-S. Rouifed, S. Cecchi, P. Crozat, G. Isella, and L. Vivien. "Integrated germanium optical interconnects on silicon substrates". In: *Nature Photonics* 8.6 (June 2014), pp. 482–488. DOI: 10.1038/nphoton.2014.73.
- [40] C. Sun, M. T. Wade, Y. Lee, J. S. Orcutt, L. Alloatti, M. S. Georgas, A. S. Waterman, J. M. Shainline, R. R. Avizienis, S. Lin, B. R. Moss, R. Kumar, F. Pavanello, A. H. Atabaki, H. M. Cook, A. J. Ou, J. C. Leu, Y.-h. Chen, K. Asanović, R. J. Ram, M. A. Popović, and V. M. Stojanović. "Single-chip microprocessor that communicates directly using light". In: *Nature* 528.7583 (Dec. 2015), pp. 534–538. DOI: 10.1038/nature16454.
- [41] Z. Zhou, B. Yin, and J. Michel. "On-chip light sources for silicon photonics". In: *Light: Science & Applications* 4.11 (Nov. 2015), e358–e358. DOI: 10.1038/lsa.2015.131.
- [42] J. R. Jain, A. Hryciw, T. M. Baer, D. A. B. Miller, M. L. Brongersma, and R. T. Howe. "A micromachining-based technology for enhancing germanium light emission via tensile strain". In: *Nature Photonics* 6.6 (May 2012), pp. 398–405. DOI: 10.1038/nphoton.2012.111.

- [43] R. Geiger, T. Zabel, and H. Sigg. "Group IV Direct Band Gap Photonics: Methods, Challenges, and Opportunities". In: *Frontiers in Materials* 2.July (July 2015). DOI: 10.3389/fmats.2015.00052.
- [44] A. Elbaz, M. El Kurdi, A. Aassime, S. Sauvage, X. Checoury, I. Sagnes, C. Baudot, F. Boeuf, and P. Boucaud. "Germanium microlasers on metallic pedestals". In: APL Photonics 3.10 (Oct. 2018), p. 106102. DOI: 10.1063/1. 5025705.
- [45] R. Soref. "The Past, Present, and Future of Silicon Photonics". In: IEEE Journal of Selected Topics in Quantum Electronics 12.6 (Nov. 2006), pp. 1678– 1687. DOI: 10.1109/JSTQE.2006.883151.
- [46] S. Wirths, R. Geiger, N. von den Driesch, G. Mussler, T. Stoica, S. Mantl, Z. Ikonic, M. Luysberg, S. Chiussi, J. M. Hartmann, H. Sigg, J. Faist, D. Buca, and D. Grützmacher. "Lasing in direct-bandgap GeSn alloy grown on Si". In: Nature Photonics 9.2 (Jan. 2015), pp. 88–92. DOI: 10.1038/nphoton.2014. 321.
- [47] S. Gupta, R. Chen, B. Magyari-Kope, H. Lin, Bin Yang, A. Nainani, Y. Nishi, J. S. Harris, and K. C. Saraswat. "GeSn technology: Extending the Ge electronics roadmap". In: 2011 International Electron Devices Meeting. IEEE, Dec. 2011, pp. 16.6.1–16.6.4. DOI: 10.1109/IEDM.2011.6131568.
- [48] R. Pandey, C. Schulte-Braucks, R. N. Sajjad, M. Barth, R. K. Ghosh, B. Grisafe, P. Sharma, N. von den Driesch, A. Vohra, B. Rayner, R. Loo, S. Mantl, D. Buca, C.-C. Yeh, C.-H. Wu, W. Tsai, D. Antoniadis, and S. Datta. "Performance benchmarking of p-type In_{0.65}Ga_{0.35}As/GaAs_{0.4}Sb_{0.6} and Ge/Ge_{0.93}Sn_{0.07} Hetero-junction Tunnel FETs". In: 2016 IEEE International Electron Devices Meeting (IEDM). IEEE, Dec. 2016, pp. 19.6.1–19.6.4. DOI: 10.1109/IEDM. 2016.7838455.
- [49] S. Al-Kabi, S. A. Ghetmiri, J. Margetis, T. Pham, Y. Zhou, W. Dou, B. Collier, R. Quinde, W. Du, A. Mosleh, J. Liu, G. Sun, R. A. Soref, J. Tolle, B. Li, M. Mortazavi, H. A. Naseem, and S.-q. Yu. "An optically pumped 2.5 μm GeSn laser on Si operating at 110 K". In: Applied Physics Letters 109.17 (Oct. 2016), p. 171105. DOI: 10.1063/1.4966141.

- [50] V. Reboud, A. Gassenq, N. Pauc, J. Aubin, L. Milord, Q. M. Thai, M. Bertrand, K. Guilloy, D. Rouchon, J. Rothman, T. Zabel, F. Armand Pilon, H. Sigg, A. Chelnokov, J. M. Hartmann, and V. Calvo. "Optically pumped GeSn micro-disks with 16% Sn lasing at 3.1 μm up to 180 K". In: Applied Physics Letters 111.9 (Aug. 2017), p. 092101. DOI: 10.1063/1.5000353.
- [51] J. Juan-Colás, A. Parkin, K. E. Dunn, M. G. Scullion, T. F. Krauss, and S. D. Johnson. "The electrophotonic silicon biosensor". In: *Nature Communications* 7 (Sept. 2016), p. 12769. DOI: 10.1038/ncomms12769.
- [52] M. Sieger and B. Mizaikoff. "Toward On-Chip Mid-Infrared Sensors". In: Analytical Chemistry 88.11 (June 2016), pp. 5562-5573. DOI: 10.1021/acs. analchem.5b04143.
- [53] R. Wang, A. Vasiliev, M. Muneeb, A. Malik, S. Sprengel, G. Boehm, M.-C. Amann, I. Šimonytė, A. Vizbaras, K. Vizbaras, R. Baets, and G. Roelkens. "III-V-on-Silicon Photonic Integrated Circuits for Spectroscopic Sensing in the 2-4 μm Wavelength Range". In: Sensors 17.8 (2017), p. 1788. DOI: 10.3390/s17081788.
- [54] R. Geiger. "Direct Band Gap Germanium for Si-compatible Lasing". PhD thesis. ETH Zurich, 2016. DOI: 10.3929/ethz-a-010645406.
- [55] J. J. Coleman. "The development of the semiconductor laser diode after the first demonstration in 1962". In: Semiconductor Science and Technology 27.9 (Sept. 2012), p. 090207. DOI: 10.1088/0268-1242/27/9/090207.
- [56] C. Goodman. "Direct-gap group IV semiconductors based on tin". In: IEEE Proceedings I Solid State and Electron Devices 129.5 (1982), pp. 189–192. DOI: 10.1049/ip-i-1.1983.0009.
- [57] J. J. Ackert, D. J. Thomson, L. Shen, A. C. Peacock, P. E. Jessop, G. T. Reed, G. Z. Mashanovich, and A. P. Knights. "High-speed detection at two micrometres with monolithic silicon photodiodes". In: *Nature Photonics* 9.6 (May 2015), pp. 393–396. DOI: 10.1038/nphoton.2015.81.
- [58] R. Soref, D. Buca, and S.-Q. Yu. "Group IV Photonics: Driving Integrated Optoelectronics". In: Optics and Photonics News 27.1 (Jan. 2016), p. 32. DOI: 10.1364/OPN.27.1.000032.

- [59] J. R. Chelikowsky and M. L. Cohen. "Nonlocal pseudopotential calculations for the electronic structure of eleven diamond and zinc-blende semiconductors". In: *Physical Review B* 14.2 (July 1976), pp. 556–582. DOI: 10.1103/ PhysRevB.14.556.
- [60] R. W. Olesinski and G. J. Abbaschian. "The Ge-Sn (Germanium-Tin) system". In: Bulletin of Alloy Phase Diagrams 5.3 (June 1984), pp. 265–271. DOI: 10.1007/BF02868550.
- [61] P. Moontragoon, Z. Ikonić, and P. Harrison. "Band structure calculations of Si-Ge-Sn alloys: achieving direct band gap materials". In: Semiconductor Science and Technology 22.7 (July 2007), pp. 742–748. DOI: 10.1088/0268– 1242/22/7/012.
- [62] P. Moontragoon, R. A. Soref, and Z. Ikonić. "The direct and indirect bandgaps of unstrained $Si_xGe_{1-x-y}Sn_y$ and their photonic device applications". In: Journal of Applied Physics 112.7 (2012), p. 073106. DOI: 10.1063/1.4757414.
- [63] N. von den Driesch. "Epitaxy of group IV Si-Ge-Sn alloys for advanced heterostructure light emtitters". PhD thesis. RWTH Aachen University, 2018, p. 149. DOI: 10.18154/RWTH-2018-221225.
- [64] M.-Y. Ryu, T. R. Harris, Y. K. Yeo, R. T. Beeler, and J. Kouvetakis. "Temperature-dependent photoluminescence of Ge/Si and Ge_{1-y}Sn_y/Si, indicating possible indirect-to-direct bandgap transition at lower Sn content". In: Applied Physics Letters 102.17 (2013), p. 171908. DOI: 10.1063/1.4803927.
- [65] N. von den Driesch, D. Stange, S. Wirths, G. Mussler, B. Holländer, Z. Ikonic, J. M. Hartmann, T. Stoica, S. Mantl, D. Grützmacher, and D. Buca. "Direct Bandgap Group IV Epitaxy on Si for Laser Applications". In: *Chemistry of Materials* 27.13 (June 2015), pp. 4693–4702. DOI: 10.1021/acs.chemmater. 5b01327.
- [66] F. Gencarelli, B. Vincent, J. Demeulemeester, A. Vantomme, A. Moussa, A. Franquet, A. Kumar, H. Bender, J. Meersschaut, W. Vandervorst, R. Loo, M. Caymax, K. Temst, and M. Heyns. "Crystalline Properties and Strain Relaxation Mechanism of CVD Grown GeSn". In: ECS Journal of Solid

- State Science and Technology 2.4 (Jan. 2013), P134-P137. DOI: 10.1149/2.011304jss.
- [67] D. Bimberg, R. Blachnik, M. Cardona, P. J. Dean, T. Grave, G. Harbeke, K. Hübner, U. Kaufmann, W. Kress, O. Madelung, W. von Münch, U. Rössler, J. Schneider, M. Schulz, and M. S. Skolnick. *Physics of Group IV Elements and III-V Compounds*. Ed. by O. Madelung. 1st ed. Springer-Verlag, New York, 1982.
- [68] G.-E. Chang, S.-W. Chang, and S. L. Chuang. "Strain-Balanced $\text{Ge}_z \text{Sn}_{1-z}$ - $\text{Si}_x \text{Ge}_y \text{Sn}_{1-x-y}$ Multiple-Quantum-Well Lasers". In: *IEEE Journal of Quantum Electronics* 46.12 (Dec. 2010), pp. 1813–1820. DOI: 10.1109/JQE.2010. 2059000.
- [69] G. Sun, R. A. Soref, and H. H. Cheng. "Design of an electrically pumped SiGeSn/GeSn/SiGeSn double-heterostructure midinfrared laser". In: *Journal of Applied Physics* 108.3 (2010), p. 033107. DOI: 10.1063/1.3467766.
- [70] G.-E. Chang, S.-W. Chang, and S. L. Chuang. "Theory for n-type doped, tensile-strained $\text{Ge-Si}_x\text{Ge}_y\text{Sn}_{1-x-y}$ quantum-well lasers at telecom wavelength". In: *Optics Express* 17.14 (July 2009), p. 11246. DOI: 10.1364/0E.17.011246.
- [71] V. R. D'Costa, Y.-Y. Fang, J. Tolle, J. Kouvetakis, and J. Menéndez. "Tunable Optical Gap at a Fixed Lattice Constant in Group-IV Semiconductor Alloys". In: *Physical Review Letters* 102.10 (Mar. 2009), p. 107403. DOI: 10.1103/PhysRevLett.102.107403.
- [72] T. Wendav, I. A. Fischer, M. Montanari, M. H. Zoellner, W. Klesse, G. Capellini, N. von den Driesch, M. Oehme, D. Buca, K. Busch, and J. Schulze. "Compositional dependence of the band-gap of $\mathrm{Ge}_{1-x-y}\mathrm{Si}_x\mathrm{Sn}_y$ alloys". In: Applied Physics Letters 108.24 (June 2016), p. 242104. DOI: 10.1063/1.4953784.
- [73] H. Kroemer. "A proposed class of hetero-junction injection lasers". In: *Proceedings of the IEEE* 51.12 (Dec. 1963), pp. 1782–1783. DOI: 10.1109/PROC. 1963.2706.

- [74] Z. Alferov. "Double heterostructure lasers: early days and future perspectives". In: *IEEE Journal of Selected Topics in Quantum Electronics* 6.6 (Nov. 2000), pp. 832–840. DOI: 10.1109/2944.902131.
- [75] M. Grundmann. *The Physics of Semiconductors*. Springer-Verlag Berlin Heidelberg, 2006, p. 643.
- [76] E. F. Schubert. *Light-Emitting Diodes*. second edi. Cambridge University press, 2006.
- [77] T. B. Bahder. "Eight-band $k \cdot p$ model of strained zinc-blende crystals". In: *Physical Review B* 41.17 (June 1990), pp. 11992–12001. DOI: 10.1103/PhysRevB.41.11992.
- [78] T. B. Bahder. "Erratum: Eight-band $k \cdot p$ model of strained zinc-blende crystals [Phys. Rev. B 41, 11 992 (1990)]". In: *Physical Review B* 46.15 (Oct. 1992), pp. 9913–9913. DOI: 10.1103/PhysRevB.46.9913.
- [79] P. Moontragoon, N. Vukmirović, Z. Ikonić, and P. Harrison. "Electronic structure and optical properties of Sn and SnGe quantum dots". In: *Journal of Applied Physics* 103.10 (2008), p. 103712. DOI: 10.1063/1.2932169.
- [80] G. P. Agrawal and N. K. Dutta. Semiconductor Lasers. 1993.
- [81] W. Shockley and W. T. Read. "Statistics of the Recombinations of Holes and Electrons". In: *Physical Review* 87.5 (1952), pp. 835–842.
- [82] G. Sun, R. A. Soref, and H. H. Cheng. "Design of a Si-based lattice-matched room-temperature GeSn/GeSiSn multi-quantum-well mid-infrared laser diode" In: Optics Express 18.19 (Sept. 2010), p. 19957. DOI: 10.1364/0E.18.019957.
- [83] C. L. Senaratne, J. D. Gallagher, T. Aoki, J. Kouvetakis, and J. Menendez. "Advances in Light Emission from Group-IV Alloys via Lattice Engineering and n-Type Doping Based on Custom-Designed Chemistries". In: *Chemistry* of Materials 26.20 (Oct. 2014), pp. 6033–6041. DOI: 10.1021/cm502988y.

- [84] S. A. Ghetmiri, W. Du, J. Margetis, A. Mosleh, L. Cousar, B. R. Conley, L. Domulevicz, A. Nazzal, G. Sun, R. A. Soref, J. Tolle, B. Li, H. A. Naseem, and S.-Q. Yu. "Direct-bandgap GeSn grown on silicon with 2230 nm photoluminescence". In: Applied Physics Letters 105.15 (Oct. 2014), p. 151109. DOI: 10.1063/1.4898597.
- T. R. Harris, M.-Y. Ryu, Y. K. Yeo, B. Wang, C. L. Senaratne, and J. Kouvetakis. "Direct bandgap cross-over point of $Ge_{1-y}Sn_y$ grown on Si estimated through temperature-dependent photoluminescence studies". In: *Journal of Applied Physics* 120.8 (Aug. 2016), p. 085706. DOI: 10.1063/1.4961464.
- [86] F. Pezzoli, A. Giorgioni, D. Patchett, and M. Myronov. "Temperature-Dependent Photoluminescence Characteristics of GeSn Epitaxial Layers". In: ACS Photonics 3.11 (2016), pp. 2004–2009. DOI: 10.1021/acsphotonics.6b00438.
- [87] W. Du, S. A. Ghetmiri, J. Margetis, S. Al-Kabi, Y. Zhou, J. Liu, G. Sun, R. A. Soref, J. Tolle, B. Li, M. Mortazavi, and S.-Q. Yu. "Investigation of optical transitions in a SiGeSn/GeSn/SiGeSn single quantum well structure". In: *Journal of Applied Physics* 122.12 (Sept. 2017), p. 123102. DOI: 10.1063/1.4986341.
- [88] S. A. Ghetmiri, Y. Zhou, J. Margetis, S. Al-Kabi, W. Dou, A. Mosleh, W. Du, A. Kuchuk, J. Liu, G. Sun, R. A. Soref, J. Tolle, H. A. Naseem, B. Li, M. Mortazavi, and S.-Q. Yu. "Study of a SiGeSn/GeSn/SiGeSn structure toward direct bandgap type-I quantum well for all group-IV optoelectronics". In: Optics Letters 42.3 (Feb. 2017), p. 387. DOI: 10.1364/OL.42.000387.
- [89] J. Aubin, J. Hartmann, A. Gassenq, L. Milord, N. Pauc, V. Reboud, and V. Calvo. "Impact of thickness on the structural properties of high tin content GeSn layers". In: *Journal of Crystal Growth* 473 (Sept. 2017), pp. 20–27. DOI: 10.1016/j.jcrysgro.2017.05.006.
- [90] S. Wirths, R. Geiger, N. von den Driesch, G. Mussler, T. Stoica, S. Mantl, Z. Ikonic, M. Luysberg, S. Chiussi, J. M. Hartmann, H. Sigg, J. Faist, D. Buca, and D. Grützmacher. "Lasing in direct-bandgap GeSn alloy grown on Si supplementary". In: *Nature Photonics* 9.2 (Jan. 2015), pp. 88–92. DOI: 10.1038/nphoton.2014.321.

- [91] C.-L. Hsiao, H.-C. Hsu, L.-C. Chen, C.-T. Wu, C.-W. Chen, M. Chen, L.-W. Tu, and K.-H. Chen. "Photoluminescence spectroscopy of nearly defect-free InN microcrystals exhibiting nondegenerate semiconductor behaviors". In: Applied Physics Letters 91.18 (2007), p. 181912. DOI: 10.1063/1.2804568.
- [92] Y. Varshni. "Temperature dependence of the energy gap in semiconductors".
 In: *Physica* 34.1 (Jan. 1967), pp. 149–154. DOI: 10.1016/0031-8914(67)
 90062-6.
- [93] S. Gupta, E. Simoen, H. Vrielinck, C. Merckling, B. Vincent, F. Gencarelli, R. Loo, and M. Heyns. "Identification of Deep Levels Associated with Extended and Point Defects in GeSn Epitaxial Layers Using DLTs". In: ECS Transactions 53.1 (2013), pp. 251–258. DOI: 10.1149/05301.0251ecst.
- [94] K. L. Teo, J. S. Colton, P. Y. Yu, E. R. Weber, M. F. Li, W. Liu, K. Uchida, H. Tokunaga, N. Akutsu, and K. Matsumoto. "An analysis of temperature dependent photoluminescence line shapes in InGaN". In: *Applied Physics Letters* 73.12 (Sept. 1998), pp. 1697–1699. DOI: 10.1063/1.122249.
- I. Mártil, E. Redondo, and A. Ojeda. "Influence of defects on the electrical and optical characteristics of blue light-emitting diodes based on III-V nitrides".
 In: Journal of Applied Physics 81.5 (Mar. 1997), pp. 2442-2444. DOI: 10. 1063/1.364294.
- [96] X. Cao, E. Stokes, P. Sandvik, S. LeBoeuf, J. Kretchmer, and D. Walker. "Diffusion and tunneling currents in GaN/InGaN multiple quantum well light-emitting diodes". In: *IEEE Electron Device Letters* 23.9 (Sept. 2002), pp. 535–537. DOI: 10.1109/LED.2002.802601.
- [97] H. Wang, Z. Ji, S. Qu, G. Wang, Y. Jiang, B. Liu, X. Xu, and H. Mino. "Influence of excitation power and temperature on photoluminescence in In-GaN/GaN multiple quantum wells". In: *Optics Express* 20.4 (Feb. 2012), p. 3932. DOI: 10.1364/0E.20.003932.
- [98] T. Schmidt, K. Lischka, and W. Zulehner. "Excitation-power dependence of the near-band-edge photoluminescence of semiconductors". In: *Physical Review B* 45.16 (Apr. 1992), pp. 8989–8994. DOI: 10.1103/PhysRevB.45. 8989.

- [99] C.-Y. Lin, C.-H. Huang, S.-H. Huang, C.-C. Chang, C. W. Liu, Y.-C. Huang, H. Chung, and C.-P. Chang. "Photoluminescence and electroluminescence from Ge/strained GeSn/Ge quantum wells". In: *Applied Physics Letters* 109.9 (Aug. 2016), p. 091103. DOI: 10.1063/1.4961939.
- [100] S. Mokkapati and C. Jagadish. "III-V compound SC for optoelectronic devices". In: *Materials Today* 12.4 (Apr. 2009), pp. 22–32. DOI: 10.1016/S1369-7021(09)70110-5.
- [101] R. W. Millar, D. C. S. Dumas, K. F. Gallacher, P. Jahandar, C. MacGregor, M. Myronov, and D. J. Paul. "Mid-infrared light emission $>3~\mu m$ wavelength from tensile strained GeSn microdisks". In: *Optics Express* 25.21 (Oct. 2017), p. 25374. DOI: 10.1364/0E.25.025374.
- [102] D. Stange, N. von den Driesch, T. Zabel, F. Armand-Pilon, D. Rainko, B. Marzban, P. Zaumseil, J.-M. Hartmann, Z. Ikonic, G. Capellini, S. Mantl, H. Sigg, J. Witzens, D. Grützmacher, and D. Buca. "SI: GeSn/SiGeSn Heterostructure and Multi Quantum Well Lasers". In: accepted by ACS Photonics (2018).
- [103] M. Oehme, J. Werner, M. Gollhofer, M. Schmid, M. Kaschel, E. Kasper, and J. Schulze. "Room-Temperature Electroluminescence From GeSn Light-Emitting Pin Diodes on Si". In: *IEEE Photonics Technology Letters* 23.23 (Dec. 2011), pp. 1751–1753. DOI: 10.1109/LPT.2011.2169052.
- [104] J. D. Gallagher, C. L. Senaratne, P. Sims, T. Aoki, J. Menéndez, and J. Kouvetakis. "Electroluminescence from GeSn heterostructure pin diodes at the indirect to direct transition". In: Applied Physics Letters 106.9 (Mar. 2015), p. 091103. DOI: 10.1063/1.4913688.
- [105] J. D. Gallagher, C. L. Senaratne, C. Xu, P. Sims, T. Aoki, D. J. Smith, J. Menéndez, and J. Kouvetakis. "Non-radiative recombination in $\mathrm{Ge}_{1-y}\mathrm{Sn}_y$ light emitting diodes: The role of strain relaxation in tuned heterostructure designs". In: *Journal of Applied Physics* 117.24 (June 2015), p. 245704. DOI: 10.1063/1.4923060.

- [106] J. D. Gallagher, C. Xu, C. L. Senaratne, T. Aoki, P. M. Wallace, J. Kouvetakis, and J. Menéndez. " $Ge_{1-x-y}Si_xSn_y$ light emitting diodes on silicon for mid-infrared photonic applications". In: *Journal of Applied Physics* 118.13 (2015), p. 135701. DOI: 10.1063/1.4931770.
- [107] H. H. Tseng, K. Y. Wu, H. Li, V. Mashanov, H. H. Cheng, G. Sun, and R. A. Soref. "Mid-infrared electroluminescence from a Ge/Ge_{0.922}Sn_{0.078}/Ge double heterostructure p-i-n diode on a Si substrate". In: Applied Physics Letters 102.18 (2013), p. 182106. DOI: 10.1063/1.4804675.
- [108] Y. Zhou, W. Dou, W. Du, T. Pham, S. A. Ghetmiri, S. Al-Kabi, A. Mosleh, M. Alher, J. Margetis, J. Tolle, G. Sun, R. Soref, B. Li, M. Mortazavi, H. Naseem, and S.-Q. Yu. "Systematic study of GeSn heterostructure-based light-emitting diodes towards mid-infrared applications". In: *Journal of Applied Physics* 120.2 (July 2016), p. 023102. DOI: 10.1063/1.4958337.
- [109] B. Schwartz, M. Oehme, K. Kostecki, D. Widmann, M. Gollhofer, R. Koerner, S. Bechler, I. A. Fischer, T. Wendav, E. Kasper, J. Schulze, and M. Kittler. "Electroluminescence of GeSn/Ge MQW LEDs on Si substrate". In: Optics Letters 40.13 (July 2015), p. 3209. DOI: 10.1364/0L.40.003209.
- [110] S. Wirths, R. Troitsch, G. Mussler, J.-M. Hartmann, P. Zaumseil, T. Schroeder, S. Mantl, and D. Buca. "Ternary and quaternary Ni(Si)Ge(Sn) contact formation for highly strained Ge p- and n-MOSFETs". In: Semiconductor Science and Technology 30.5 (May 2015), p. 055003. DOI: 10.1088/0268-1242/30/5/055003.
- [111] C. Schulte-Braucks, E. Hofmann, S. Glass, N. von den Driesch, G. Mussler, U. Breuer, J.-M. Hartmann, P. Zaumseil, T. Schröder, Q.-T. Zhao, S. Mantl, and D. Buca. "Schottky barrier tuning via dopant segregation in NiGeSn-GeSn contacts". In: *Journal of Applied Physics* 121.20 (May 2017), p. 205705. DOI: 10.1063/1.4984117.
- [112] C. Schulte-Braucks, S. Glass, E. Hofmann, D. Stange, N. von den Driesch, J. Hartmann, Z. Ikonic, Q. Zhao, D. Buca, and S. Mantl. "Process modules for GeSn nanoelectronics with high Sn-contents". In: *Solid-State Electronics* 128 (Feb. 2017), pp. 54–59. DOI: 10.1016/j.sse.2016.10.024.

- [113] J. Hilibrand and R. D. Gold. "Determination of the Impurity Distribution in Junction Diodes from Capacitance-Voltage Measurements". In: RCA Review 21 (1960), p. 245.
- [114] S. Wirths, D. Stange, M.-A. Pampillón, A. T. Tiedemann, G. Mussler, A. Fox, U. Breuer, B. Baert, E. San Andrés, N. D. Nguyen, J.-M. Hartmann, Z. Ikonic, S. Mantl, and D. Buca. "High- k Gate Stacks on Low Bandgap Tensile Strained Ge and GeSn Alloys for Field-Effect Transistors". In: ACS Applied Materials and Interfaces 7.1 (Jan. 2015), pp. 62–67. DOI: 10.1021/am5075248.
- [115] C. Schulte-Braucks. "Investigation of GeSn as Novel Group IV Semiconductor for Electronic Applications". PhD thesis. RWTH Aachen University, 2017. DOI: 10.18154/RWTH-2018-223259.
- [116] S. M. Sze and K. K. Ng. *Physics Of Semiconductor Devices*. 3rd. Whiley Interscience, 2007.
- [117] C. Schulte-Braucks, N. von den Driesch, S. Glass, A. T. Tiedemann, U. Breuer, A. Besmehn, J.-M. Hartmann, Z. Ikonic, Q. T. Zhao, S. Mantl, and D. Buca. "Low Temperature Deposition of High-k/Metal Gate Stacks on High-Sn Content (Si)GeSn-Alloys". In: ACS Applied Materials and Interfaces 8.20 (May 2016), pp. 13133–13139. DOI: 10.1021/acsami.6b02425.
- [118] L. Esaki. "New Phenomenon in Narrow Germanium p-n Junctions". In: *Physical Review* 109.2 (Jan. 1958), pp. 603–604. DOI: 10.1103/PhysRev.109.603.
- [119] M. Oehme, A. Karmous, M. Sarlija, J. Werner, E. Kasper, and J. Schulze. "Ge quantum dot tunneling diode with room temperature negative differential resistance". In: *Applied Physics Letters* 97.1 (2010), p. 012101. DOI: 10.1063/ 1.3462069.
- [120] M. Stoffel, G. S. Kar, and O. G. Schmidt. "Ge rich Esaki diodes with high peak to valley current ratios". In: *Materials Science and Engineering C* 25.5-8 (2005), pp. 826-829. DOI: 10.1016/j.msec.2005.06.027.

- [121] T. Pham, W. Du, H. Tran, J. Margetis, J. Tolle, G. Sun, R. A. Soref, H. A. Naseem, B. Li, and S.-Q. Yu. "Systematic study of Si-based GeSn photodiodes with 26 μ m detector cutoff for short-wave infrared detection". In: *Optics Express* 24.5 (Mar. 2016), p. 4519. DOI: 10.1364/OE.24.004519.
- [122] T. Stoica, L. Vescan, and M. Goryll. "Electroluminescence of strained SiGe/Si selectively grown above the critical thickness for plastic relaxation". In: *Journal of Applied Physics* 83.6 (Mar. 1998), pp. 3367–3373. DOI: 10.1063/1.367104.
- [123] R. R. Lieten, K. Bustillo, T. Smets, E. Simoen, J. W. Ager, E. E. Haller, and J.-P. Locquet. "Photoluminescence of bulk germanium". In: *Physical Review* B 86.3 (July 2012), p. 035204. DOI: 10.1103/PhysRevB.86.035204.
- [124] P. Lautenschlager, M. Garriga, and M. Cardona. "Temperature dependence of the interband critical-point parameters of InP". In: *Physical Review B* 36.9 (Sept. 1987), pp. 4813–4820. DOI: 10.1103/PhysRevB.36.4813.
- [125] R. Pässler. "Temperature dependence of fundamental band gaps in group IV, III–V, and II–VI materials via a two-oscillator model". In: *Journal of Applied Physics* 89.11 (June 2001), pp. 6235–6240. DOI: 10.1063/1.1369407.
- [126] L. Gupta, S. Rath, S. C. Abbi, and F. C. Jain. "Temperature dependence of the fundamental band gap parameters in cadmium-rich Zn_xCd_{1-x}Se using photoluminescence spectroscopy". In: *Pramana* 61.4 (Oct. 2003), pp. 729– 737. DOI: 10.1007/BF02706122.
- [127] L. Viña, S. Logothetidis, and M. Cardona. "Temperature dependence of the dielectric function of germanium". In: *Physical Review B* 30.4 (Aug. 1984), pp. 1979–1991. DOI: 10.1103/PhysRevB.30.1979.
- [128] P. C. Grant, J. Margetis, Y. Zhou, W. Dou, G. Abernathy, A. Kuchuk, W. Du, B. Li, J. Tolle, J. Liu, G. Sun, R. A. Soref, M. Mortazavi, and S.-Q. Yu. "Direct bandgap type-I GeSn/GeSn quantum well on a GeSn- and Gebuffered Si substrate". In: AIP Advances 8.2 (Feb. 2018), p. 025104. DOI: 10.1063/1.5020035.

- [129] G. Tränkle, H. Leier, A. Forchel, H. Haug, C. Ell, and G. Weimann. "Dimensionality dependence of the band-gap renormalization in two- and three-dimensional electron-hole plasmas in GaAs". In: *Physical Review Letters* 58.4 (Jan. 1987), pp. 419–422. DOI: 10.1103/PhysRevLett.58.419.
- [130] N. Kirstaedter, E. H. Böttcher, D. Bimberg, C. Harder, and H. P. Meier. Granular Nanoelectronics. Ed. by D. K. Ferry, J. R. Barker, and C. Jacoboni. Vol. 251. NATO ASI Series. Boston, MA: Springer US, 1991, pp. 499–502. DOI: 10.1007/978-1-4899-3689-9.
- [131] J. Van Campenhout, P. Rojo Romeo, P. Regreny, C. Seassal, D. Van Thourhout, S. Verstuyft, L. Di Cioccio, J.-M. Fedeli, C. Lagahe, and R. Baets. "Electrically pumped InP-based microdisk lasers integrated with a nanophotonic silicon-on-insulator waveguide circuit". In: Optics Express 15.11 (2007), p. 6744. DOI: 10.1364/0E.15.006744.
- [132] R. Wang, S. Sprengel, G. Boehm, M. Muneeb, R. Baets, M.-C. Amann, and G. Roelkens. "2.3 μm range InP-based type-II quantum well Fabry-Perot lasers heterogeneously integrated on a silicon photonic integrated circuit". In: Optics Express 24.18 (Sept. 2016), p. 21081. DOI: 10.1364/0E.24.021081.
- [133] Z. Wang, A. Abbasi, U. Dave, A. De Groote, S. Kumari, B. Kunert, C. Merckling, M. Pantouvaki, Y. Shi, B. Tian, K. Van Gasse, J. Verbist, R. Wang, W. Xie, J. Zhang, Y. Zhu, J. Bauwelinck, X. Yin, Z. Hens, J. Van Campenhout, B. Kuyken, R. Baets, G. Morthier, D. Van Thourhout, and G. Roelkens. "Novel Light Source Integration Approaches for Silicon Photonics". In: Laser & Photonics Reviews 11.4 (July 2017), p. 1700063. DOI: 10.1002/lpor.201700063.
- [134] Y. Sun, K. Zhou, Q. Sun, J. Liu, M. Feng, Z. Li, Y. Zhou, L. Zhang, D. Li, S. Zhang, M. Ikeda, S. Liu, and H. Yang. "Room-temperature continuous-wave electrically injected InGaN-based laser directly grown on Si". In: *Nature Photonics* 10.9 (Aug. 2016), pp. 595–599. DOI: 10.1038/nphoton.2016.158.
- [135] Y. Wan, D. Jung, J. Norman, C. Shang, I. MacFarlane, Q. Li, M. J. Kennedy, A. C. Gossard, K. M. Lau, and J. E. Bowers. "O-band electrically injected

- quantum dot micro-ring lasers on on-axis (001) GaP/Si and V-groove Si". In: Optics Express 25.22 (Oct. 2017), p. 26853. DOI: 10.1364/0E.25.026853.
- [136] G. N. Malheiros-Silveira, F. Lu, I. Bhattacharya, T.-T. D. Tran, H. Sun, and C. J. Chang-Hasnain. "III-V Compound Semiconductor Nanopillars Monolithically Integrated to Silicon Photonics". In: ACS Photonics 4.5 (2017), pp. 1021–1025. DOI: 10.1021/acsphotonics.6b01035.
- [137] D. Liang, X. Huang, G. Kurczveil, M. Fiorentino, and R. G. Beausoleil. "Integrated finely tunable microring laser on silicon". In: *Nature Photonics* 10.11 (2016), pp. 719–722. DOI: 10.1038/nphoton.2016.163.
- [138] J. Liu, X. Sun, D. Pan, X. Wang, L. C. Kimerling, T. L. Koch, and J. Michel. "Tensile-strained, n-type Ge as a gain medium for monolithic laser integration on Si". In: *Optics Express* 15.18 (2007), p. 11272. DOI: 10.1364/0E.15. 011272.
- [139] R. Geiger, M. J. Suess, R. A. Minamisawa, C. Bonzon, G. Schiefler, J. Frigerio, D. Chrastina, G. Isella, R. Spolenak, J. Faiste, and H. Sigg. "Enhanced light emission from Ge micro bridges uniaxially strained beyond 3%". In: 10th International Conference on Group IV Photonics. Vol. 1. IEEE, Aug. 2013, pp. 93–94. DOI: 10.1109/Group4.2013.6644442.
- [140] R. Millar, K. Gallacher, J. Frigerio, A. Ballabio, A. Bashir, I. MacLaren, G. Isella, and D. J. Paul. "Analysis of Ge micro-cavities with in-plane tensile strains above 2 %". In: Optics Express 24.5 (Mar. 2016), p. 4365. DOI: 10. 1364/0E.24.004365.
- [141] A. Z. Al-Attili, S. Kako, M. K. Husain, F. Y. Gardes, N. Higashitarumizu, S. Iwamoto, Y. Arakawa, Y. Ishikawa, H. Arimoto, K. Oda, T. Ido, and S. Saito. "Whispering Gallery Mode Resonances from Ge Micro-Disks on Suspended Beams". In: Frontiers in Materials 2.May (May 2015), pp. 1–9. DOI: 10.3389/fmats.2015.00043.
- [142] K. Guilloy, N. Pauc, A. Gassenq, Y.-M. Niquet, J.-M. Escalante, I. Duchemin, S. Tardif, G. Osvaldo Dias, D. Rouchon, J. Widiez, J.-M. Hartmann, R. Geiger, T. Zabel, H. Sigg, J. Faist, A. Chelnokov, V. Reboud, and V. Calvo. "Germanium under High Tensile Stress: Nonlinear Dependence of Direct

- Band Gap vs Strain". In: *ACS Photonics* 3.10 (Oct. 2016), pp. 1907–1911. DOI: 10.1021/acsphotonics.6b00429.
- [143] M. El Kurdi, M. Prost, A. Ghrib, S. Sauvage, X. Checoury, G. Beaudoin, I. Sagnes, G. Picardi, R. Ossikovski, and P. Boucaud. "Direct Band Gap Germanium Microdisks Obtained with Silicon Nitride Stressor Layers". In: ACS Photonics 3.3 (Mar. 2016), pp. 443–448. DOI: 10.1021/acsphotonics. 5b00632.
- [144] M. Grydlik, F. Hackl, H. Groiss, M. Glaser, A. Halilovic, T. Fromherz, W. Jantsch, F. Schäffler, and M. Brehm. "Lasing from Glassy Ge Quantum Dots in Crystalline Si". In: ACS Photonics 3.2 (Feb. 2016), pp. 298–303. DOI: 10.1021/acsphotonics.5b00671.
- [145] S. Bao, D. Kim, C. Onwukaeme, S. Gupta, K. Saraswat, K. H. Lee, Y. Kim, D. Min, Y. Jung, H. Qiu, H. Wang, E. A. Fitzgerald, C. S. Tan, and D. Nam. "Low-threshold optically pumped lasing in highly strained germanium nanowires". In: *Nature Communications* 8.1 (Dec. 2017), p. 1845. DOI: 10.1038/s41467-017-02026-w.
- [146] R. E. Camacho-Aguilera, Y. Cai, N. Patel, J. T. Bessette, M. Romagnoli,
 L. C. Kimerling, and J. Michel. "An electrically pumped germanium laser".
 In: Optics Express 20.10 (May 2012), p. 11316. DOI: 10.1364/0E.20.011316.
- [147] B. Zheng, J. Michel, F. Y. G. Ren, L. C. Kimerling, D. C. Jacobson, and J. M. Poate. "Room-temperature sharp line electroluminescence at $\lambda=1.54$ μm from an erbium-doped, silicon light-emitting diode". In: *Applied Physics Letters* 64.21 (May 1994), pp. 2842–2844. DOI: 10.1063/1.111977.
- [148] J. Palm, F. Gan, B. Zheng, J. Michel, and L. C. Kimerling. "Electroluminescence of erbium-doped silicon". In: *Physical Review B* 54.24 (Dec. 1996), pp. 17603–17615. DOI: 10.1103/PhysRevB.54.17603.
- [149] T. J. Kippenberg, J. Kalkman, A. Polman, and K. J. Vahala. "Demonstration of an erbium-doped microdisk laser on a silicon chip". In: *Physical Review A* 74.5 (Nov. 2006), p. 051802. DOI: 10.1103/PhysRevA.74.051802.

- [150] O. Jambois, F. Gourbilleau, A. J. Kenyon, J. Montserrat, R. Rizk, and B. Garrido. "Towards population inversion of electrically pumped Er ions sensitized by Si nanoclusters". In: *Optics Express* 18.3 (Feb. 2010), p. 2230. DOI: 10.1364/0E.18.002230.
- [151] S. Cueff, C. Labbé, O. Jambois, Y. Berencén, A. J. Kenyon, B. Garrido, and R. Rizk. "Structural factors impacting carrier transport and electroluminescence from Si nanocluster-sensitized Er ions". In: *Optics Express* 20.20 (Sept. 2012), p. 22490. DOI: 10.1364/0E.20.022490.
- [152] W. L. Wilson, P. F. Szajowski, and L. E. Brus. "Quantum Confinement in Size-Selected, Surface-Oxidized Silicon Nanocrystals". In: Science 262.5137 (Nov. 1993), pp. 1242–1244. DOI: 10.1126/science.262.5137.1242.
- [153] L. Pavesi, L. Dal Negro, C. Mazzoleni, G. Franzò, and F. Priolo. "Optical gain in silicon nanocrystals". In: *Nature* 408.6811 (Nov. 2000), pp. 440–444. DOI: 10.1038/35044012.
- [154] R.-J. Zhang, S.-Y. Seo, A. P. Milenin, M. Zacharias, and U. Gösele. "Visible range whispering-gallery mode in microdisk array based on size-controlled Si nanocrystals". In: *Applied Physics Letters* 88.15 (Apr. 2006), p. 153120. DOI: 10.1063/1.2195712.
- [155] D.-C. Wang, C. Zhang, P. Zeng, W.-J. Zhou, L. Ma, H.-T. Wang, Z.-Q. Zhou, F. Hu, S.-Y. Zhang, M. Lu, and X. Wu. "An all-silicon laser based on silicon nanocrystals with high optical gains". In: *Science Bulletin* 63.2 (Jan. 2018), pp. 75–77. DOI: 10.1016/j.scib.2018.01.006.
- [156] H. Rong, A. Liu, R. Jones, O. Cohen, D. Hak, R. Nicolaescu, A. Fang, and M. Paniccia. "An all-silicon Raman laser". In: *Nature* 433.7023 (Jan. 2005), pp. 292–294. DOI: 10.1038/nature03273.
- [157] H. Rong, R. Jones, A. Liu, O. Cohen, D. Hak, A. Fang, and M. Paniccia. "A continous-wave Raman silicon laser". In: *Nature* 433.7027 (Feb. 2005), pp. 717–719. DOI: 10.1038/nature03331.
- [158] Y. Takahashi, Y. Inui, M. Chihara, T. Asano, R. Terawaki, and S. Noda. "A micrometre-scale Raman silicon laser with a microwatt threshold". In: *Nature* 498.7455 (June 2013), pp. 470–474. DOI: 10.1038/nature12237.

- [159] R. Baets. "An ultra-small silicon laser". In: Nature 498 (2013), p. 4475. DOI: 10.1038/msb4100050.
- [160] J. Margetis, S. Al-Kabi, W. Du, W. Dou, Y. Zhou, T. Pham, P. Grant, S. Ghetmiri, A. Mosleh, B. Li, J. Liu, G. Sun, R. Soref, J. Tolle, M. Mortazavi, and S.-Q. Yu. "Si-Based GeSn Lasers with Wavelength Coverage of 2-3 μm and Operating Temperatures up to 180 K". In: ACS Photonics 5.3 (Mar. 2018), pp. 827–833. DOI: 10.1021/acsphotonics.7b00938.
- [161] Q. M. Thai, N. Pauc, J. Aubin, M. Bertrand, J. Chrétien, A. Chelnokov, J. M. Hartmann, V. Reboud, and V. Calvo. "2D hexagonal photonic crystal GeSn laser with 16% Sn content". In: Applied Physics Letters 113.5 (July 2018), p. 051104. DOI: 10.1063/1.5036739.
- [162] D. Stange, N. von den Driesch, S. Wirths, C. Schulte-Braucks, E. Hofmann, J.-M. Hartmann, Z. Ikonic, S. Mantl, D. Grützmacher, and D. Buca. "High Sn Content GeSn LEDs for Group IV Photonics". In: *International SiGe* Technology and Device Meeting (ICSI-VII /ISTDM 2016). Nagoya, 2016.
- [163] D. Stange, N. von den Driesch, T. Zabel, F. Armand-Pilon, B. Marzban, D. Rainko, J.-M. Hartmann, G. Capellini, T. Schroeder, H. Sigg, J. Witzens, D. Grützmacher, and D. Buca. "Reduced Threshold Microdisk Lasers from GeSn/SiGeSn Heterostructures". In: *IEEE Photonics Society- International Conference on Group IV Photonics*. Berlin, 2017.
- [164] A. Einstein. "The Quantum Theory of Radiation". In: *Physikalische Zeitschrift* 18.121 (1917).
- [165] M. G. A. Bernard and G. Duraffourg. "Laser Conditions in Semiconductors". In: physica status solidi (b) 1.7 (1961), pp. 699–703. DOI: 10.1002/pssb.19610010703.
- [166] M. Csele. Fundamentals of Light Sources and Lasers. John Wiley and Sons, Inc, 2004.
- [167] I. D. W. Samuel, E. B. Namdas, and G. A. Turnbull. "How to recognize lasing". In: Nature Photonics 3.10 (Oct. 2009), pp. 546–549. DOI: 10.1038/ nphoton.2009.173.

- [168] B. Dutt, Hai Lin, D. S. Sukhdeo, B. M. Vulovic, S. Gupta, Donguk Nam, K. C. Saraswat, and J. S. Harris. "Theoretical Analysis of GeSn Alloys as a Gain Medium for a Si-Compatible Laser". In: *IEEE Journal of Selected Topics in Quantum Electronics* 19.5 (Sept. 2013), pp. 1502706–1502706. DOI: 10.1109/JSTQE.2013.2241397.
- [169] S.-W. Chang and S. L. Chuang. "Theory of Optical Gain of $\operatorname{Ge-Si}_x\operatorname{Ge}_y\operatorname{Sn}_{1-x-y}$ Quantum-Well Lasers". In: *IEEE Journal of Quantum Electronics* 43.3 (Mar. 2007), pp. 249–256. DOI: 10.1109/JQE.2006.890401.
- [170] Y.-H. Zhu, Q. Xu, W.-J. Fan, and J.-W. Wang. "Theoretical gain of strained $GeSn_{0.02}/Ge_{1-x-y}Si_xSn_y$ quantum well laser". In: *Journal of Applied Physics* 107.7 (Apr. 2010), p. 073108. DOI: 10.1063/1.3329424.
- [171] H. Tran, W. Du, S. A. Ghetmiri, A. Mosleh, G. Sun, R. A. Soref, J. Margetis, J. Tolle, B. Li, H. A. Naseem, and S.-Q. Yu. "Systematic study of $Ge_{1-x}Sn_x$ absorption coefficient and refractive index for the device applications of Sibased optoelectronics". In: *Journal of Applied Physics* 119.10 (Mar. 2016), p. 103106. DOI: 10.1063/1.4943652.
- [172] W. A. Pliskin and R. P. Esch. "Refractive Index of SiO₂ Films Grown on Silicon". In: *Journal of Applied Physics* 36.6 (June 1965), pp. 2011–2013. DOI: 10.1063/1.1714393.
- [173] D. S. Kim, S. G. Yoon, G. E. Jang, S. J. Suh, H. Kim, and D. H. Yoon. "Refractive index properties of SiN thin films and fabrication of SiN optical waveguide". In: *Journal of Electroceramics* 17.2-4 (Dec. 2006), pp. 315–318. DOI: 10.1007/s10832-006-9710-x.
- [174] S. L. McCall, A. F. J. Levi, R. E. Slusher, S. J. Pearton, and R. A. Logan. "Whispering-gallery mode microdisk lasers". In: *Applied Physics Letters* 60.3 (Jan. 1992), pp. 289–291. DOI: 10.1063/1.106688.
- [175] L. Y. M. Tobing and P. Dumon. Photonic Microresonator Research and Applications. Ed. by I. Chremmos, O. Schwelb, and N. Uzunoglu. Vol. 156. Springer Series in Optical Sciences. Boston, MA: Springer US, 2010, pp. 1–27. DOI: 10.1007/978-1-4419-1744-7.

- [176] A. Matsko and V. Ilchenko. "Optical resonators with whispering-gallery modespart I: basics". In: *IEEE Journal of Selected Topics in Quantum Electronics* 12.1 (Jan. 2006), pp. 3–14. DOI: 10.1109/JSTQE.2005.862952.
- [177] K. J. Vahala. "Optical microcavities". In: Nature 424.6950 (Aug. 2003), pp. 839–846. DOI: 10.1038/nature01939.
- [178] J. E. Heebner, T. C. Bond, and J. S. Kallman. "Generalized formulation for performance degradations due to bending and edge scattering loss in microdisk resonators". In: *Optics Express* 15.8 (2007), p. 4452. DOI: 10. 1364/0E.15.004452.
- [179] S. Gupta, R. Chen, Y.-c. Huang, Y. Kim, E. Sanchez, J. S. Harris, and K. C. Saraswat. "Highly Selective Dry Etching of Germanium over Germanium-Tin ($Ge_{1-x}Sn_x$): A Novel Route for $Ge_{1-x}Sn_x$ Nanostructure Fabrication". In: Nano Letters 13.8 (Aug. 2013), pp. 3783–3790. DOI: 10.1021/n14017286.
- [180] R. Chen, S. Gupta, Y.-C. Huang, Y. Huo, C. W. Rudy, E. Sanchez, Y. Kim, T. I. Kamins, K. C. Saraswat, and J. S. Harris. "Demonstration of a Ge/GeSn/Ge Quantum-Well Microdisk Resonator on Silicon: Enabling High-Quality Ge(Sn) Materials for Micro- and Nanophotonics". In: *Nano Letters* 14.1 (Jan. 2014), pp. 37–43. DOI: 10.1021/n1402815v.
- [181] L. Milord, J. Aubin, A. Gassenq, S. Tardif, K. Guilloy, N. Pauc, J. Rothman, A. Chelnokov, J. M. Hartmann, V. Calvo, and V. Reboud. "Inductively coupled plasma etching of germanium tin for the fabrication of photonic components". In: *Silicon Photonics XII*. Ed. by G. T. Reed and A. P. Knights. Feb. 2017, p. 101080C. DOI: 10.1117/12.2252280.
- [182] D. Stange, S. Wirths, R. Geiger, C. Schulte-Braucks, B. Marzban, N. V. D. Driesch, G. Mussler, T. Zabel, T. Stoica, J. M. Hartmann, S. Mantl, Z. Ikonic, D. Grützmacher, H. Sigg, J. Witzens, and D. Buca. "SI: Optically Pumped GeSn Microdisk Lasers on Si". In: ACS Photonics 3.7 (2016), pp. 1279–1285. DOI: 10.1021/acsphotonics.6b00258.
- [183] A. S. Vasin, F. Oliveira, M. F. Cerqueira, J. Schulze, and M. I. Vasilevskiy. "Structural and vibrational properties of $\operatorname{Sn}_x \operatorname{Ge}_{1-x}$: Modeling and experi-

- ments". In: Journal of Applied Physics 124.3 (July 2018), p. 035105. DOI: 10.1063/1.5030104.
- [184] Z. Sui and I. P. Herman. "Effect of strain on phonons in Si, Ge, and Si/Ge heterostructures". In: *Physical Review B* 48.24 (Dec. 1993), pp. 17938–17953. DOI: 10.1103/PhysRevB.48.17938.
- [185] V. D'Costa, J. Tolle, R. Roucka, C. Poweleit, J. Kouvetakis, and J. Menéndez. "Raman scattering in Ge_{1-y}Sn_y alloys". In: *Solid State Communications* 144.5-6 (Nov. 2007), pp. 240–244. DOI: 10.1016/j.ssc.2007.08.020.
- [186] H. Lin, R. Chen, Y. Huo, T. I. Kamins, and J. S. Harris. "Raman study of strained $Ge_{1-x}Sn_x$ alloys". In: *Applied Physics Letters* 98.26 (2011), p. 261917. DOI: 10.1063/1.3606384.
- [187] J.-H. Fournier-Lupien, S. Mukherjee, S. Wirths, E. Pippel, N. Hayazawa, G. Mussler, J. M. Hartmann, P. Desjardins, D. Buca, and O. Moutanabbir. "Strain and composition effects on Raman vibrational modes of silicongermanium-tin ternary alloys". In: Applied Physics Letters 103.26 (Dec. 2013), p. 263103. DOI: 10.1063/1.4855436.
- [188] R. Cheng, W. Wang, X. Gong, L. Sun, P. Guo, H. Hu, Z. Shen, G. Han, and Y.-C. Yeo. "Relaxed and Strained Patterned Germanium-Tin Structures: A Raman Scattering Study". In: ECS Journal of Solid State Science and Technology 2.4 (Jan. 2013), P138–P145. DOI: 10.1149/2.013304jss.
- [189] A. Gassenq, L. Milord, J. Aubin, N. Pauc, K. Guilloy, J. Rothman, D. Rouchon, A. Chelnokov, J. M. Hartmann, V. Reboud, and V. Calvo. "Raman spectral shift versus strain and composition in GeSn layers with 6%-15% Sn content". In: *Applied Physics Letters* 110.11 (Mar. 2017), p. 112101. DOI: 10.1063/1.4978512.
- [190] M. J. Süess, R. a. Minamisawa, R. Geiger, K. K. Bourdelle, H. Sigg, and R. Spolenak. "Power-dependent Raman analysis of highly strained Si nanobridges." In: Nano letters 14.3 (Mar. 2014), pp. 1249–54. DOI: 10.1021/n1404152r.
- [191] Z. Sui, H. H. Burke, and I. P. Herman. "Raman scattering in germanium-silicon alloys under hydrostatic pressure". In: *Physical Review B* 48.4 (July 1993), pp. 2162–2168. DOI: 10.1103/PhysRevB.48.2162.

- [192] M. J. Süess, R. Geiger, R. A. Minamisawa, G. Schiefler, J. Frigerio, D. Chrastina, G. Isella, R. Spolenak, J. Faist, and H. Sigg. "Analysis of enhanced light emission from highly strained germanium microbridges". In: *Nature Photonics* 7.6 (Apr. 2013), pp. 466–472. DOI: 10.1038/nphoton.2013.67.
- [193] A. Gassenq, S. Tardif, K. Guilloy, I. Duchemin, N. Pauc, J. M. Hartmann, D. Rouchon, J. Widiez, Y. M. Niquet, L. Milord, T. Zabel, H. Sigg, J. Faist, A. Chelnokov, F. Rieutord, V. Reboud, and V. Calvo. "Raman-strain relations in highly strained Ge: Uniaxial \langle 100 \rangle, \langle 110 \rangle and biaxial (001) stress". In: Journal of Applied Physics 121.5 (Feb. 2017), p. 055702. DOI: 10.1063/1.4974202.
- [194] J. Van Campenhout, P. Rojo-Romeo, D. Van Thourhout, C. Seassal, P. Regreny, L. Di Cioccio, J. M. Fedeli, and R. Baets. "Thermal characterization of electrically injected thin-film InGaAsP microdisk lasers on Si". In: *Journal of Lightwave Technology* 25.6 (2007), pp. 1543–1548. DOI: 10.1109/JLT.2007.895552.
- [195] P. Mena, J. Morikuni, S.-M. Kang, A. Harton, and K. Wyatt. "A simple rate-equation-based thermal VCSEL model". In: *Journal of Lightwave Technology* 17.5 (May 1999), pp. 865–872. DOI: 10.1109/50.762905.
- [196] D. Sukhdeo, Y. Kim, S. Gupta, K. Saraswat, B. Dutt, and D. Nam. "Theoretical Modeling for the Interaction of Tin Alloying With N-Type Doping and Tensile Strain for GeSn Lasers". In: *IEEE Electron Device Letters* 37.10 (Oct. 2016), pp. 1307–1310. DOI: 10.1109/LED.2016.2603162. arXiv: 1506.08402.
- [197] C. Y. Tsai, C. Y. Tsai, C. H. Chen, T. L. Sung, T. Y. Wu, and F. P. Shih. "Theoretical model for intravalley and intervalley free-carrier absorption in semiconductor lasers: Beyond the classical drude model". In: *IEEE Journal of Quantum Electronics* 34.3 (1998), pp. 552–558. DOI: 10.1109/3.661466.
- [198] R. Camacho-Aguilera, Z. Han, Y. Cai, L. C. Kimerling, and J. Michel. "Direct band gap narrowing in highly doped Ge". In: Applied Physics Letters 102.15 (Apr. 2013), p. 152106. DOI: 10.1063/1.4802199.

- [199] S. Al-Kabi, S. A. Ghetmiri, J. Margetis, W. Du, A. Mosleh, M. Alher, W. Dou, J. M. Grant, G. Sun, R. A. Soref, J. Tolle, B. Li, M. Mortazavi, H. A. Naseem, and S.-Q. Yu. "Optical Characterization of Si-Based Ge_{1-x}Sn_x Alloys with Sn Compositions up to 12%". In: *Journal of Electronic Materials* 45.4 (Apr. 2016), pp. 2133–2141. DOI: 10.1007/s11664-015-4283-6.
- [200] H. Rupprecht, J. M. Woodall, and G. D. Pettit. "Efficient Visible Electro-luminescence at 300 K from Ga_{1-x}Al_xAs p-n Junctions Grown by Liquid-Phase Epitaxy". In: *Applied Physics Letters* 11.3 (Aug. 1967), pp. 81–83. DOI: 10.1063/1.1755045.
- [201] I. Hayashi, M. B. Panish, and F. K. Reinhart. "GaAs-Al $_x$ Ga $_{1-x}$ As Double Heterostructure Injection Lasers". In: *Journal of Applied Physics* 42.5 (Apr. 1971), pp. 1929–1941. DOI: 10.1063/1.1660469.
- [202] R. Dingle, W. Wiegmann, and C. H. Henry. "Quantum States of Confined Carriers in Very Thin Al_xGa_{1-x}As-GaAs-Al_xGa_{1-x}As Heterostructures". In: Physical Review Letters 33.14 (Sept. 1974), pp. 827–830. DOI: 10.1103/ PhysRevLett.33.827.
- [203] W. T. Tsang. "Extremely low threshold (AlGa)As graded-index waveguide separate-confinement heterostructure lasers grown by molecular beam epitaxy". In: *Applied Physics Letters* 40.3 (Feb. 1982), pp. 217–219. DOI: 10.1063/1.93046.
- [204] G. Park, O. B. Shchekin, D. L. Huffaker, and D. G. Deppe. "Low-threshold oxide-confined 1.3 μ m quantum-dot laser". In: *IEEE Photonics Technology Letters* 12.3 (2000), pp. 230–232. DOI: 10.1109/68.826897.
- [205] M. Bauer, C. Ritter, P. A. Crozier, J. Ren, J. Menendez, G. Wolf, and J. Kouvetakis. "Synthesis of ternary SiGeSn semiconductors on Si(100) via $\operatorname{Sn}_x\operatorname{Ge}_{1-x}$ buffer layers". In: *Applied Physics Letters* 83.11 (2003), pp. 2163–2165. DOI: 10.1063/1.1606104.
- [206] W. Dou, Y. Zhou, J. Margetis, S. A. Ghetmiri, S. Al-Kabi, W. Du, J. Liu, G. Sun, R. A. Soref, J. Tolle, B. Li, M. Mortazavi, and S.-Q. Yu. "Optically pumped lasing at 3 μ m from compositionally graded GeSn with tin up to

- 22.3%". In: *Optics Letters* 43.19 (Oct. 2018), p. 4558. DOI: 10.1364/OL.43. 004558.
- [207] D. Rainko, Z. Ikonic, N. Vukmirović, D. Stange, N. von den Driesch, D. Grützmacher, and D. Buca. "Investigation of carrier confinement in direct bandgap GeSn/SiGeSn 2D and 0D heterostructures". In: Scientific Reports 8.1 (2018), p. 15557. DOI: 10.1038/s41598-018-33820-1.
- [208] A. Portavoce, I. Berbezier, P. Gas, and A. Ronda. "Sb surface segregation during epitaxial growth of SiGe heterostructures: The effects of Ge composition and biaxial stress". In: *Physical Review B* 69.15 (Apr. 2004), p. 155414. DOI: 10.1103/PhysRevB.69.155414.
- [209] E. Hofmann. "Characterization of GeSn Tunnel Diodes and Contacts for Novel Devices". In: *Master thesis*. RWTH Aachen University. 2016.
- [210] M. Panish, H. Casey, S. Sumski, and P. Foy. "Reduction of threshold current density in GaAs-Al_xGa_{1-x}As heterostructure lasers by separate optical and carrier confinement". In: Applied Physics Letters 22.11 (June 1973), pp. 590– 591. DOI: 10.1063/1.1654518.
- [211] G. Thompson and P. Kirkby. "(GaAl)As lasers with a heterostructure for optical confinement and additional heterojunctions for extreme carrier confinement". In: *IEEE Journal of Quantum Electronics* 9.2 (Feb. 1973), pp. 311– 318. DOI: 10.1109/JQE.1973.1077458.
- [212] W. T. Tsang. "A graded-index waveguide separate-confinement laser with very low threshold and a narrow Gaussian beam". In: Applied Physics Letters 39.2 (July 1981), pp. 134–137. DOI: 10.1063/1.92658.
- [213] C. S. Fenrich, X. Chen, R. Chen, Y. C. Huang, H. Chung, M. Y. Kao, Y. Huo, T. I. Kamins, and J. S. Harris. "Strained Pseudomorphic $Ge_{1-x}Sn_x$ Multiple Quantum Well Microdisk Using SiN_y Stressor Layer". In: *ACS Photonics* 3.12 (2016), pp. 2231–2236. DOI: 10.1021/acsphotonics.6b00562.
- [214] A. Jamshidi, M. Noroozi, M. Moeen, A. Hallén, B. Hamawandi, J. Lu, L. Hultman, M. Östling, and H. Radamson. "Growth of GeSnSiC layers for photonic applications". In: Surface and Coatings Technology 230 (Sept. 2013), pp. 106–110. DOI: 10.1016/j.surfcoat.2013.06.074.

- [215] R. Soref. "Direct-bandgap compositions of the CSiGeSn group-IV alloy". In: Optical Materials Express 4.4 (Apr. 2014), p. 836. DOI: 10.1364/OME.4.000836.
- [216] Z. Ikonić. "Electronic structure of (Si)GeSn and its tuning via incorporation of carbon". In: *IEEE Photonics Society Summer Topicals*. Vol. 3. 2016, pp. 55–56.

Acknowledgements

During my time as a PhD student, I got a lot of support by many people, whom I would like to show my gratitude at this point. I spent an exciting time in Jülich, learned a lot about research and evolved not only as a scientist.

At the beginning, I thank my doctoral supervisor *Prof. Detlev Grützmacher*, who enabled me to undertake my PhD thesis in his institute. Through his interest in the topic, he promoted me not only in doing my research but also in presenting it to the scientific community. I am further indebted to *Prof. Siegfried Mantl*, who admitted me as a member in his part of the institute. *Prof. Thomas Taubner* agreed to undertake the second review of my thesis, which I gratefully appreciate.

A strong motivator during my PhD thesis was *Dr. Dan Buca*, the leader of the GeSn group. His enthusiasm pushed me forward and his high expectations challenged me from time to time. He supported my every day life by his addressability and enabled all conference trips as well as visits at other institutes, for which I am deeply thankful.

I also thank the whole GeSn team. It was great joy working with you and I think, it is true to say that we became good friends over time, while ongoing debates on physics and several after work activities did the rest. Dr. Nils von den Driesch grew most of the material I worked with, conducted RBS and ECV measurements, for which I am beholden to him. Additionally, I am very grateful for the discussions we had, work-related and non-work-related, which in each case sometimes got out of hand and were lost in detail. In this context, we shared liters of coffee, which, totally in the spirit of science, were explored by using many different methods. Anyway, I benefited from his deep knowledge of physics, his differentiated view on various topics and his wisdom adapted from XKCD, The Simpsons and The Naked Gun.

I thank *Denis Rainko* for band structure calculations as well as the material growth which he performed. In him I found a fascinating colleague, with whom I exchanged many ideas of physics but also various aspects on the philosophy of life. We spent an exciting time in Japan and he absolutely enriched my time in Jülich.

As former member of the GeSn group, I thank *Dr. Christian Schulte-Braucks* for extensive pioneering work regarding GeSn processing techniques and his support by fabricating the first generation of LEDs.

Continuous feeding of espresso lied in *Konstantin Mertens'* hands and was a culinary enrichment.

All in all, I am very glad, that we had a strong group cohesion with the whole PhD students. *Ulrich Tromm* engaged in organizing events and cake weeks, which became fabulous through *Stefan Glass'* cheese cake and the party animal *Dr. Vinh Luong*. In addition I am much obliged to *Dr. Toma Stoica*, who introduced many measurement procedures to me and supported a lot of physical interpretation of the data. Thanks goes to the whole Waldschlösschen team, namely *Andreas Tiedemann*, *Karl-Heinz Deussen* and *Patric Bernardy*. They supported ALD layer growth in this work and provided assistance when there was trouble in the optical laboratory. For solving cooling issues and also construction of sample holders I thank *Herbert Kertz* for his help. Furthermore, many people afforded me their assistance with a lot of material characterization methods. In this regard, I express my gratitude to *Dr. Gregor Mussler* for various XRD, *Dr. Uwe Breuer* for SIMS, *Steffi Lenk* and *Lidia Kibkalo* for TEM and *Dr. Ivan Povstugar* for APT measurements. Thanks also to the *HNF* staff, who ensured the cleanroom to be in working order.

Besides internal colleagues, there were many collaborators, who strongly supported my work. First of all, I owe a deep gratitude to *Dr. Hans Sigg*. He provided his optical set-up and some weeks each year for the PL spectroscopy of microdisk lasers. Additionally, he intensively contributed to data analysis and writing of publications. In that respect, I thank *Dr. Richard Geiger* and *Dr. Stephan Wirths*, from whom I learned operating the set-up. We performed the measurements on single-layer MDs together. The following experiments of doped GeSn lasers were accompanied by *Esteban Marín*. The third and most intensive measurement series on heterostructure lasers was supported by *Francesco Armand Pilon* and *Dr. Thomas Zabel*, who also helped with *Raman* measurements of suspended structures at *ETH Zürich*. All

in all, I spend a lot of exciting and fascinating hours at *PSI* and therefore I want to thank all the people who contributed. I owe a debt of gratitude to *Dr. Zoran Ikonić* for providing the code for band structure calculations and for giving vast numbers of advice regarding many questions about physics. I am thankful and glad that we worked in a collaboration with *Prof. Jeremy Witzens* and *Bahareh Marzban*. They contributed strain simulations, mode analysis and the design for electrical pumped lasers. Also, they greatly supported the paper writing.

I also thank *Dr. Jean-Michel Hartmann* for the Ge-VS, which formed the base of all GeSn layer growth. Representative for all people from *IHP* who participated in the heterostructure layer characterization via XRD, EDX and TEM analysis, I acknowledge *Prof. Giovanni Capellini*.

Additional thanks goes to all members of the institute, which have not been named previously, for a cooperative and pleasant working atmosphere.

Finally, I am greatly appreciative for the support, which I experienced from my family and friends during my whole academic career. My wonderful partner *Christian Ingenhorst* carefully listened to all of my concerns, including technically ones, and charged my battery whenever it was empty. I am deeply grateful for him and his solidarity.

List of Publications

Primary Author

- D. Stange, S. Wirths, N. von den Driesch, G. Mussler, T. Stoica, Z. Ikonic, J. M. Hartmann, S. Mantl, D. Grützmacher, and D. Buca. "Optical Transitions in Direct-Bandgap Ge_{1-x}Sn_x Alloys". In: ACS Photonics 2.11 (Nov. 2015), pp. 1539–1545. DOI: 10.1021/acsphotonics.5b00372.
- D. Stange, N. von den Driesch, D. Rainko, C. Schulte-Braucks, S. Wirths, G. Mussler, A. T. Tiedemann, T. Stoica, J. M. Hartmann, Z. Ikonic, S. Mantl, D. Grützmacher, and D. Buca. "Study of GeSn based heterostructures: towards optimized group IV MQW LEDs". In: Optics Express 24.2 (Jan. 2016), p. 1358.
 DOI: 10.1364/0E.24.001358.
- D. Stange, S. Wirths, R. Geiger, C. Schulte-Braucks, B. Marzban, N. von den Driesch, G. Mussler, T. Zabel, T. Stoica, J.-M. Hartmann, S. Mantl, Z. Ikonic, D. Grützmacher, H. Sigg, J. Witzens, and D. Buca. "Optically Pumped GeSn Microdisk Lasers on Si". In: ACS Photonics 3.7 (July 2016), pp. 1279–1285.
 DOI: 10.1021/acsphotonics.6b00258.
- D. Stange, C. Schulte-Braucks, N. von den Driesch, S. Wirths, G. Mussler, S. Lenk, T. Stoica, S. Mantl, D. Grützmacher, D. Buca, R. Geiger, T. Zabel, H. Sigg, J.-M. Hartmann, and Z. Ikonic. "High Sn-Content GeSn Light Emitters for Silicon Photonics". In: Future Trends in Microelectronics- Journey into the

unknown. Ed. by S. Luryi, J. Xu, and A. Zaslavsky. Wiley, 2016. Chap. 2.6, pp. 181–191.

- D. Stange, N. von den Driesch, D. Rainko, S. Roesgaard, I. Povstugar, J.-M. Hartmann, T. Stoica, Z. Ikonic, S. Mantl, D. Grützmacher, and D. Buca. "Short-wave infrared LEDs from GeSn/SiGeSn multiple quantum wells". In: *Optica* 4.2 (Feb. 2017), p. 185. DOI: 10.1364/0PTICA.4.000185.
- D. Stange, N. von den Driesch, T. Zabel, F. Armand-Pilon, D. Rainko, B. Marzban, P. Zaumseil, J.-M. Hartmann, Z. Ikonic, G. Capellini, S. Mantl, H. Sigg, J. Witzens, D. Grützmacher, and D. Buca. "GeSn/SiGeSn Heterostructure and Multi Quantum Well Lasers". In: *ACS Photonics* 5.11 (Nov. 2018), pp. 4628–4636. DOI: 10.1021/acsphotonics.8b01116.

Contributing Author

- S. Wirths, D. Stange, M.-A. Pampillón, A. T. Tiedemann, G. Mussler, A. Fox, U. Breuer, B. Baert, E. San Andrés, N. D. Nguyen, J.-M. Hartmann, Z. Ikonic, S. Mantl, and D. Buca. "High- k Gate Stacks on Low Bandgap Tensile Strained Ge and GeSn Alloys for Field-Effect Transistors". In: ACS Applied Materials and Interfaces 7.1 (Jan. 2015), pp. 62–67. DOI: 10.1021/am5075248.
- N. von den Driesch, D. Stange, S. Wirths, G. Mussler, B. Holländer, Z. Ikonic, J. M. Hartmann, T. Stoica, S. Mantl, D. Grützmacher, and D. Buca. "Direct Bandgap Group IV Epitaxy on Si for Laser Applications". In: *Chemistry of Materials* 27.13 (June 2015), pp. 4693–4702. DOI: 10.1021/acs.chemmater. 5b01327.
- C. Schulte-Braucks, D. Stange, N. von den Driesch, S. Blaeser, Z. Ikonic, J. M. Hartmann, S. Mantl, and D. Buca. "Negative differential resistance in direct band-gap GeSn p-i-n structures". In: *Applied Physics Letters* 107.4 (July 2015), p. 042101. DOI: 10.1063/1.4927622.

- S. Hooda, S. A. Khan, B. Satpati, D. Stange, D. Buca, M. Bala, C. Pannu, D. Kanjilal, and D. Kabiraj. "Effect of ion beam parameters on engineering of nanoscale voids and their stability under post-growth annealing". In: *Applied Physics A* 122.3 (Mar. 2016), p. 227. DOI: 10.1007/s00339-016-9776-5.
- N. von den Driesch, D. Stange, S. Wirths, D. Rainko, G. Mussler, T. Stoica, Z. Ikonić, J.-M. Hartmann, D. Grützmacher, S. Mantl, and D. Buca. "Direct bandgap GeSn light-emitting diodes for short-wave infrared applications grown on Si". In: SPIE Photonics West. Ed. by G. T. Reed and A. P. Knights. Vol. 9752. Mar. 2016, p. 97520C. DOI: 10.1117/12.2211641.
- N. von den Driesch, D. Stange, S. Wirths, D. Rainko, I. Povstugar, A. Savenko, U. Breuer, R. Geiger, H. Sigg, Z. Ikonic, J.-M. Hartmann, D. Grützmacher, S. Mantl, and D. Buca. "SiGeSn Ternaries for Efficient Group IV Heterostructure Light Emitters". In: Small 13.16 (Apr. 2017), p. 1603321. DOI: 10.1002/smll. 201603321.
- N. von den Driesch, D. Stange, D. Rainko, I. Povstugar, P. Zaumseil, G. Capellini, T. Schröder, T. Denneulin, Z. Ikonic, J.-M. Hartmann, H. Sigg, S. Mantl, D. Grützmacher, and D. Buca. "Advanced GeSn/SiGeSn Group IV Heterostructure Lasers". In: Advanced Science 5.6 (June 2018), p. 1700955.
 DOI: 10.1002/advs.201700955.
- C. Schulte-Braucks, S. Glass, E. Hofmann, D. Stange, N. von den Driesch, J. Hartmann, Z. Ikonic, Q. Zhao, D. Buca, and S. Mantl. "Process modules for GeSn nanoelectronics with high Sn-contents". In: *Solid-State Electronics* 128 (Feb. 2017), pp. 54–59. DOI: 10.1016/j.sse.2016.10.024.
- P. Zaumseil, Y. Hou, M. A. Schubert, N. von den Driesch, D. Stange, D. Rainko, M. Virgilio, D. Buca, and G. Capellini. "The thermal stability of epitaxial GeSn layers". In: *APL Materials* 6.7 (July 2018), p. 076108. DOI: 10.1063/1.5036728.

- R. Loo, Y. Shimura, S. Ike, A. Vohra, T. Stoica, D. Stange, D. Buca, D. Kohen, J. Margetis, and J. Tolle. "Epitaxial GeSn: impact of process conditions on material quality". In: Semiconductor Science and Technology (Sept. 2018). DOI: 10.1088/1361-6641/aae2f9.
- D. Rainko, Z. Ikonic, N. Vukmirović, D. Stange, N. von den Driesch, D. Grützmacher, and D. Buca. "Investigation of carrier confinement in direct bandgap GeSn/SiGeSn 2D and 0D heterostructures". In: Scientific Reports 8.1 (2018), p. 15557. DOI: 10.1038/s41598-018-33820-1.
- D. Rainko, Z. Ikonic, A. Elbaz, N. von den Driesch, D. Stange, E. Herth, P. Boucaud, M. El Kurdi, D. Grützmacher, and D. Buca. "Impact of tensile strain on low Sn content GeSn lasing". In: *Scientific Reports* 9.1 (Jan. 2019), p. 259. DOI: 10.1038/s41598-018-36837-8.
- N. von den Driesch, D. Stange, D. Rainko, U. Breuer, G. Capellini, J.-M. Hartmann, H. Sigg, S. Mantl, D. Grützmacher, and D. Buca. "Epitaxy of Si-Ge-Sn-based heterostructures for CMOS-integratable light emitters". In: Solid-State Electronics (Mar. 2019). DOI: 10.1016/j.sse.2019.03.013.

Conference Contributions

- D. Stange, C. Schulte-Braucks, N. von den Driesch, S. Wirths, G. Mussler, P. Bernardy, A. Tiedemann, T. Stoica, J.-M. Hartmann, Z. Ikonic, S. Mantl, D. Grützmacher, and D. Buca. "High Sn-content GeSn for infrared light emitting diodes". In: *European Materials Research Society (E-MRS 2015)*. Lille, France, 2015, Symposium K.
- D. Stange, N. von den Driesch, S. Wirths, C. Schulte-Braucks, E. Hofmann, J.-M. Hartmann, Z. Ikonic, S. Mantl, D. Grützmacher, and D. Buca. "High Sn Content GeSn LEDs for Group IV Photonics". In: *International SiGe Tech*nology and Device Meeting (ICSI-VII /ISTDM 2016). Nagoya, 2016.

- D. Stange, N. von den Driesch, S. Wirths, R. Geiger, B. Marzban, C. Schulte-Braucks, Z. Ikonic, J.-M. Hartmann, S. Mantl, J. Witzens, H. Sigg, D. Grützmacher, and D. Buca. "Optically Pumped GeSn Microdisk Laser". In: Workshop on "Controlled Processing for Ultra-large Scale Integration" (JSPS). Jülich, 2016.
- D. Stange, N. von den Driesch, D. Rainko, Z. Ikonic, J.-M. Hartmann, S. Mantl, D. Buca, and D. Grützmacher. "GeSn/SiGeSn Heterostructures for Si Optoelectronics". In: Compound Semiconductor Week 2017. Berlin, 2017.
- D. Stange, N. von den Driesch, T. Zabel, F. Armand-Pilon, B. Marzban, D. Rainko, J.-M. Hartmann, G. Capellini, T. Schroeder, H. Sigg, J. Witzens, D. Grützmacher, and D. Buca. "Reduced Threshold Microdisk Lasers from GeSn/SiGeSn Heterostructures". In: *IEEE Photonics Society- International Conference on Group IV Photonics*. Berlin, 2017.
- D. Stange, N. von den Driesch, D. Rainko, T. Zabel, B. Marzban, Z. Ikonic, P. Zaumseil, G. Capellini, S. Manti, J. Witzens, H. Sigg, D. Grützmacher, and D. Buca. "Quantum confinement effects in GeSn/SiGeSn heterostructure lasers".
 In: 2017 IEEE International Electron Devices Meeting (IEDM). IEEE, Dec. 2017, pp. 24.2.1–24.2.4. DOI: 10.1109/IEDM.2017.8268451.
- D. Stange, N. von den Driesch, T. Zabel, F. Armand-Pilon, D. Rainko, A. T. Tiedemann, J.-M. Hartmann, G. Capellini, Z. Ikonić, H. Sigg, D. Grützmacher, and D. Buca. "GeSn lasers". In: *IEEE International Semiconductor Conference (CAS)*. Sinaia, Romania, 2018, International Workshop on GeSn photonics.

Curriculum Vitae

Name Date and Place of Birth Daniela Stange 13.02.1990 / Viersen

WORK EXPERIENCE

DEC/2014 – JUN/2018 Graduate Student Researcher

■ Forschungszentrum Jülich GmbH, Peter Grünberg Institut 9

Group IV Semiconductor physics, Optics und Electronics

OCT/2012 – SEP/2014 Student Assistant in the Field of Teaching

3. Physikalisches Institut B, RWTH Aachen

Supervisor of exercise courses on experimental physics 1

Responsible for experiments during lecture

EDUCATION

DEC/2014 – FEB/2019 **Doctorate in Physics**

Forschungszentrum Jülich GmbH, Peter Grünberg Institut 9 Thesis: Group IV (Si)GeSn Light Emission and Lasing Studies

OCT/2012 – SEP/2014 Master of Science, Physics

RWTH Aachen University

Specialization: Condensed Matter Physics

Thesis: Electrical and Optical Characterization of Indirect and

Fundamental Direct Bandgap GeSn Alloys

OCT/2009 – SEP/2012 Bachelor of Science, Physics

RWTH Aachen University

<u>Thesis</u>: Development and Commissioning of a Cooling Test Stand for Measurements on Silicon-Photomultipliers

AUG/2000 - MAY/2009

General Qualification for University Entrance (Abitur)

Gymnasium an der Gartenstraße, Mönchengladbach

Specialization: Mathematics, Physics

SPECIAL QUALIFICATIONS

LANGUAGES • German (Mother Tongue), English (Fluent)

■ Origin, Adobe Illustrator, MS Office, Latex

Schriften des Forschungszentrums Jülich Reihe Schlüsseltechnologien / Key Technologies

Band / Volume 180

Manipulation of magnetism in iron oxide nanoparticle / BaTiO₃ composites and low-dimensional iron oxide nanoparticle arrays

L. Wang (2018), VI, 151 pp ISBN: 978-3-95806-351-8

Band / Volume 181

Creating and characterizing a single molecule device for quantitative surface science

M. Green (2018), viii, 142 pp (untersch. Pag.) ISBN: 978-3-95806-352-5

Band / Volume 182

8th Georgian-German School and Workshop in Basic Science

A. Kacharava (Ed.) erscheint nur als CD (2018)

ISBN: 978-3-95806-353-2

Band / Volume 183

Topological properties of complex magnets from an advanced *ab-initio* Wannier description

J.-P. Hanke (2018), xi, 173 pp ISBN: 978-3-95806-357-0

Band / Volume 184

Translation Initiation with 70S Ribosomes: A Single Molecule Study

C. Remes (2018), iv, 113 pp ISBN: 978-3-95806-358-7

Band / Volume 185

Scanning tunneling potentiometry at nanoscale defects in thin films

F. Lüpke (2018), iv, 144 pp (untersch. Pag.)

ISBN: 978-3-95806-361-7

Band / Volume 186

Inelastic neutron scattering on magnetocaloric compounds

N. Biniskos (2018), iii, 92 pp ISBN: 978-3-95806-362-4

Band / Volume 187

Magnetic Order and Excitation in Frustrated Pyrochlore 5d - Transition Metal Oxides

E. Feng (2018), iv, 182 pp ISBN: 978-3-95806-365-5 Band / Volume 188

Finite-Difference Time-Domain Simulations Assisting to Reconstruct the Brain's Nerve Fiber Architecture by 3D Polarized Light Imaging

M. Menzel (2018), ix, 296 pp ISBN: 978-3-95806-368-6

Band / Volume 189

Characterization of the cell-substrate interface using surface plasmon resonance microscopy

E. M. Kreysing (2018), xiii, 260 pp ISBN: 978-3-95806-369-3

Band / Volume 190

Scattering! Soft, Functional and Quantum Materials

Lecture Notes of the 50th IFF Spring School 2019 11 – 22 March 2019, Jülich, Germany ed. by M. Angst, T. Brückel, S. Förster, K. Friese, R. Zorn (2019), ca 1000 pp ISBN: 978-3-95806-380-8

Band / Volume 191

Absolute scale off-axis electron holography of thin dichalcogenide crystals at atomic resolution

F. Winkler (2019), xxiii, 187 pp ISBN: 978-3-95806-383-9

Band / Volume 192

High-resolution genome and transcriptome analysis of *Gluconobacter* oxydans 621H and growth-improved strains by next-generation sequencing

A. Kranz (2019), III, 182 pp ISBN: 978-3-95806-385-3

Band / Volume 193

Group IV (Si)GeSn Light Emission and Lasing Studies

D. Stange (2019), vi, 151 pp ISBN: 978-3-95806-389-1

Weitere Schriften des Verlags im Forschungszentrum Jülich unter

http://wwwzb1.fz-juelich.de/verlagextern1/index.asp

Schlüsseltechnologien / Key Technologies Band / Volume 193 ISBN 978-3-95806-389-1

